Multifunctional Carbon-Polymer Composites for Temperature Sensing and De-icing

A Dissertation

Presented to
the Faculty of the Department of Mechanical Engineering
University of Houston

In Partial Fulfillment
of the Requirements for the Degree
Doctorate of Philosophy
in Mechanical Engineering

by
Christiana Chang

August 2013

Multifunctional Carbon-Polymer Composites for Temperature Sensing and De-icing

---

Christiana Chang

Approved:

Chairman of the Committee
Gangbing Song, Professor
Mechanical Engineering

Matthew Franchek, Professor
Mechanical Engineering

Li Mo, Associate Professor
Civil and Environmental Engineering

Yi-Lung Mo, Professor
Civil and Environmental Engineering

Pradeep Sharma, Professor
Mechanical Engineering

Suresh Khator, Associate Dean,
Cullen College of Engineering

Pradeep Sharma, Chairman
Mechanical Engineering

Acknowledgements

This project was funded in part by the National Science Foundation and through the Department of Education's GAANN program grant for graduate research and professional development. The author was supported by both the GAANN grant and the NSF's GK-12 fellowship. This project was conducted in the Smart Materials and Structures Laboratory under the guidance of Dr. Gangbing Song. I am grateful for his guidance on this work, as well as the opportunities he's given me to broaden my view of the polymer composites field. I would also like thank Dr. S.S. Wang and Dr. P. Sharma for their support through the GAANN and GK-12 programs, respectively. This work would not have been completed without the assistance of a number of other members of Dr. Song's lab, especially Ms. Subhadra Burughla, Mr. Mithun Singla, Mr. Timothy Lai, and Mr. Larry Vuong. Additional work was conducted at Chiba University, Chiba, Japan, under the generous guidance of Dr. Ning Hu and with the assistance of his doctoral students Mr. Alamusi, Mr. Liangke Wu, and Ms. Yaolu Liu. The work conducted at Chiba University was supported by the US NSF and the Japan Society for the Promotion of Science (JSPS). Facilities and support for the UAA de-icing field test were provided by Dr. Joey Yang of the Dept. of Civil Engineering, University of Alaska at Anchorage with site assistance from Mr. Simon and Corbin Rowe. Use of tensile testing equipment was generously given by Dr. Mo Li of the Materials Testing and Imaging Laboratory of the Dept. of Civil and Environmental Engineering, University of Houston, with testing assistance from her doctoral student, Mr. Prakash Bhat.

Finally, I would like to thank my friends and family for all of their support through my graduate student life. Without them, I would not still be sane. Thank you.

Multifunctional Carbon-Polymer Composites for Temperature Sensing and De-icing

An Abstract

of a

Dissertation

Presented to
the Faculty of the Department of Mechanical Engineering
University of Houston

In Partial Fulfillment
of the Requirements for the Degree
Doctorate of Philosophy
in Mechanical Engineering

by
Christiana Chang

August 2013

Abstract

This dissertation presents the work conducted on two major projects: 1) a structurally integrated, continuous carbon fiber heating element based polymer composite system for the de-icing of wind turbine blades and 2) modeling and experimental verification of piezoresistivity of carbon nanotube/nanofiber based polymer nanocomposite strain sensors. First, icing events on wind turbine blades not only cause a stop in production, but can also lead to serious structural damage to the turbine itself and surrounding structures. This work proposes a structurally integrated, continuous carbon fiber heating element wind turbine blade de-icing system, including an environmental condition based control system for heating actuation.

Next, a Monte Carlo based numerical simulation of electrical conduction through a carbon nanotube/nanofiber-polymer nanocomposite is presented. Carbon nanocomposites show great promise as structurally integrated, highly sensitive strain sensors due to their inherent piezoresistivity, but many mechanisms affecting their gauge factor, such as that of temperature, are not well understood. This dissertation presents modification made to an existing Monte Carlo simulation of nanocomposite resistivity, extending its functionality to predict piezoresistive properties dependent on composite temperature. The numerical model is verified with experimental results of carbon nanotube-epoxy nanocomposites under strain at varying sample temperatures.

Keywords: Carbon fiber, carbon nanofiber, carbon nanotube, nanocomposites, piezoresistivity, de-icing

Table of Contents

List of Figures

List of Tables

Symbols and Abbreviations

Symbol	Meaning
T	Temperature
V	Voltage
I	Current
R	Resistance
P	Power
ρ	Bulk Electrical Resistivity
L	Length
A	Cross-Sectional Area
σ	Bulk Electrical Conductivity
J	Current Density
h	Planck's Constant
d	Separation Distance between CNT
m	Mass of Electron
e	Charge of Electron
λ	Band Gap Energy of Insulating Film
D	Diameter of CNT
α	Co-efficient of Thermal Expansion (used interchangeably with Thermal Expansion Rate)
u	Short Fiber Length
v	Poisson's Ratio
E	Young's Modulus

ε	Strain
V_f	Volume Fraction of Fiber
V_m	Volume Fraction of Matrix
x, y, z	Rectangular Coordinates

Abbreviation	**Meaning**
CNT	Carbon Nanotube
CNF	Carbon Nanofiber
CTE	Coefficient of Thermal Expansion
CF	Carbon Fiber
DP	Dew Point
MWCNT	Multi-walled Carbon Nanotube
RVE	Representative Volume Element
PBC	Periodic Boundary Condition

Chapter 1 Introduction

1.1 MOTIVATION AND OBJECTIVES

1.1.1 Wind Turbine Blade Icing – Economy, Maintenance, and Safety Issues

For the profitability of wind energy resources, maximization of operation time is key to ensure continued production and a steady stream of product to sell to the consumer. Environmental factors, such as conditions for blade icing, often pose a threat to continuous operation of wind turbines and solutions must be developed to counter these environmental effects to keep the wind turbine online as often as possible. In areas such as the North Sea [1], blade icing is a common problem which can require the entire turbine to be completely stopped to prevent complications such as structural damage due to rotating mass imbalance and dangers to local buildings due to ice throw-off. For turbines installed in moist, freezing environments, an integrated anti- or de-icing strategy is needed to keep the turbine operational in a wider variety of environmental conditions to continue energy production.

Though in current practice a number of anti-icing strategies are used [2], including special blade coatings and anti-icing chemical sprays, they are of limited effectiveness and, in the case of sprays, difficult to apply in field sites. This paper proposes the use of laminated carbon fiber (CF) heating elements used in conjunction with advanced, robust electronic control strategies for a structurally integrated active de-icing system which can be operated on-site, either autonomously or with remote user control. A fiberglass-CF-epoxy laminate composite system was designed and tested for its ability to both deice (remove formed ice by melting) and prevent ice formation on the composite surface. In addition to the material system itself, a fuzzy logic based control strategy was designed to target the minimum power needed to maintain a 4°C surface set point at a variety of wind speeds. The performance and efficiency of the proposed

fuzzy logic control scheme was compared to the common on-off control strategy often used for temperature control. Finally, a field test of the proposed self-heating laminate system and control system was tested in Anchorage, Alaska.

1.1.2 Piezoresistive Carbon Nanocomposites – Modeling and Experimentation

Following the successful fabrication of the C60 fullerene, there has been an explosion of interest in nanoscale materials and the potential that they unlock due to their atomic scale dimensions and unique physical behaviors. Of particular interest have been carbon based nanomaterials due to both the availability of carbon, as compared to rare earth metals like indium used in current electronics, and their extraordinary theoretical materials properties, including high strength, chemical inertness, and high electrical and thermal conductivities. Furthermore, advanced research in composite materials has provided simple methods to incorporate these high performance properties into common structural materials such as fiber reinforced polymers and even cement. However, though these properties have been investigated extensively empirically, there is still much to be learned about the multi-scale origins of the properties in composite materials. Not only can these multi-scale investigations give us better understanding on the physical mechanisms of bulk properties, but development of analysis tools can also provide assistance in design of the bulk material by linking parameters, such as fiber loading fraction, fiber orientation, constituent electrical properties, and constituent mechanical properties, to bulk properties for material design.

The second half of this dissertation focuses on the numerical modeling of electrical resistance properties of carbon nanotube (CNT) – epoxy films with a focus on the effects of temperature. Particularly, this dissertation investigates the multi-scale effects of temperature on electrical transport properties, beginning with the effect of microstructure on electrical resistance between individual fibers in the matrix to the bulk material property of electrical resistance. A

Monte Carlo based simulation was developed and used in conjunction with common commercial software to investigate the effects of applied strain and temperature to the electrical resistance properties of CNT-epoxy films. In particular, this dissertation aims to connect mechanical properties of the constituents to the temperature based sensitivity of bulk electrical resistance from a microstructural approach. These numerical simulation results are further verified by experiment.

1.2 CONTRIBUTION AND SIGNIFICANCE OF THE RESEARCH IN THIS DISSERTATION

This dissertation aims to further research in application of functional carbon reinforced structural composite, particularly in the areas of sensing, instrumentation, and design of not only the structural material itself, but also the supporting control technologies. Since this dissertation is comprised on two main projects, the contributions of this dissertation can be divided as such:

1.2.1 Contributions of Laminate De-icing Project:

- A structurally integrated, carbon fiber reinforced fiberglass-epoxy laminate material was designed and tested for de-icing and anti-icing performance, with a targeted application in wind energy industries. The structural material successfully removed formed ice and prevented ice formation in both laboratory and field settings.
- A robust, fuzzy logic based power controller was designed and tested to regulate the surface temperature of the proposed laminate plate while maintaining heating energy efficiency. The developed fuzzy logic rule base was empirically developed based on sample testing of the material system using a simple laboratory test. This controller can take into account wind speed and local

humidity conditions to adjust power consumption, functionalities that existing power controllers for similar composite de-icing systems lacks.

- Performance comparison of the proposed fuzzy logic controller to common on-off control shows that not only is the fuzzy logic controller more energy efficient, but that it is also more effective in de-icing and anti-icing functions due to an enlarged heating footprint. This result supports the use of more advanced controllers for de-icing applications to maximize effectiveness despite the simplicity of implementation of on-off control.
- Material tests show that the proposed heating scheme does not adversely affect the tensile properties of the proposed laminate system, indicating that the embedded heating element scheme will not shorten operation life of the wind turbine blade or compromise its structural integrity during operation.

1.2.2 Contributions of Electrical Resistance Modeling with Temperature Effect

- Using analytical models of thermal expansion of CNT filled epoxy composites, the developed Monte Carlo model links fiber orientation due to thermal expansion to observed changes in bulk electrical resistivity due to temperature change. While this effect has been observed and thermal expansion suspected, the presented numerical model directly links the effect of thermal expansion on the composite microstructure to the observed bulk behavior.
- Experimental results verify with great accuracy the temperature threshold between thermal expansion and contraction of the CNT-epoxy composite, as verified by electrical resistance measurements. The experimental results verify the proposed numerical model and provide important threshold points (change between thermal expansion and contraction, threshold of network breakdown) for

applications of the composite as a temperature sensor or for temperature compensation in strain sensors.

1.2.3 Significance of Research

This dissertation presents an integrated de-icing system, including the material system and supporting power control architecture, as a proof of concept for wind turbine blade de-icing applications. Though similar material system technology exists in industry, a major obstacle to profitability is a lack of power control strategies to maximize effectiveness and minimize energy costs. The results of this dissertation show that not only can simple, single temperature measurement based control strategies be used to significantly reduce power consumption, but that advanced controllers can increase the heated area while significantly reducing energy usage as compared to traditional temperature control. This dissertation provides a first step toward the design of a complete de-icing system which includes the heating element and the supporting sensing, actuating, and control architecture and algorithms to improve heating system effectiveness.

Additionally, this dissertation presents and important link between thermal expansion of CNT-epoxy composites, changes in composite microstructure due to temperature changes, and the observed electrical resistivity change in the bulk material, a link that had previously not been demonstrated in literature though the empirical behavior had been observed. With the link demonstrated, the proposed numerical model can also be used as a design tool to allow material scientists to tailor the sensitivity of the proposed composite system for temperature sensing by simulating the effect of parameters such as filler loading, matrix bandgap, filler aspect ratio, and filler orientation. Additionally, the proposed model can also be used as analysis tool to help decouple the temperature induced resistivity change from applied strain induced changes, an important step in improving the accuracy of the proposed strain sensor.

1.3 ORGANIZATION OF THIS DISSERTATION

This dissertation is organized in the following manner:

- Chapter 1 presents the introduction to the topics discussed in this dissertation. In particular, this chapter presents the motivation for the development of multifunctional, carbon reinforced polymer composites and their possible applications as both structural materials and electronic sensors. This chapter also presents the significance of the presented research and the organization of the dissertation.

- Chapter 2 presents a literature review of carbon reinforced polymer composites and their engineering applications. General observations of carbon fiber reinforced polymer composites are presented, followed by discussions of the great potential of carbon nanoparticle reinforced polymer composites.

- Chapter 3 presents a literature review of wind turbine blade de-icing research and discusses the motivation for a structurally integrated, intelligently controlled carbon fiber based de-icing system.

- Chapter 4 presents the work done on the development of a structurally integrated, carbon fiber based self heating laminate composite specifically targeted for wind turbine blade de-icing applications. This chapter includes laboratory work on the development of an intelligent, fuzzy logic controller for power control of the self heating laminate panel as well as

field testing of small scale wind turbine blades equipped with the self heating laminate material.

- Chapter 5 presents an experimental investigation of the effect of repeated thermal cycling of the proposed carbon fiber based self heating laminate system on the tensile mechanical properties of the laminate material. The chapter focuses on laboratory testing of coupon samples to characterize the progression of mechanical properties with increased thermal cycling loading.

- Chapter 6 presents a Monte Carlo based simulation of electrical resistivity of carbon nanotube filled polymer composites, with particular interest in the effect of temperature on the composite's electrical properties. The chapter presents the development of the computational Monte Carlo resistivity model, the numerical simulation results, and the experimental verification of the simulation results using a carbon nanotube-epoxy composite film material system.

- Chapter 7 presents the major conclusions and observations drawn from the work presented in Chapters 4-6, as well as proposals for future work to extend the findings presented in this dissertation.

Chapter 2 Carbon-Polymer Composites and Their Applications

2.1 RISE OF COMPOSITES AS HIGHLY FUNCTIONAL STRUCTURAL MATERIALS

Composite materials, or materials comprised of distinctive constituent materials but have a bulk behavior that is unlike its individual constituents, have long been used as structural materials, even before humans understood composites in the engineering sense. From straw-mud huts to Roman concrete, humans have understood that blending together the right matrices with the right reinforcements results in a combination of traits from the matrix and reinforcement, leaving us with structural materials that have the required strength and give us additional flexibility of use. For example, concrete allows us to harvest the high compressive strength of stone while bonding with cement allows us to pour the uncured composite mixture into any shape we need, a benefit that is not provided by stone alone.

Though composites have been in use for centuries, it is only more recently that intensive study of the art of blending the matrix and reinforcement has lead us to engineering composites designed for certain performances. Particularly of interest are functional composites, or composites which are granted other abilities due to the design of the matrix and reinforcement [3]. In addition to strength, these functionalities can range from chemical sensing [4], electrical and thermal transport properties [5][6], mechanical sensing [7][8], self-healing properties [9][10], improved damping [11], and actuation abilities [12][13]. By careful selection of constituent materials and fabrication, modern structural composites have the ability to not only serve as structural component to support loads, but can provide structurally integrated functionalities which reduces the need for additional instrumentation to be added onto the structure itself.

A wide variety of functional structural composites have been demonstrated in the last two decades. At the most basic level, there has been great work into making structural composites which are able to provide tailored transport properties for high performance structural systems. Berghaus et al. proposed an alumina-zirconia based ceramic composite spray for abrasion protection and improved thermal surface barriers [14]. On the other end of the spectrum, Every et al. [15] analyzed the effect of filler size on the thermal conductivity of Zn-diamond particle filled composites. Though diamond has the highest known thermal conductivity, their modeling and experimental work showed that the composite thermal conductivity is highly dependent on filler particle size due to increased thermal barrier dominance as the particle surface area to volume ratio increases. Additionally, to overcome the inherent low electrical resistance of polymers, there has been a large body of research to improve electron transport in polymers for the sake of EMI shielding [3][16]. Kim et al. [17] demonstrated a purely polmer composite (polyester and polypyrrole) composite made through electrochemical polymerization with a volume resistivity as low as 0.2Ω and EMI shielding performance of 36dB over a wide frequency range up to 1.5GHz, making it comparable to some metals.

In addition to these more passive functional composites, there has been great research into composites with targeted responsive functions, such as damage repair and healing. Kessler et al. [9] and White et al. [10] broke ground by proposing self-healing (autonomic healing) polymer composites containing microencapsulated healing agents in the reinforcement and solid chemical catalysts dispersed within the matrix. Room temperature healing allowed a cantilevered beam with mid-plane delamination to recover up to 45% of the uncracked fracture toughness; elevated healing temperatures allowed recovery up to 80%. Extending upon this idea, Tee et al. [18] designed a pressure and flexural sensitive organic polymer composite skin using nanostructured nickel microparticles that exhibited self healing properties. In their work, recovery of electrical conductivity post healing was as high as 90% after 15 seconds of healing, with mechanical

properties restored after 10 minutes of healing, making their organic matrix composite ideal for biomimetic skins for robotics and prostheses. Li et al. [19] further proposed similar self healing cementitious composites using their strain hardening polyvinyl alcohol (PVA) fiber reinforced engineered cementitious composite (ECC) and hollow glass fibers filled with superglue.

In addition to healing properties of composites, there have been numerous developments in making structural composites into their own actuators and sensors. Yehia et al. demonstrated that a combination of steel fibers and carbon fiber in concrete enables the concrete enough electrical conductance to serve as its own heating element, allowing a concrete bridge overlay to heat itself and remove surface ice [13] [20], allowing a common structural material to act as its own thermal actuator. Sodano et al. [21] demonstrated the improved performance of macro-fiber composites (MFC) over traditional piezoceramic actuators and sensors for inflatable structures. While piezoceramics are brittle and are limited to low strain, MFCs use piezoelectric fibers in piezoelectric polymer matrices (such as PVDF) to form flexible, durable strain sensors and actuators for dynamic measurement, enabling their use as structurally integrated vibration suppression systems. Shape memory alloys (SMA) have also been proposed for self-actuating composites in a number of different schemes. Song et al. [22] demonstrated active position control of a honeycomb composite sandwich beam with embedded SMA wires, using a robust feed-forward compensator to take into account SMA's hysteretic and non-linear behavior. In another approach, Boyd and Lagoudas [23] proposed a short SMA fiber reinforced composite and used the Mori-Tanaka averaging scheme to estimate thermomechanical properties due to the temperature induced SMA phase transformation.

In addition to these examples of functional composites, there is a great focus (in which this dissertation takes part) in the area of functional carbon reinforced composites. Carbon is a highly abundant material which has fantastic mechanical, electrical, and thermal properties [3][16], making it an ideal reinforcement material for functional composites. The following two

sections will focus on two categories of carbon reinforced composites relevant to this dissertation: carbon fiber reinforced composites and carbon nanocomposites.

2.2 CONTINUOUS AND SHORT FIBER CARBON FIBER COMPOSITES

Currently, most carbon reinforced composites refer to macro fiber reinforced composites made from carbon fiber yarns drawn from polyacrylonitrile (PAN) or pitch precursors. Most commonly, the term "carbon fiber composite" brings to mind continuous fiber reinforced composite due to their use in commercial products such as car bodies and high performance sports equipment. In addition to high strength, continuous carbon fiber reinforcements impart some piezoresistivity to polymer composites due to conductive network break down as the material is strained and deformed [24]. Wang et al. [25] showed that clever design of the CF lay-up to form grids within the larger laminate structure could be used for localized damage detection, as reductions in electrical conductivity could be traced through the known possible conduction paths through the CF. A similar technique was used by Irving and Thiagarajan [26], who used unidirectional axial and cross-ply carbon fiber in laminate composites to monitor static stress loads and fatigue damage using electrical potential measurements. Their results indicate that degradation of electrical conduction properties accumulates during fatigue and that thresholds can be determined to provide early indication of fatigue damage.

However, use of continue CF requires complicated fabrication techniques to place the CF in a lay-up prior to application of the matrix. Short fibers, or cut CF on the length of a few microns to several millimeters, can easily be mixed into cured or uncured matrices and be shaped, by processes such as drawing and injection, more easily than by lay-up. In another damage detection approach, Weber and Schwartz used a CF damage model to explain increases in resistance with fatigue in short carbon fiber reinforced polymer (CFRP) epoxy laminate samples [27].

In her extensive research work on short carbon fiber composites, Chung et al. demonstrated that short fiber reinforced composites, particularly those of cementitious nature, could be used for strain sensing, EMI shielding, and temperature sensing [28]. In particular, carbon fiber polymer and cementitious composites were observed to have an activation energy based relationship between electrical resistance and temperature, allowing short carbon fiber reinforced composites to be used as highly sensitive thermistors [7]. This was reinforced by the activation energy electrical resistance behavior observed by Chrisp [8]. Thus, cementitious carbon fiber reinforced structural materials, including concrete and mortars, are ideal self-sensing structural materials as they can detect their own strain and temperature variations directly, without the need for additional sensors.

2.3 MATERIAL OF THE CENTURY? – CARBON NANOPARTICLES AND NANOCOMPOSITES

In recent years, perhaps the most focus has fallen on carbon nanoparticle reinforced composites [29][30], particularly those based around carbon nanotubes and its variations [16][31] [32]. Due to their high performance theoretical properties [33], such as electron and phonon mobility [34][35], and improved percolation behavior at low filler loadings [6][36][37], carbon nanoparticle reinforced composites are believed to hold a plethora of high performance functional composites which can be made from readily available material sources. Using both piezoresistive polymer matrices [38] and the network break down due to strain [6], a number of researchers have proposed CNT [31][39][40][41] or graphene based strain sensors. Kang et al. [31] used single walled CNT-poly-methyl methacrylate (PMMA) composite system to develop a high sensitivity strain sensor for dynamic strain measurements of structures. To perform the sensing duty, they formed their CNT-PMMA composites into long strips, called neurons, to perform local strain and crack growth monitoring within a artificial neural system (ANS) to aggregate results

from multiple sensors. Hu et al. conducted extensive work with CNT-epoxy film systems to both experimentally test the piezoresistive sensitivity of their developed film and to model the microstructural origins of the piezoelectric effect [42][39]. In their findings, Hu et al. [39][40] found that CNT-epoxy strain sensor sensitivity can be tuned by varying CNT loading, curing temperature, stirring/dispersion rate, CNT diameter, and the barrier energy height of the polymer matrix. These results were also supported by extensive numerical modeling of the system microstructure. In addition to polymer matrices, similar strain sensing abilities have been investigated in cementitious composites using carbon nanofibers. Gao et al. studied the improvement of electrical transport using self-consolidating concrete (SCC) and carbon nanofiber (CNF) based concrete samples. His investigation showed that with improved fiber dispersion due to the low viscosity of SCC, strain sensitivity of CNF-concrete composites was greatly improved [43].

Other than structural strain measurements, carbon nanoparticle filled composites have been seen to have many sensing, EMI, and actuation functionalities. Kuila et al.'s review of graphene-polymer composites [38] showed that graphene not only allows the creation of epoxy composites with high heat dissipation capacity, EMI shielding capabilities, and strain sensing for various polymer matrices, but also that poly-vinyl diflouride's (PVDF) inherent piezoelectric properties are enhanced with graphene processing, leading to transparent, flexible conducting polymer materials with high thermal stability. Such polymer film has already seen research to move production to commercial scales, as demonstrated by the roll-to-roll fabrication technique of transparent graphene electrode films described by Bae et al. [44]. Additionally, the morphological properties of well dispersed graphene in polymer matrices resulted in composites with improved gas barrier properties, with successful suppression of N_2 and He permeation. Wei et al. [45] proposed highly selective, multifunctional chemical vapor sensors using aligned CNTs in polymer matrices. In their work, as synthesized, aligned CNT arrays without polymer matrices

were compared to composite films formed with the aligned CNT arrays and poly(vinyle acetate) PVAc. Results showed a reversible 130% increase in electrical resistance of the CNT-composite film in the presence tetrahydrofuran (THF) vapor, while the pure CNT array showed no change in resistivity. A broad review of CNT based chemical sensors by Sinha et al. [46] indicates that similar technology can be used to sense a wide array of gases and chemicals in the food, automotive, and health industries.

2.4 SUMMARY OF LITERATURE

The existing literature shows that there is great potential for functional composite materials to provide numerous improved transport properties, actuation, and sensing properties to structural materials, allowing them not only operate within systems more efficiently but to also provide information about themselves and to react to their environment. While the field of functional composites is a broad area which encompasses many different types of material systems, there is a large focus on carbon based composites both due to its abundance and its unique material properties. This chapter provided a brief overview of current research in carbon based functional structural composites, containing both macro fibers and carbon nanoparticles. The following chapters will provide current work on the use of both macro- and nano-scale carbon reinforcements in polymer composites in the development of functional composites for heating and strain and temperature sensing.

Chapter 3 Development of Carbon Fiber Heating Element Based Wind Turbine Blade De-icing System

3.1 INTRODUCTION

With the looming knowledge of limited fossil fuel supplies, it has become a global concern to develop clean, efficient, and reliable alternative energy sources to power our world's electricity needs well into the future. While there is much competition in the field, modern wind energy harvesting technologies are amongst the most mature and commercially viable, with many large scale "wind farms" operational and many more in proposal. However, wind energy production is highly dependent on a number of uncontrollable environmental factors, such has the actual wind speed, presence of rain and lightening, and, in certain regions, formation of ice on the wind turbine blades [1][47]. Though modern wind turbine energy harvesters have grown to multi- megawatt capacities, these rated capacities are only the potential production under ideal conditions. In unfavorable conditions, energy production may be cut down to a fraction of the rated capacity, or in certain cases, completely stopped to product the electrical grid or the wind turbine structure itself [48].

This chapter focuses on a proposed solution for the problem of wind turbine blade icing – a structurally integrated carbon fiber (CF) based polymer matrix laminate system with self-heating capabilities. First, a literature review of current technology for wind turbine blade de-icing and carbon fiber composites in the wind energy industry is presented. Then, the system design for the proposed CF-based self-heating laminate composite is presented with some preliminary experimental work to guide the heating control system design. Next, the design and testing of robust fuzzy logic power control systems for de-icing and anti-icing of laminate composite plate samples is presented and discussed. Then, the site installation of a small scale, mock-up wind turbine system with the proposed CF-based de-icing system is presented with field

testing results. Finally, the overall results are discussed with comments on future directions for system development.

3.2 State of Art in Wind Turbine Blade Counter-Icing Strategies

As our energy needs grow and our understanding of wind resources improves, construction of wind farm sites in areas of extreme, wind rich weather climates is becoming more common. In particular, wind turbine operation in cold climates in Europe, North America, and Asia has grown in the last decade [49]. Though these cold regions may have rich wind resources, wind turbines in these areas are susceptible to blade icing, which can significantly modify the aerodynamic performance and increase structural loads due to the increased, unbalanced mass [50]. In Scandanavia, an estimated 1.1% - 1.5% of estimated production losses were due to cold climate and icing [51]. These production stoppages are predicted increase as more wind turbine plants are designed to operate offshore to harness greater wind energy capacity at the risk of more exposure to moisture [50][51]. Furthermore, the risk of ice shedding throwing large blocks of ice onto nearby settlements could endanger residents and service personnel [52][52]. Thus, special attention should be paid to wind turbine blades which are designed for operation in cold climates to ensure steady production, safe operation, and prolonged structural life [53]. Currently, in the case of a severe icing event, operators completely shut the wind turbine down, halting production [1][48].

To counter the formation of ice on wind turbine blades, two approaches are currently taken: the anti-icing approach and the active de-icing approach [2][47][49]. In the case of anti-icing, strategies are targeted toward the prevention of ice formation on the blade surfaces. Special ice-phobic coatings and chemical sprays which lower water's freezing point have been proposed, but they are limited in their effectiveness and, in the case of sprays, are impractical in real field implementations [2]. Active de-icing systems, such as heating systems [54][55][56] or

active-pitch systems, add energy to the system to provide de-icing functions and are more effective through a range of environmental conditions, but have high energy consumption, particularly in heating based strategies. Active pitch systems use the motors built into the base of the blade, usually used to turn the blades into the wind to regulate power production, to turn the blades into the sun and melt ice off the surface [2]. However, this still requires production to be shut off while the blades are repositioned and stalled during the de-icing process. While dark colored coatings have made this solar based de-icing approach more efficient, there are still limitations due to sunlight availability and range of operable temperature conditions.

A more effective active de-icing approach has been active heating of the turbine blades themselves. In terms of production capacity, power estimates for resistive heating based strategies vary from as little 1-4% of turbine capacity to as much as 14% of capacity, depending on environmental conditions and turbine size [2][49]. A variety of strategies to provide heat to the turbine blades have been proposed. Boyd et al. [55] proposed an intermittent warm air heating system which would blow heated air down the length of the blade inside of the hollow, box girder supported blade shell. However, reviews of this approach found it to be energy inefficient, as the energy transfer from the air to the blade skin was inefficient and additional energy was needed to run the fans to blow the air down the blade, limiting its reach [2]. Kelley Aerospace [57] has developed a surface mounted heated sheath which can be installed over the blades and heated to melt ice of the blade surface. However, this material is installed post production and is an additional add-on to the structure, possibly affecting the aerodynamics of the blade. Though a commercial, carbon fiber heating element based active de-icing system has been deployed in the North Sea [54], robust control systems based on local icing conditions are still lacking to automate the operation of the de-icing system and to reduce power consumption. The development of robust ice sensors, modeling of icing conditions, and design of energy efficient, multi-input control algorithms is needed to make operation of heating element based de-icing

systems effective and cost efficient in terms of power consumption as a portion of wind turbine power capacity.

3.3 DE-ICING SYSTEM DESIGN

Prior to design of the controller system, some basic tests to understand the behavior of the proposed self-heating laminate system were performed. To explore the heating properties of the proposed CF laminate, small plate samples were first used to investigate the temperature distribution and power requirements during heating in the plane of the composite plate.

3.3.1 Sample Fabrication and Dimensions

7-in×7-in fiberglass-epoxy composite plates were fabricated by hand lay-up with a 2-in wide carbon fiber tape laminated below the surface layer of fiberglass as the resistive heating element. During curing, the composite was vacuumed bagged to 25" Hg for 24 hours at room temperature (approximately 25°C), after which the plate was taken off of the mold and allowed to air cure for an additional 24 hours. To record the temperature profile of the plate samples, a thermocouple was surface mounted as given in the schematic presented in Figure 3. A photo of the specimen without gel coat is presented in Figure 2. Properties of the carbon fiber, fiberglass, and epoxy are given in Table 1.

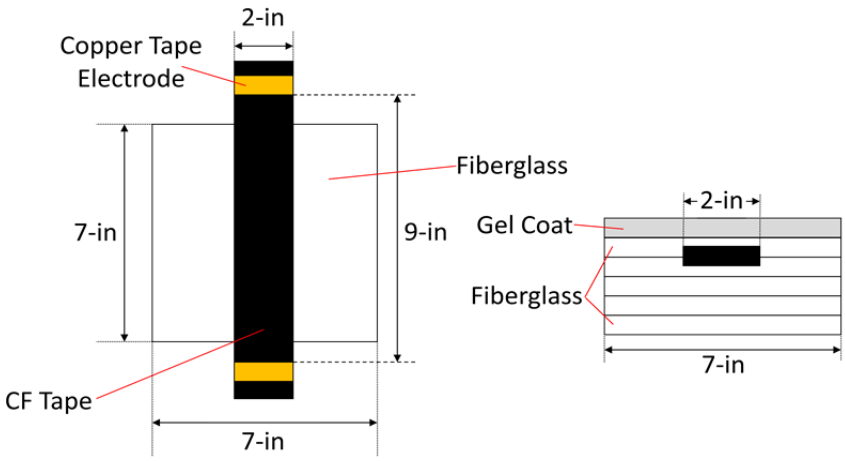

Figure 1: Schematic of composite plate sample for lab testing

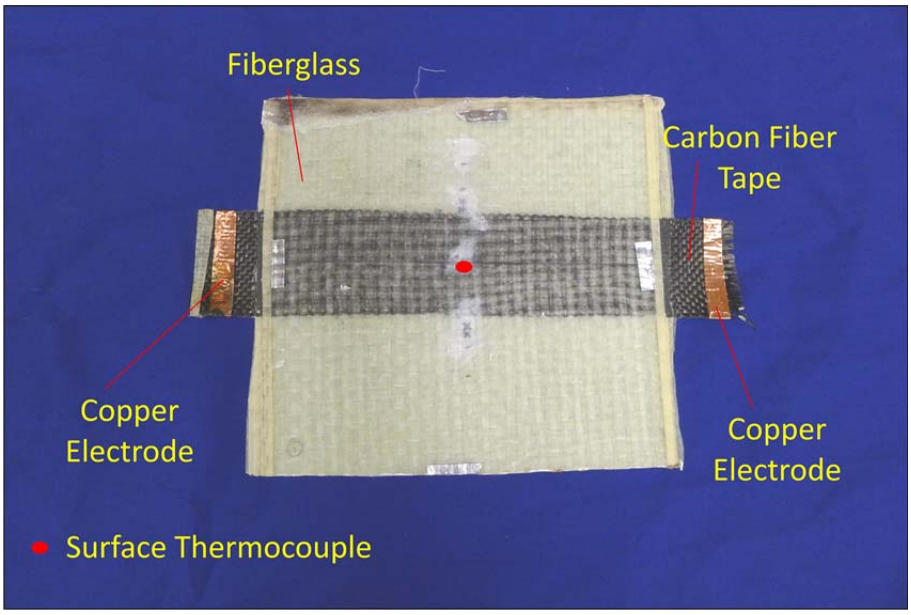

Figure 2: Photo of composite plate sample (without gel coat)

Table 1: Typical Material Properties

	Epoxy	Fiberglass	Carbon Fiber
Specific Heat	1.0 kJ/kg-K	0.764 kJ/kg-K	0.8 kJ/kg-K
Thermal Conductivity	0.25 W/m-K	1.0 W/m-K	8.50 W/m-K
Linear Thermal Expansion Coefficient	74.7 µm/m-K	5.3 µm/m-K	-0.600 µm/m-K
Young's Modulus	17 GPa	73 GPa	231 GPa

3.3.2 In Plane Heating Distribution of CF-Epoxy Laminate Plates

First, to understand the basic heating behavior of the embedded CF tapes in the laminate, the in-plane heating distribution was examine by measurements of temperature as the CF tape was used as a resistive heating element. To measure the in-plane temperature distribution, six thermocouples were surface mounted using thermal compound at positions indicated in Figure 3.

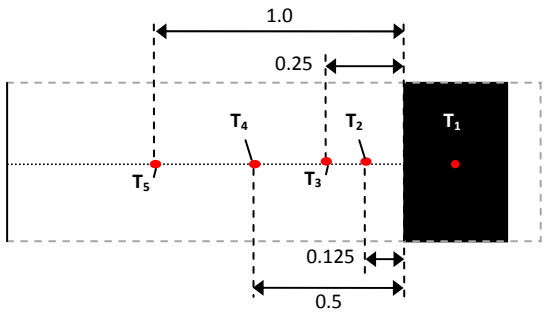

Figure 3: Placement of Thermocouples (dimensions in inches)

Two tests were conducted to examine the temperature distribution on the surface of the composite plate as the CF tape heats the plate surface; first, a constant voltage was applied to the two ends of the CF tape and the temperature monitored as the surface temperature was allowed to heat to equilibrium. Second, as the temperature directly above the CF tape was expected to be the highest, a simple on-off controller was used to maintain the T_1 temperature at +4°C with an applied voltage of 10V, in line with our ultimate de-icing goals. Once T_1 reached our target temperature, the T_1 temperature was maintained and the temperature data for all sensors recorded for an additional period of 15 minutes. For both tests, a FLIR infrared thermal imaging camera was also used at the intervals of 0, 1, 2, 5, 10, and 15 minutes after the beginning of heating to capture a more complete view of the instantaneous temperature distribution.

A sample set of results from the constant voltage to equilibrium tests is shown in Figure 4. From the temperature history, it can be seen that as we move away from the CF tape, the temperature of the plate drops significantly over a very short distance, most notably in the first

interval (between T1 and T2) where the temperature drops from 94.3°C above the CF tape to 43.4°C only 1/4" from the edge of the tape. The temperature continues to drop as we move further from the edge of the CF tape, but at a much reduced rate. Thus, it can be seen that at the CF-fiberglass transition in the in-plane direction of the plate there is a steep temperature gradient, consistent with the poor thermal conduction properties of both the epoxy matrix and fiberglass reinforcement. However, it should also be verified that the temperature distribution directly above the CF tape is even and that this temperature drop is indeed localized to the CF-fiberglass interface.

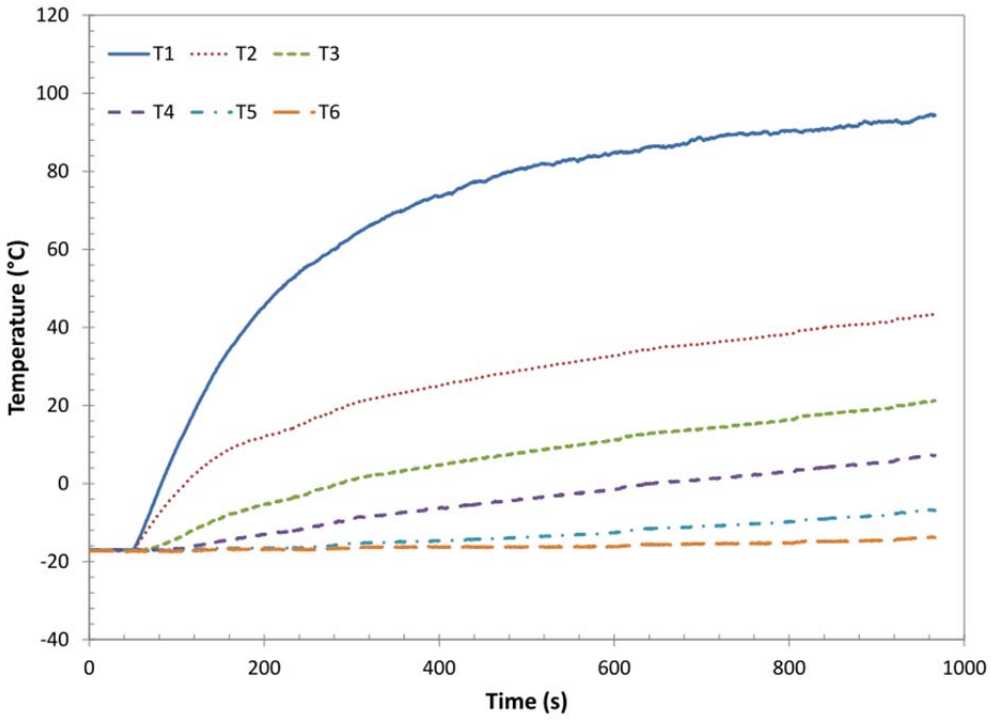

Figure 4: Temperature distribution with 10V applied

From the thermal images, it can be seen that, indeed, the area immediately above the CF tape is heated evenly at that there is no significant temperature drop as we move away from the center of the CF tape toward the CF tape edge. Furthermore, the steep temperature gradient at the edge of the CF tape is better visualized. The thermal images show that the temperature abruptly

drops at the edge of the CF tape and that the edges of the plate sample are very near the ambient temperature of the environment. The progression of thermal images also shows that this steep temperature gradient develops quickly and is evident almost as soon as the power to the CF tape is turned on.

Similar results are achieved in the controlled T_0 temperature tests, though the difference in temperature from the CF tape to pure fiberglass in the top-down view is reduced due to the reduced heating load of the CF tape. A sample heating temperature history is given in Figure 5 and the thermal images in Figure 6. As with the plate heated to equilibrium, in both the temperature history and thermal images we can see a significant drop in temperature as we transition from the CF tape footprint to areas composed purely of epoxy and fiberglass, though the total temperature difference is much reduced (7.8°C over ¼").

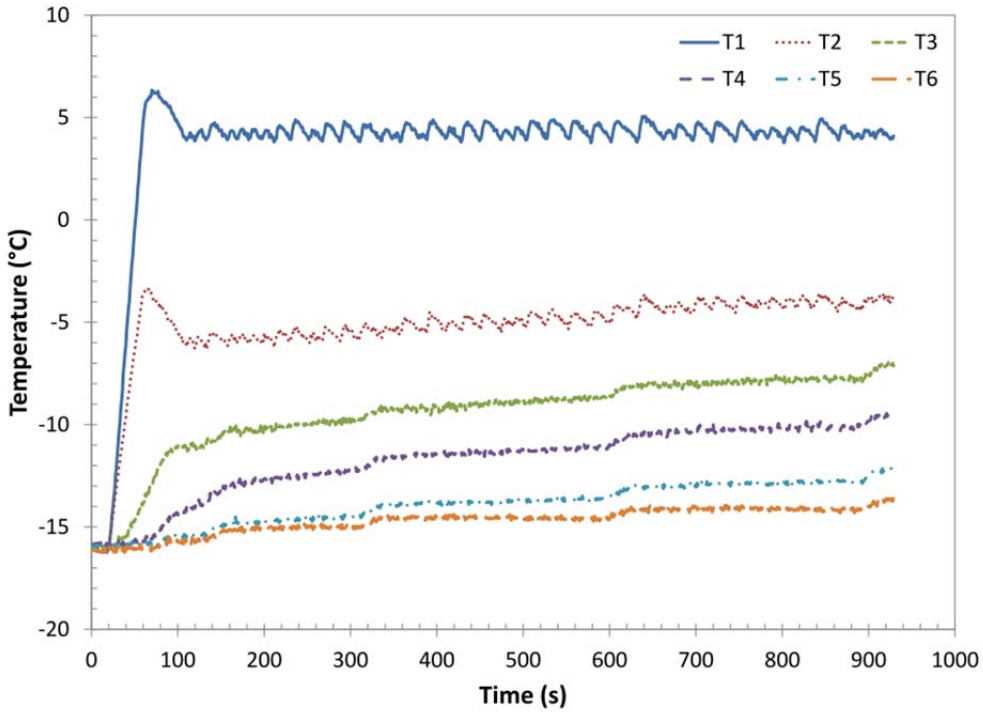

Figure 5: Temperature history with 10V applied (controlled heating)

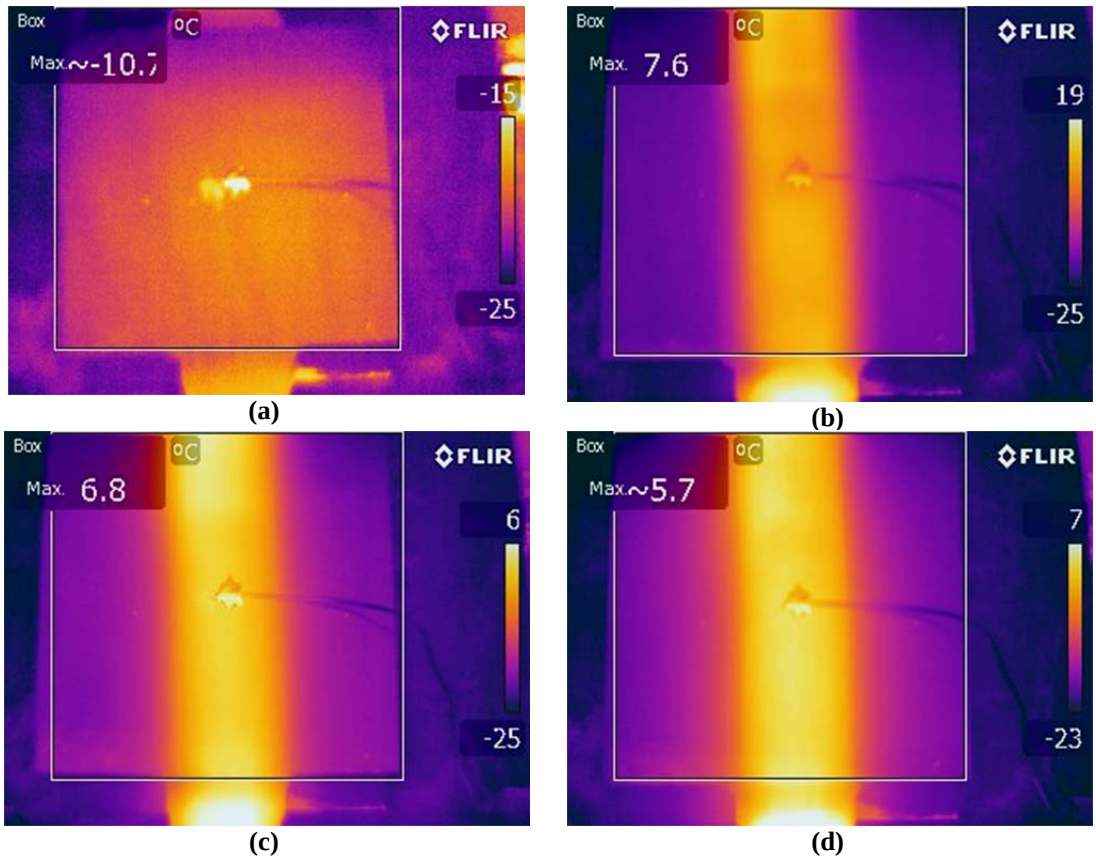

Figure 6: Thermal images of plate with controlled heating after (a) 0 minutes, (b) 1 minute, (c) 5 minutes, and (d) 10 minutes

From these two temperature distribution tests, it is concluded that heating of the composite beyond the immediate footprint of the CF tape, that is, the area above the CF tape, is not sufficient to support de-icing functions. Even in the instance of controlled heating, there is a significant temperature gradient at the CF tape interface, beyond which the temperature drops off very quickly to the ambient freezing temperature. Thus, it was decided that in the control design, only the temperature immediately above the CF tape at the surface need be taken into account and that the placement of the temperature sensor can be anywhere within the CF tape footprint without significant variation in measured temperature. This allows us to significantly reduce the number of required sensors for accurate control of the heating system and simplifies the control design process.

3.4 DEVELOPMENT OF FUZZY ENVIRONMENTAL FEEDBACK CONTROLLER

In order to provide a basis for the fuzzy rule base for power regulation based on the wind speed, an on/off controller was used to maintain the surface temperature of the plate at a set point of 4°C for wind speeds ranging from 0 to 40km/hour spaced at 10km/hour intervals. Tests were conducted in a freezer with an average air temperature of -15ºC. Relative wind was simulated using a blower with controllable speed. To separate the blower output from the ambient air in the freezer, a flow isolator was constructed with a section of flow straighteners, as described in Figure 7. Power was provided to the carbon fiber tape by a programmable power supply regulated by pulse width modulation (PWM) through mechanical relay. The duty cycle of the relay board was controlled through our design LabView Virtual Instrument (VI), which contains designs for manual, on/off and fuzzy logic control. A carrying wave frequency of 1Hz was used in the fuzzy logic controller design. A block diagram of the general experimental set-up is given in Figure 9. A photo of the experimental set-up is given in Figure 8.

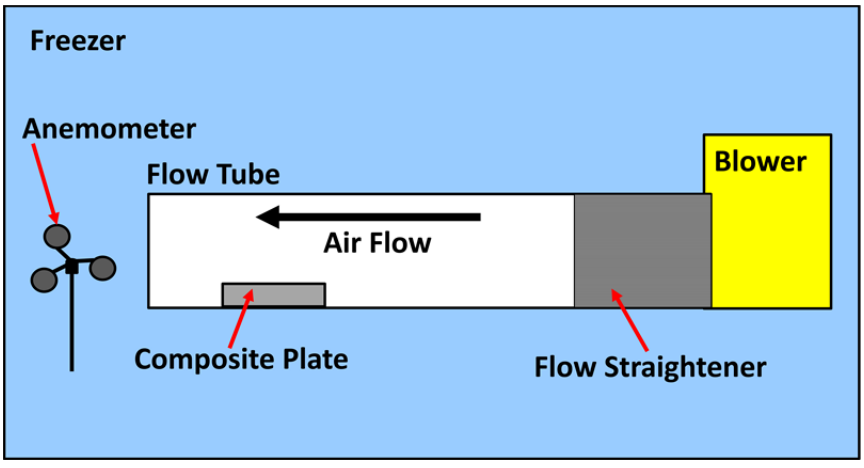

Figure 7: Schematic of Test System with Wind Blower

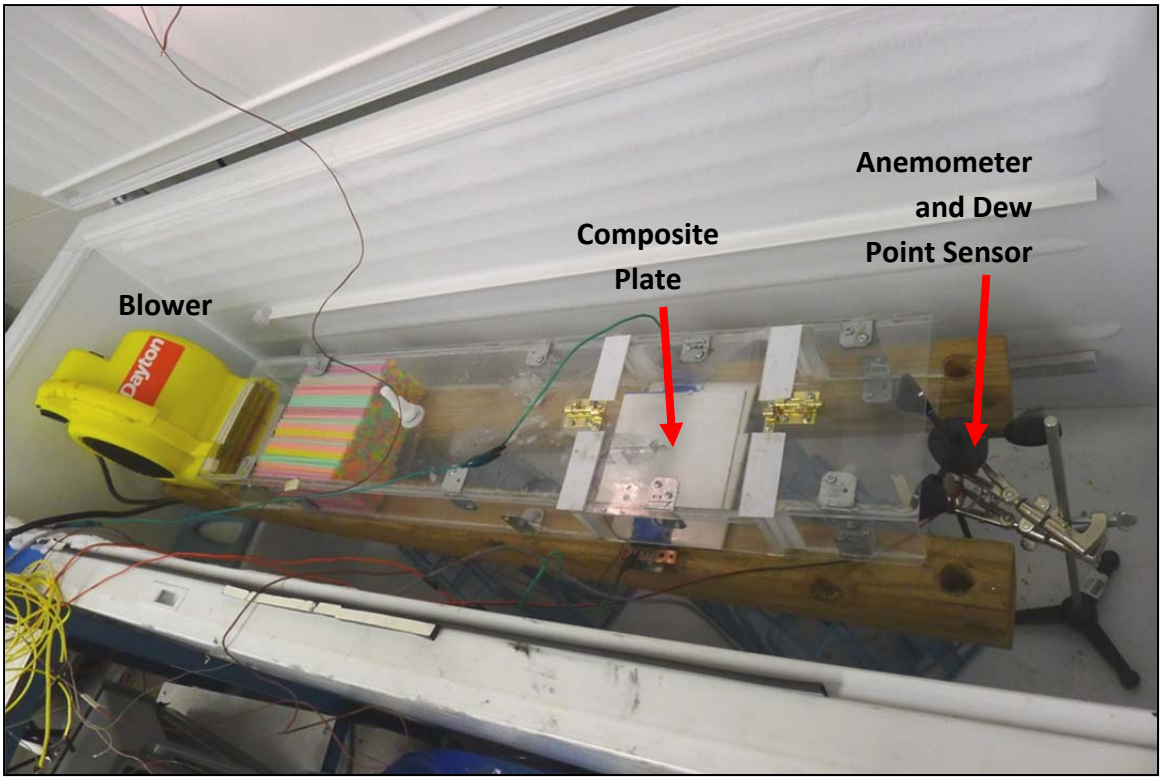

Figure 8: Photo of Composite Plate Control Test System

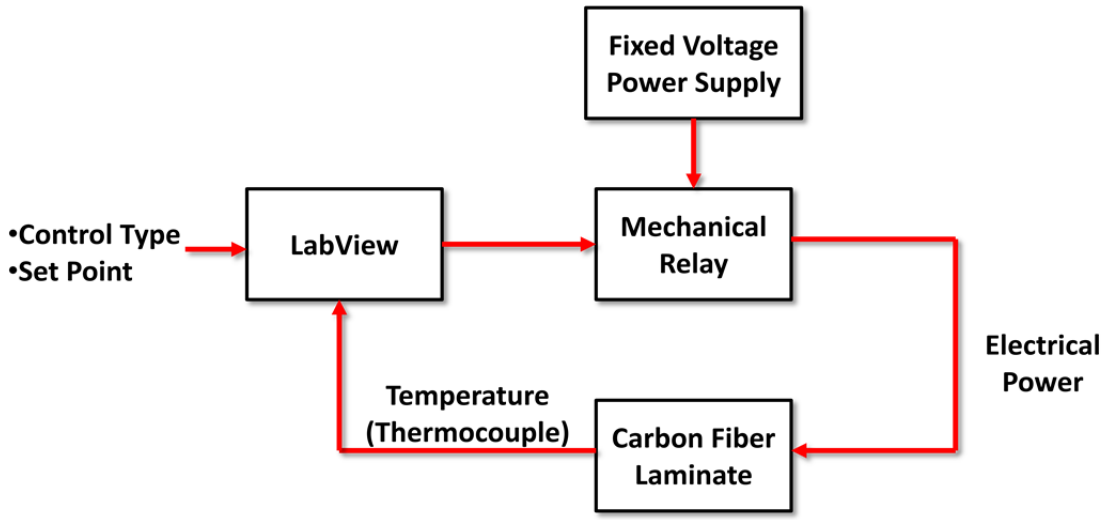

Figure 9: Block diagram of lab-scale experimental set-up

With the wind speed held constant, the on/off controller was used to bring the plate up to the set point temperature and used to maintain the set point temperature for at least 10 minutes. The average power usage during the 10 minutes of maintained set point temperature was taken as

the minimum power level needed to maintain the set point temperature at a given wind speed. A sample of the fixed wind speed test using on/off control is given in Figure 10.

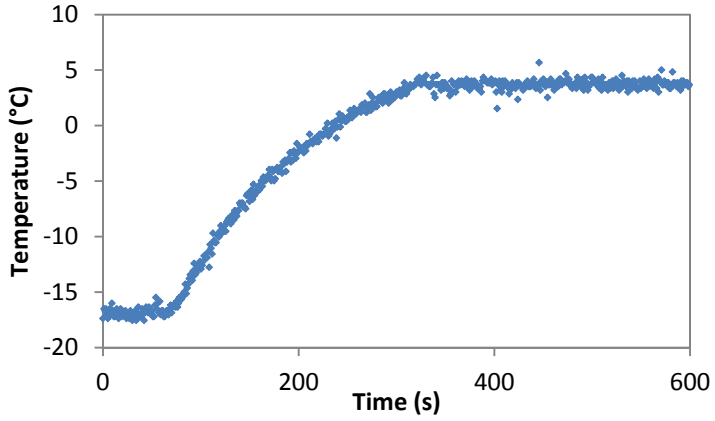

Figure 10: ON/OFF Heating at 10km/hour Wind Speed – 4°C Set Point

Based on the heating performance of the plate operating in different wind speeds, the fuzzy logic rule base was designed. A fuzzy logic controller was implemented in LabView with the rule base dependent on the plate surface temperature and the relative wind speed, as shown in the block diagram presented in Figure 11. The developed rule base is presented in Figure 12. The range is given by temperature in °C and wind speed in km/hour in Figure 12a and Figure 12b, respectively. Based on previous results, it was found that the surface temperature directly above the CF tape was sufficient for temperature control for de-icing purposes. To control the power supply to the CF tape, the fuzzy logic controller provides decisions on the duty cycle length of the PWM constant voltage power supply. The fuzzy logic duty cycle output set based on surface temperature and wind speed is summarized in Table 2 and Figure 13.

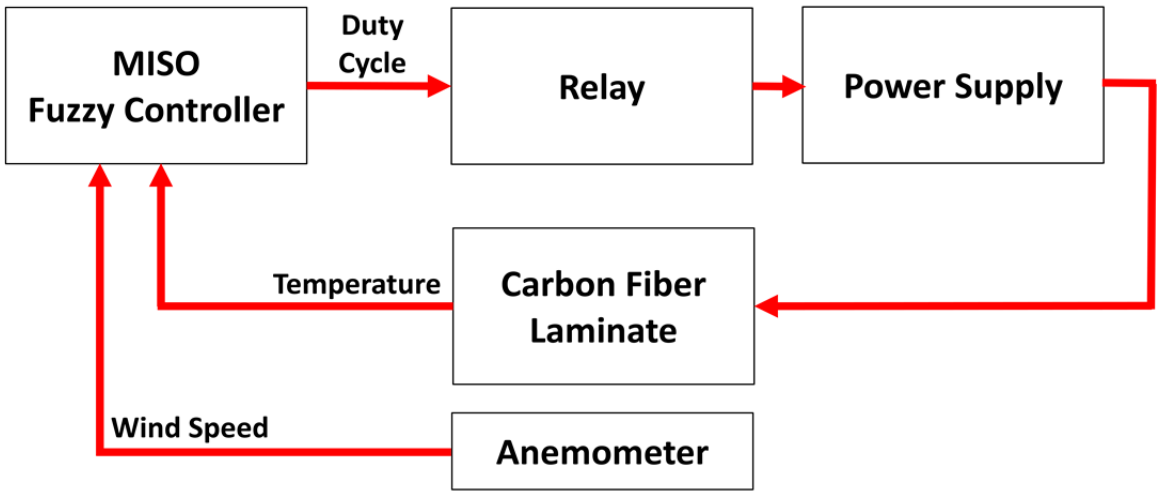

Figure 11: Block diagram of fuzzy logic feedback system

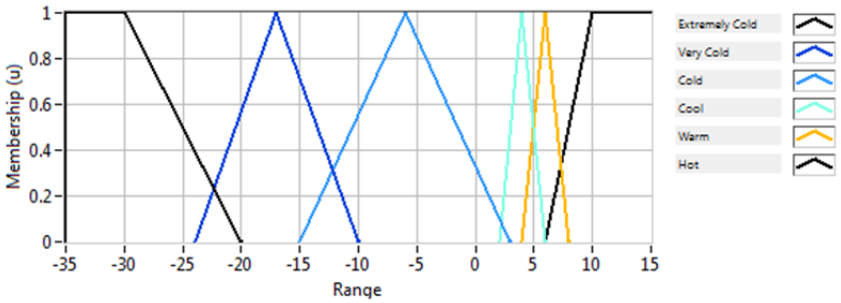

(a)

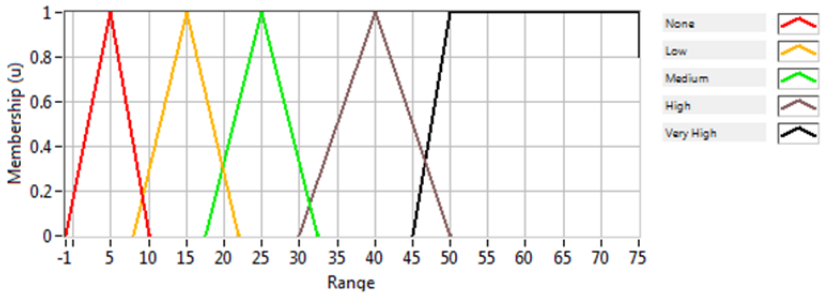

(b)

Figure 12: Fuzzy Logic Input Rule Set (a) Temperature and (b) Wind Speed

Table 2: Fuzzy Logic Output Rules

		Wind Speed				
		None	**Low**	**Medium**	**High**	**Very High**
Temperature	**Extremely Cold**	None	None	None	None	None
	Very Cold	Medium	High	Very High	None	None
	Cold	Low	Medium	High	Very High	None
	Cool	Very Low	Medium	High	Very High	None
	Warm	None	Very Low	Low	Low	None
	Hot	None	None	None	None	None

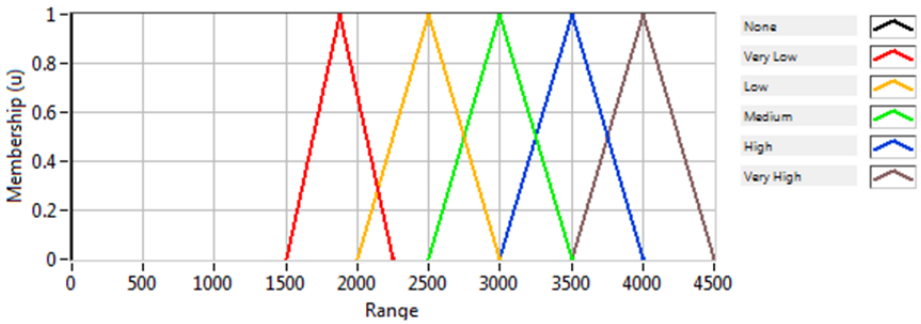

Figure 13: Specific Power (W/m^2) Output Set for Fuzzy Logic Controller

3.5 LABORATORY TESTING OF CONTROL SYSTEM

3.5.1 Variable Wind Speed Tests

To test the implemented fuzzy logic controller, the samples were heated in the simulated freezing wind conditions with the heating power regulated by the controller implemented in LabView. To provide a proof of concept, tests were conducted with no ice on the plate surface to show that the fuzzy logic controller is able to accurately and precisely control the surface temperature of the composite plate. Robustness of the fuzzy logic controller was tested by changing both the temperature and wind parameters of the test and allowing the controller to automatically compensate the supplied CF tape power to maintain the desired surface temperature.

3.5.2 De-icing Feasibility Test

To demonstrate the ability of the proposed self-heating CF tape laminate to perform the actual de-icing function, a feasibility test was undertaken to melt and remove ice from the heated portion of the composite samples. To prepare the samples for the de-icing test, a thin layer of ice was formed on the surface of the sample with 150mL of water directly frozen on to the surface of the composite plate. The nominal thickness of the ice layer was 0.25 in.

To track the de-icing progress, the mass of the frozen ice on the surface of the plate was recorded throughout the de-icing procedure. At the onset of the control action, mass measurements were taken every minute; after 5 minutes, the mass measurements were spaced to every 2 minutes. Measurements were continually taken until the decrease of mass was less than 0.05g per measurement interval.

3.5.3 Dew Point Based Anti-Icing

To further reduce the power consumption of the proposed automated de-icing system in real world applications, the addition of a dew point (DP) comparison to the composite surface temperature was added. As discussed in the literature review section, most icing events are rhime icing events and occur due to high water vapor content in the air surrounding the turbine blade, not by precipitation events, such as rain or snow. Thus, it is reasonable to use the additional information of the DP, the temperature below which water vapor in the air will condense, of the surrounding air as an indicator of the likelihood of rhime ice formation.

An Ohmic Instruments DPSC-35XR dew point sensor and signal conditioning board was used to measure the dew point of the air passing over the composite plate. The sensor element was place at in the wind tunnel just prior to the composite plate platform. The dew point was recorded from the included signal conditioning board and compared to the measured air

temperature in the area surrounding the wind tunnel. To provide additional moisture to the air, a humidifier was used to introduce water vapor into the wind tunnel upstream of the plate. Due to the limitations of the humidifier, the de-icing test was only run in still air. To test the performance of the controllers throughout different icing conditions, the humidifier was turned on and off at the intervals described in Figure 14. The mass of ice accretion was taken every 15 minutes. An updated block diagram of the measurement scheme is presented in Figure 15. A photograph of the test set-up with the dew point sensor is presented in Figure 16.

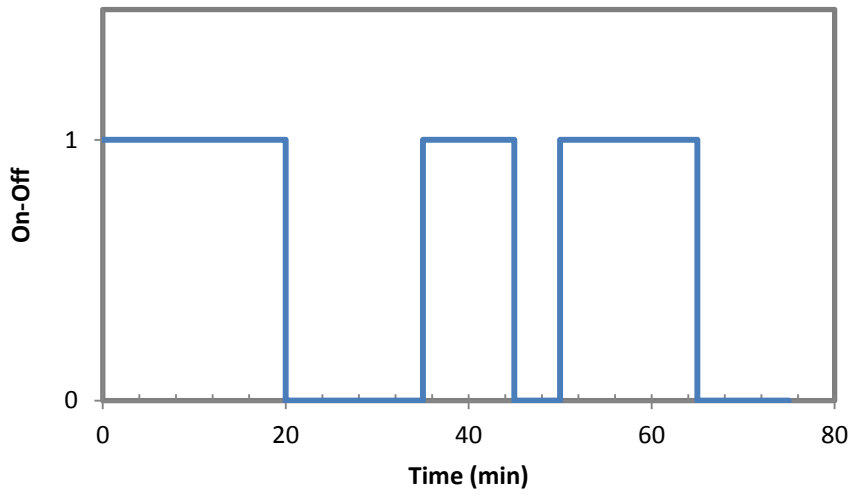

Figure 14: Intervals of humidifier action during anti-icing test

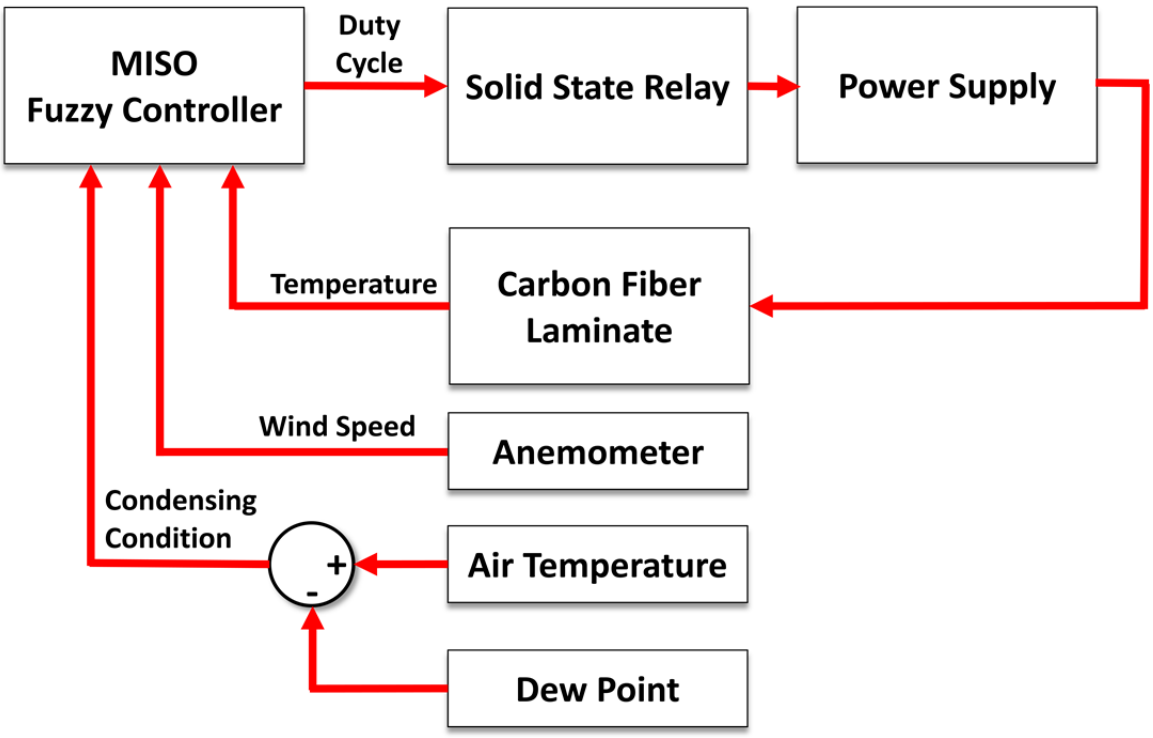

Figure 15: Block diagram of dew point enhanced anti-icing control

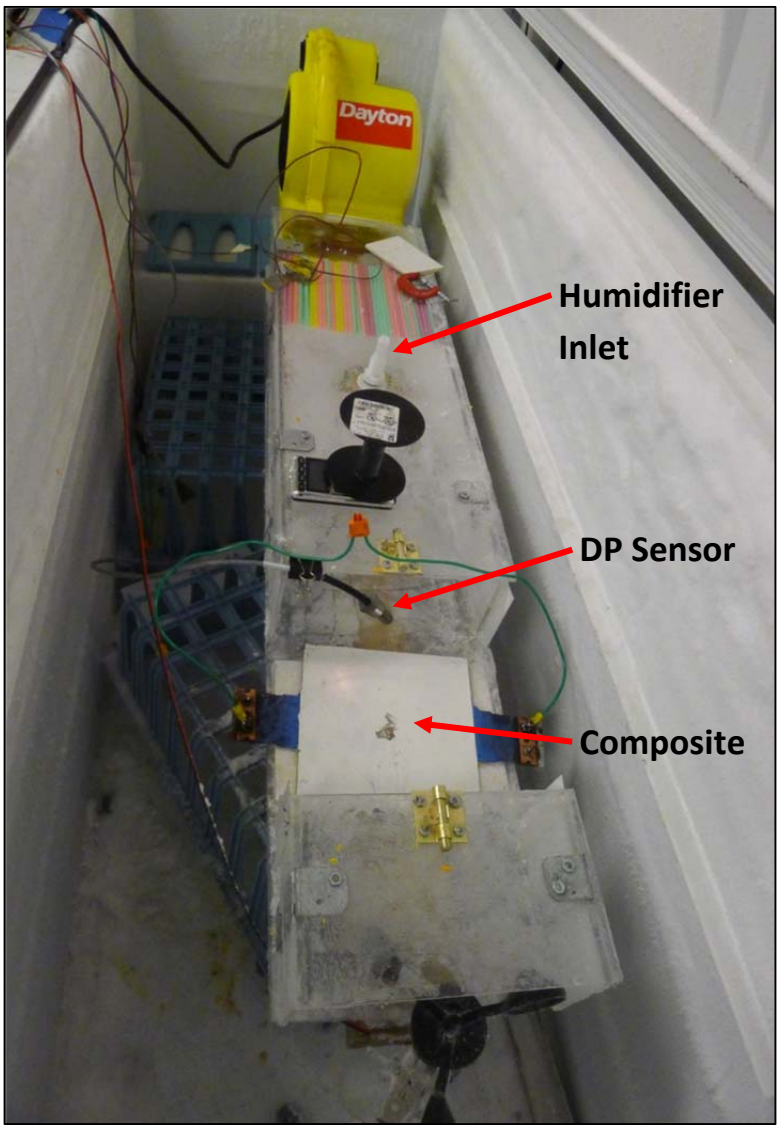

Figure 16: Photograph of test set-up with dew point sensor

The dew point measurement was incorporated into the control scheme by taking the difference between the air temperature and the measured dew point temperature, or

$$T_{Diff} = T_{Air} - T_{Dew\ Point}. \quad (1)$$

If the difference was positive, then the dew point was below the air temperature and no icing event was expected, as no water will condense out of the air; if the value was negative, then the air temperature was below the dew point and it is expected that water vapor will condense out of

the air, small water droplets will form on the composite surface, and the condensed water will quickly freeze onto the composite in the form of rhime ice.

To quantify the effectiveness of the anti-icing strategy, the mass of ice accretion during the icing event was recorded. Though hygroscopic effects are quite common in composites due to the polymer matrix' ability to absorb water, this water absorption is diffusion driven and due to both the low temperatures and low water concentration in this experiment, the weight of absorbed water is negligible.

A comparison of the relative anti-icing effectiveness of the CF heated laminate composite was conducted with the following control schemes (detailed description of the DP enhanced on-off and fuzzy controllers will follow):

- No heating
- On-off control (surface temperature only)
- DP enhanced on-off
- DP enhanced fuzzy

The DP enhanced on-off control function exactly like the on-off controller described previously, with the added condition that heating will be provided ONLY if the DP also rises above the ambient air temperature. The DP enhanced fuzzy controller uses the benefits of fuzzy logic rules to provide even more complexity – given that possible icing conditions are predicted, the fuzzy logic controller can act more proactively than the DP enhanced on-off control and provide an appropriate level of pre-heating to the plate to further reduce power usage, as it is often more power efficient to maintain a temperature than to repeatedly heat up to that temperature. Adding the paramenter T_{Diff} to the fuzzy controller, the fuzzy logic rules were updated as shown in Figure 17.

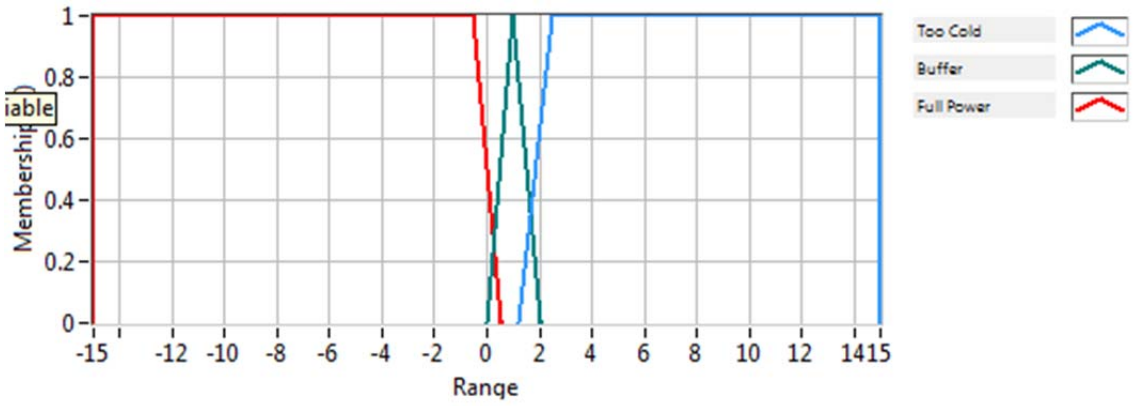

Figure 17: DP enhanced fuzzy control rules

Using the DP difference classification presented in Figure 17, the output rules were updated with three simple changes:

- IF the DP difference is in the "Full Power" range (the DP is higher than the air temperature), then use the output rules in Table 2 based on the surface temperature and wind speed.
- IF the DP difference is in the "Buffer" range and the temperature is in the "Cool" range, as described previously in Figure 12, the power output is one level below the output specified in Table 2 for the same surface temperature and wind speed to provide pre-heating for future icing conditions. For example, if the power output in Table 2 would be "Very High," the output is downgraded to "High."
- IF the DP difference is the "Too Cold" range, the DP falls below the air temperature and no water is expected to condense. The controller applies no power for heating.

3.5.4 RESULTS

The results of the surface temperature controlled, constant wind heating tests for the fuzzy set calibration are given in Figure 18 and the summary of the required power to maintain

the set point for different wind speed is given in Table 3. In the minimum specific power required to maintain our 4C set point, it can be seen that with the exception of the no wind condition, the remaining points follow a relatively linear relationship between the required specific power and the wind speed, consistent with the large effects of convection on the cooling.

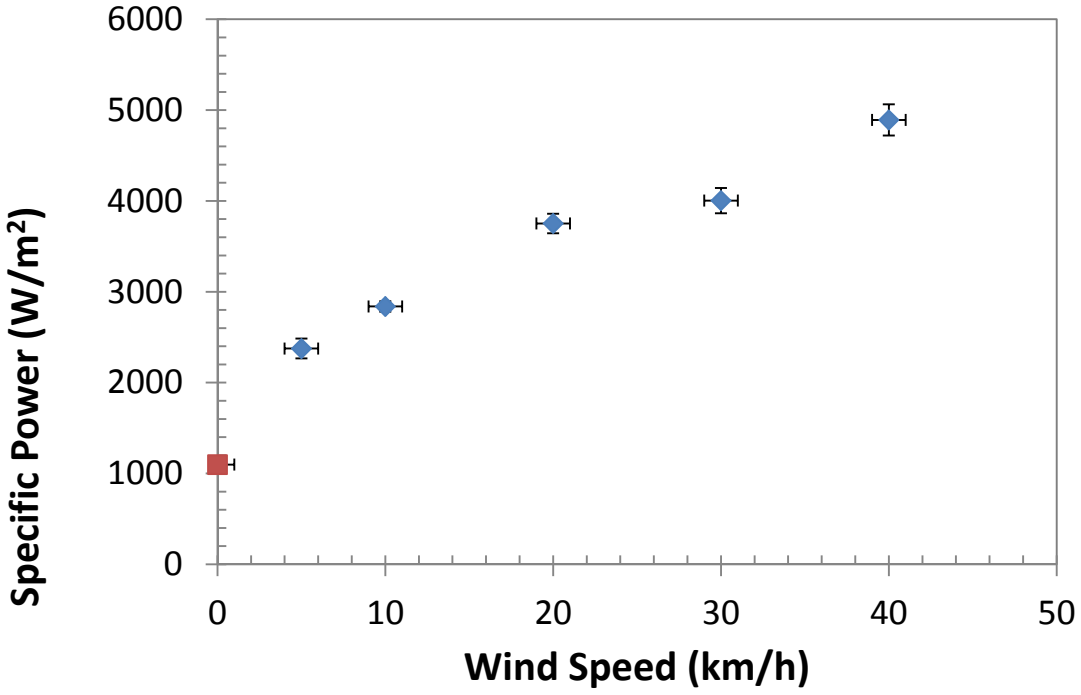

Figure 18: Minimum specific power vs. wind speed - 4°C set point

The summary of the minimum specific power requirements in Table 3 were used as a baseline for the design of the fuzzy logic controller. The relative linearity between points with wind speeds leads us to believe that interpolation of operating conditions using center averaged defuzzification techniques can accurately provide power at wind speeds outside of our calibration set.

Table 3: Minimum Specific Power and Duty Cycle for Different Wind Speeds - 4°C Set Point

Wind Speed (km/h)	Specific Power at +4°C (W/m^2)	Duty Cycle % (P_{Max} = 5400 W/m^2)
0	**1097.94**	**24**
5	**2375.66**	**44**
10	**2838.34**	**52**
20	**3752.27**	**69**
30	**4003.54**	**74**
40	**4891.51**	**90**

To test for robustness, the wind speed was varied and the fuzzy logic controller used to automatically compensate the power sent to the CF tape. The recorded temperatures for the designed fuzzy logic controller are compared to the performance of an on/off controller for the same time-varying wind speed course for comparison in Figure 19. First, the wind speed was increased in increments of 10 km/hour and held for 5 minutes before the next wind speed increment. When the maximum wind speed of 40 km/hour was reached, the wind speed was gradually stepped down to 35, 25, 15, and 5 km/hour at 5 minute intervals to test the ability of the fuzzy logic controller to interpolate between the data set used for its design.

The comparison of the fuzzy logic controller performance against the on/off controller is presented in Figure 19. It can be seen that as the wind speed was increased, the performance of the two controllers to maintain the temperature at 4°C was very similar and only has a few point of significant difference. First, at the onset of the test, the on-off controller experienced an initial overshoot of the surface temperature. Due to the gradual tapering of power as the set point is reached in the design of the fuzzy controller, no such overshoot was seen in the fuzzy logic controller. Next, at the first increase of wind speed from 0 km/h to 10 km/h, both control strategies experienced an initial dip in temperature from which they quickly recovered. The fuzzy logic controller was slightly slower to recover due to its reduced power rate near the set point. It should be noted that despite the short dip, neither controller allowed the surface

temperature to drop below freezing. Finally, at the last wind speed change from 5 km/hour to 0 km/hr, both controllers experienced a small overshoot in the surface temperature, but the maximum error in the fuzzy logic controller, a difference on +1.3°C, was much less than that of the on-off controller, a difference of 3.6°C. It should be noted that both of these significant adjustments in surface temperature occur when transitioning to or from no wind speed, consistent with the discontinuity seen in the power vs. wind speed plot in Figure 18.

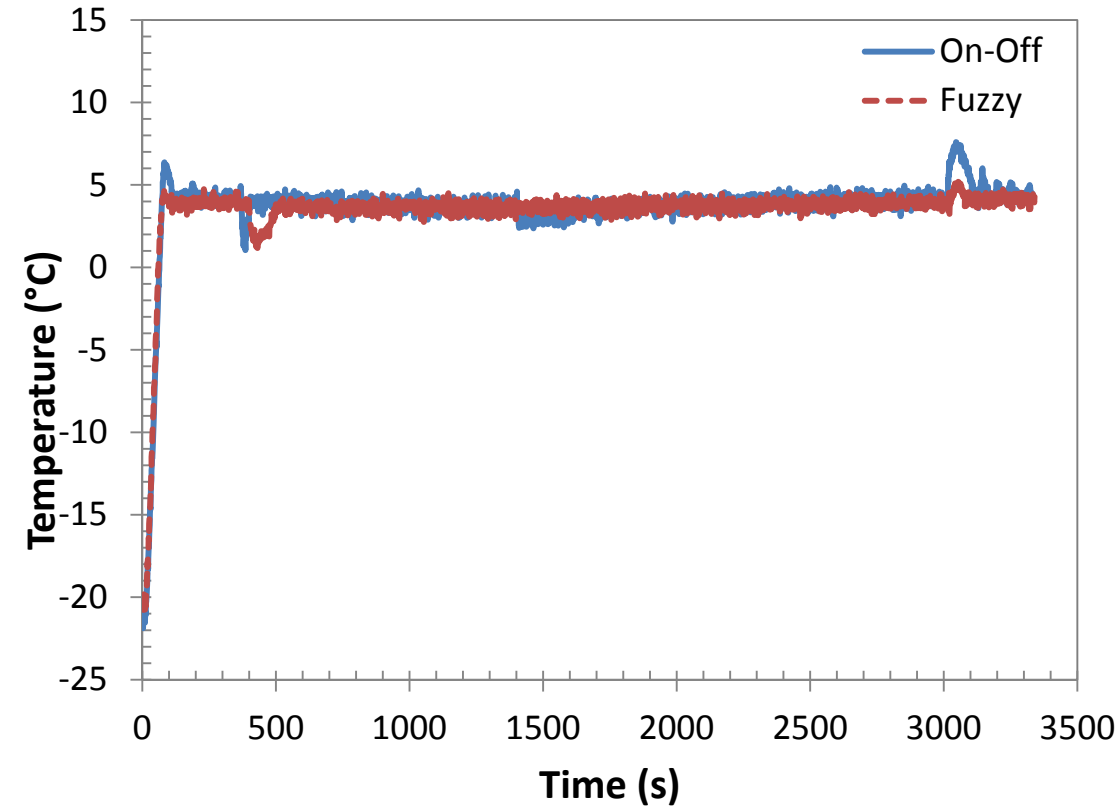

(a)

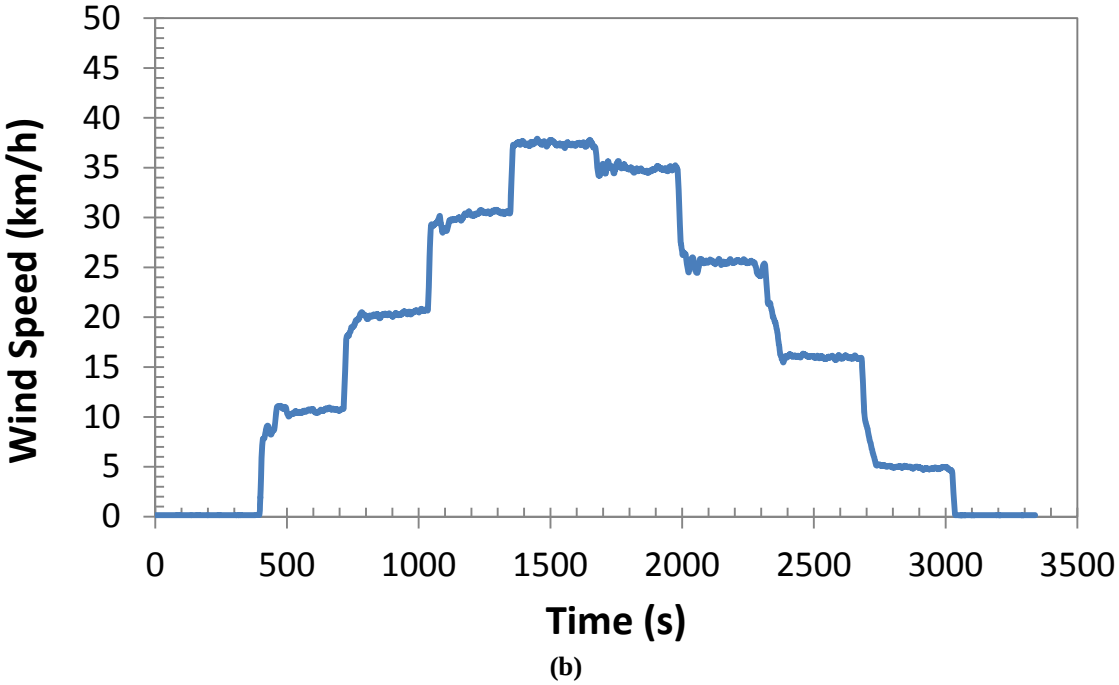

(b)

Figure 19: Increasing Wind Speed Test (a) CF Tape Surface Temperature and (b) Wind Speed

To compare the efficiency of the two controllers, the consumed energy during the different wind speed tests used to heat and maintain the surface temperature of the plate was calculated. The use of energy with time is presented in Figure 20 and the total energy usage is tabulated in Table 4. The term "energy unit" refers to the a normalized unit of energy equal to full power heating over one second; thus, the fuzzy logic control's usage of duty cycle results in a fraction of an energy unit during one cycle of carrying wave. The total energy can easily be calculated by multiplying the energy used in one second of heating at full power. From the plot of energy vs. time, it can be seen that throughout the variable wind speed test the fuzzy logic controller is more energy efficient while maintaining the same surface conditions as the on-off controller. At the end of the test, the total energy units consumed in the heating process were calculated and it was found that the fuzzy logic controller had a total energy savings of 13.7% as compared to the on-off controller, a significant savings which, in the proposed wind turbine blade application, would not only result in an energy cost savings, but also an increase in production as the saved electrical energy can be sold on the electricity market.

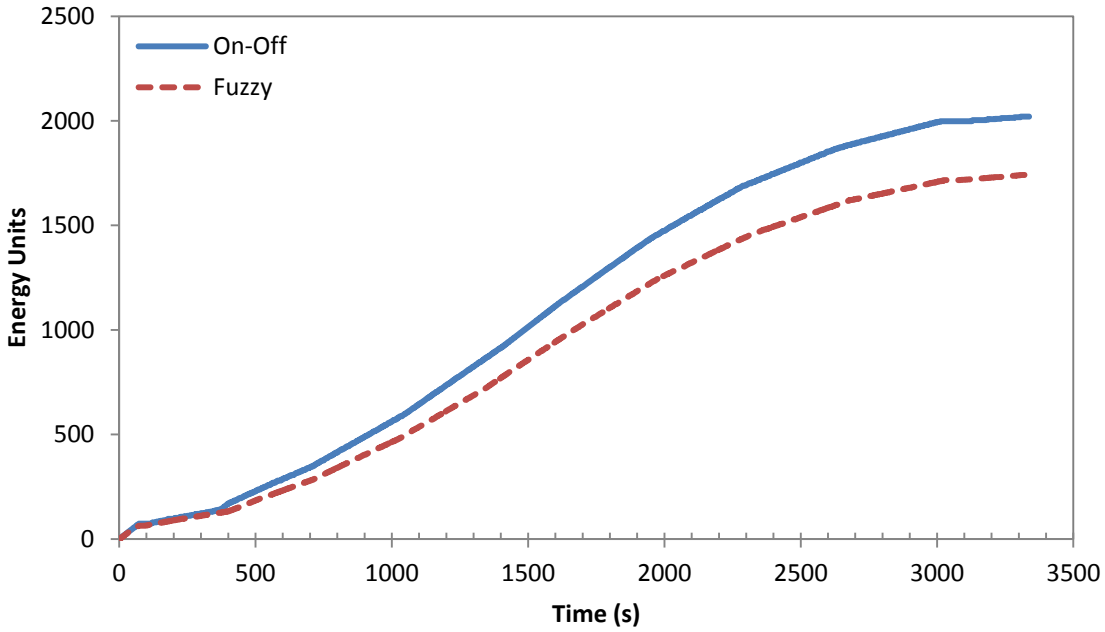

Figure 20: Energy usage vs. time of variable wind speed temperature control test

Table 4: Energy Usage for On/Off and Fuzzy Controllers

	Control Type	*Energy Usage (Energy Units)*	*Energy Saving*
Varying Wind Speed	ON-OFF	2020	-
	Fuzzy	1743	13.7%

In addition to verifying the controller action and power usage for pure surface temperature control, the proposed heated CF laminate system was tested for its actual de-icing capacity by measuring the mass of melted ice for the on-off and developed fuzzy power control strategies. The mass of the melted ice over time for the on-off and fuzzy power controlled plates is given in Figure 21. It can be seen that at the onset of heating (0-6 minutes), the on-off controller has a slightly higher rate of melting since it provides full power until the set point is reached, where as the fuzzy controller begins to taper the delivered power as we reach the set point to avoid overshoot. After the set point is reached, the ice temperature is not necessarily the same as the set point and the ice still needs to gain enough heat to overcome the phase change barrier. Between the 5-7 minute mark, the ice finally gain enough heat to begin the phase change from solid to liquid and a relatively large amount of water melts quickly. It is after this initial jump in melted ice mass that we begin to see a significant difference in the controller performance. After the passing this threshold, the fuzzy controller has a higher rate of ice melting, with the final mass of melted ice using the fuzzy controller exceeding that of the on-off controller by 2.37g, or 34% of the final mass of melted ice using the fuzzy controller.

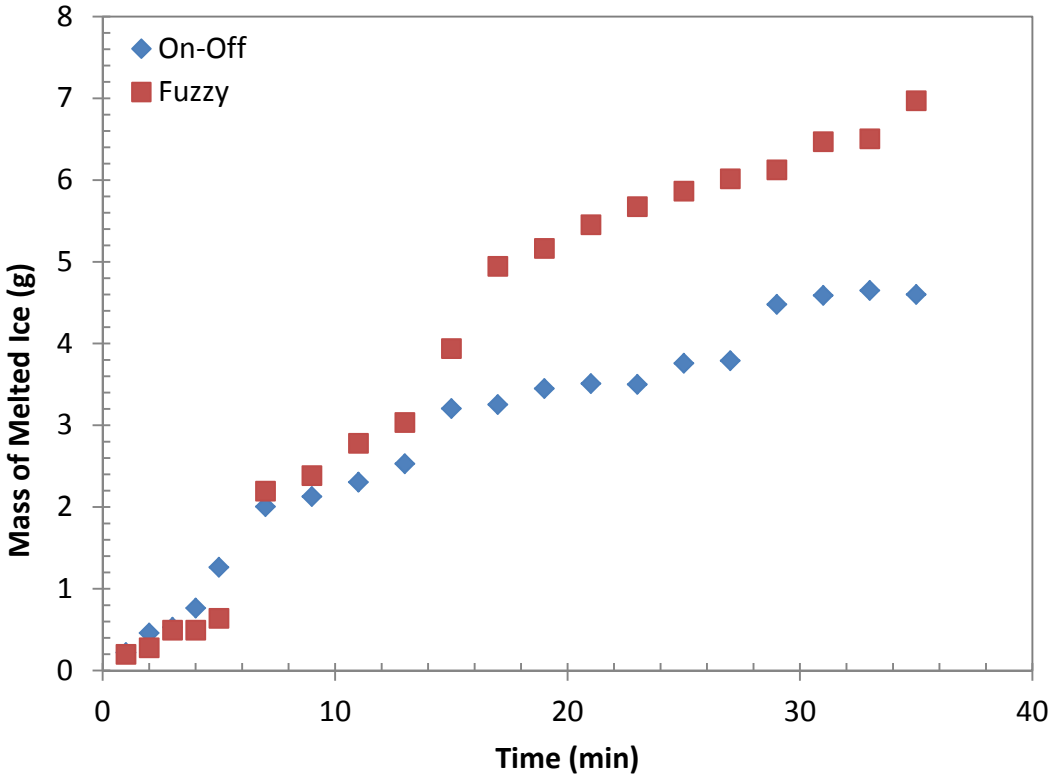

Figure 21: Mass of melted ice

To understand why the fuzzy controller is able to melt so much more ice although the maintained surface temperature at the thermocouple point are the same, it is useful to investigate thermal images of the plates during the de-icing test, presented in Figure 22. It can be seen that though our previous results indicate that the heating is relatively even in the footprint of the CF tape, the on-off controller results in a slightly narrower heated region, over which the temperature is homogeneous. It is believed that since the on-off controller only provides full power over the entire sampling period, the chattering associated with the on-off controller results in relatively long periods with no heating when the surface temperature is even only fractions of a degree above the set point. To illustrate this, the control action during the de-icing tests are shown in for the on-off and fuzzy controller. Thus, though the center of the CF strip footprint meets the set point requirements, the edges cool during the overshoot periods. However, the fuzzy logic control directly controls the duty cycle of the power supply, providing more regular pulses of heating to

the CF element. Thus, heat is delivered more regularly to CF element, constantly reheating the entire footprint and overcoming more heat loss through the CF tape edges.

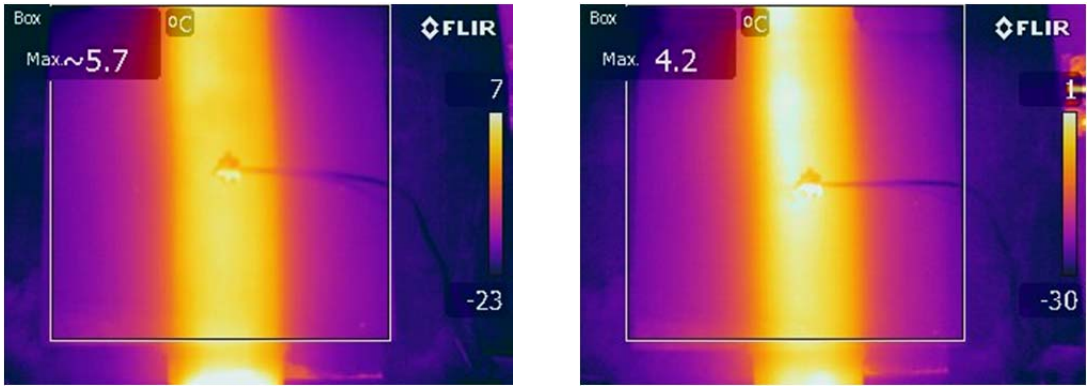

(a) **(b)**

Figure 22: Thermal image comparison of heated area for (a) on-off and (b) fuzzy controllers

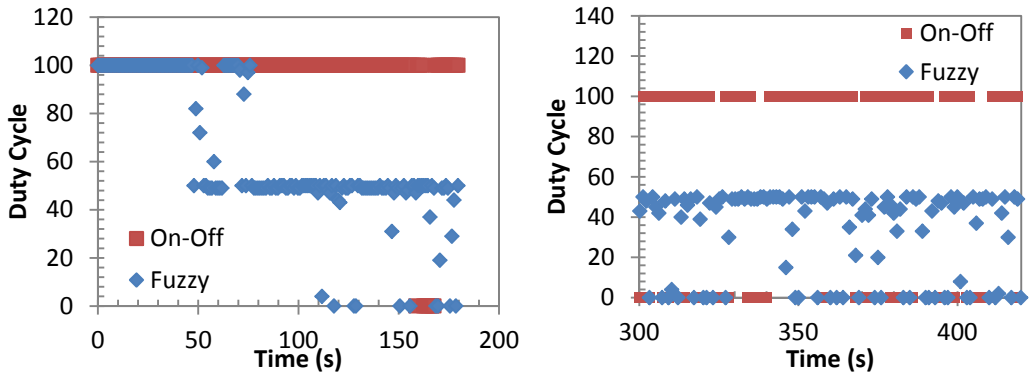

(a) **(b)**

Figure 23: Control action during de-icing test for (a) first 3 minutes and (b) 1 minute of setpoint

A comparison of the energy consumption during the de-icing test also shows that the fuzzy logic controller is more energy efficient that the on-off controller in performing the same task. The energy consumption over time presented in Figure 24 is presented in terms of energy units for simplicity; one energy unit is equal to the consumed energy of the plate over one second of heating at full power. Thus, with an applied voltage of 8.65V over the electrodes and a current of 5.6A, a single energy unit is equal to 48.44J (48.44W over 1 second). As can be seen, after the initial period of heating at which both controllers provide full power to the CF element, the fuzzy

logic controller consistently is more power efficient throughout the duration of the de-icing test once the fuzzy logic controller begins to taper the power as the surface temperature approaches the set point. There is a slight mismatch in time due to the time taken to weigh the samples; however, comparing the energy usage at the end of the fuzzy logic controller to the corresponding time in the on-off test indicates a 32% energy savings of the fuzzy logic as compared to the on-off controller. Additionally, we should bear in mind that for the same time, the fuzzy logic controller was also able to remove more ice from the sample surface, indicating that the fuzzy logic controller boosts both power efficiency and performance of the proposed CF tape based self-heated laminate system.

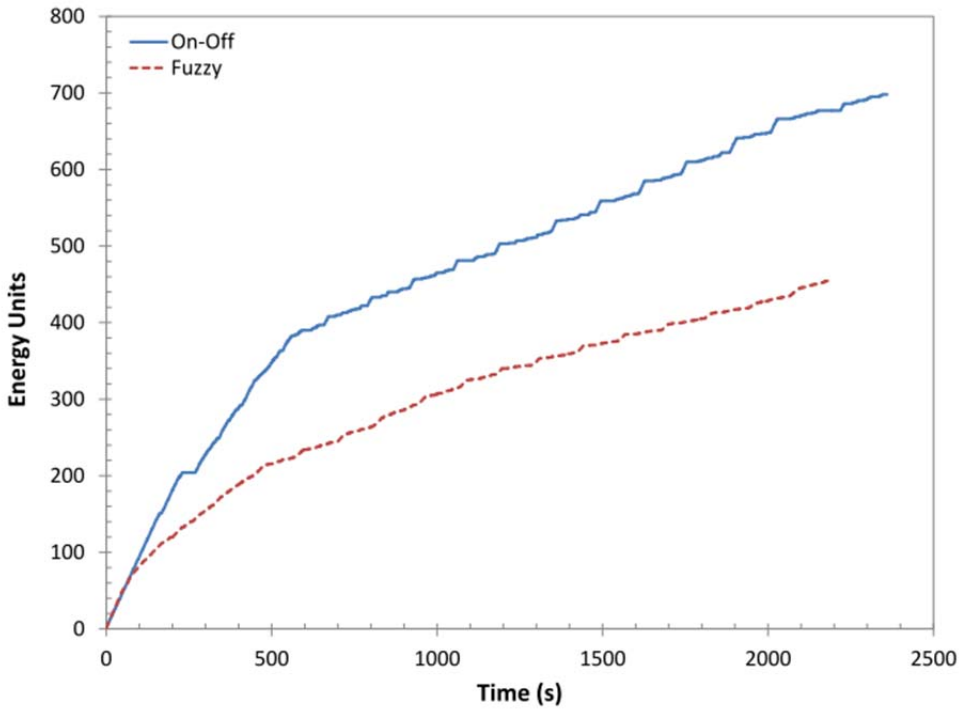

Figure 24: Energy vs. Time during de-icing

The anti-icing performance of the controllers was also evaluated to investigate the ability of the CF laminate system to prevent ice formation on the plate surface due to water vapor condensation. A preliminary investigation of the surfaces of the plates after the icing events, given in Figure 25, shows that the CF tape element is effective in ice formation prevention. In

Figure 25a, the plate with no heating after the icing event is evenly covered in a layer of soft ice crystals. Figure 25b shows the plate after the icing event, during which the on-off power control scheme was utilized; it can be easily seen that in the CF footprint area, there is little ice formation despite the soft crystal ice formation in the surrounding, unheated areas.

Though visual inspection provides a qualitative confirmation of the anti-icing abilities of the CF laminate system, quantification of the anti-icing function of the controller system is provided by measurement of the mass of ice accretion, presented in Figure 26. In Figure 26, the horizontal axis is time, the primary axis (left) is the mass of the ice accretion, and the secondary axis (right) is a binary value (1 = on, 0 = off) to indicate whether the humidifier was turned on or off during that time duration. The mass data supports the anti-icing abilities of the CF laminate system; with the anti-icing heating of the CF plate, the mass of ice accretion was reduced by 25%, 20%, and 33% for the on-off, on-off DP, and fuzzy DP power controllers, respectively.

Furthermore, subtle differences in the controller anti-icing performance can be seen. It should be noted that while the ice accretion rates are comparable between the on-off and the DP enhanced on-off controller, there are only two points at which the mass of ice is higher in the DP enhanced controller than the conventional on-off controller – at 30 minutes and at 75 minutes. Both of these instances correspond to icing events in which the water vapor content was initially high (humidifier on) and gradually dropped below the dew point (humidifier off). After these icing events, it was noted that there were small areas of hard ice formation within the CF footprint on the DP enhanced on-off controlled sample, consistent with the freezing of liquid water. It is believed that as the DP dropped below the air temperature and the controller turned off, small uncertainties in the temperature and DP measurements (each with an uncertainty of ±1°C) resulted in vapor condensation onto the plate surface after the controller was turned off, but before the plate surface temperature dropped below freezing. As the plate continued to cool

below freezing, the liquid water froze, resulting in small areas of ice accretion. A summary of the reduction in ice accretion mass is presented in Table 5.

Table 5: Summary of Anti-Icing Test with Differnt Power Control Strategies

	Mass Accreted Ice (g)	% Ice Reduction	Power Units	% Power Reduction
None	7.35	-	-	-
On-Off	5.48	25%	758.00	-
On-Off DP	5.86	20%	495.00	35%
Fuzzy	4.55	17%	606.91	-20%
Fuzzy DP	4.77	35%	547.53	28%

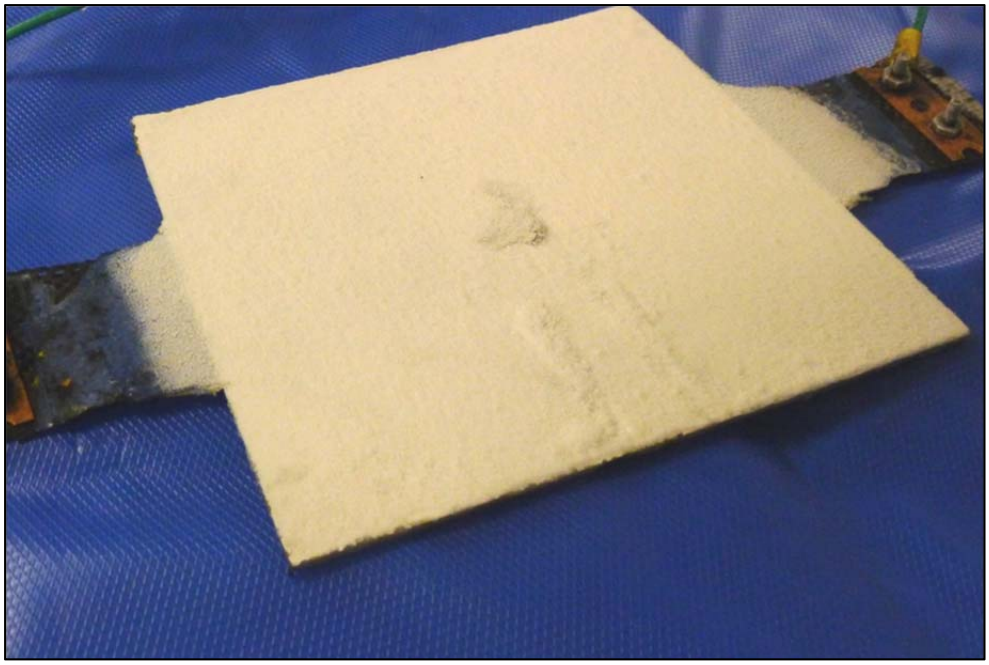

(a)

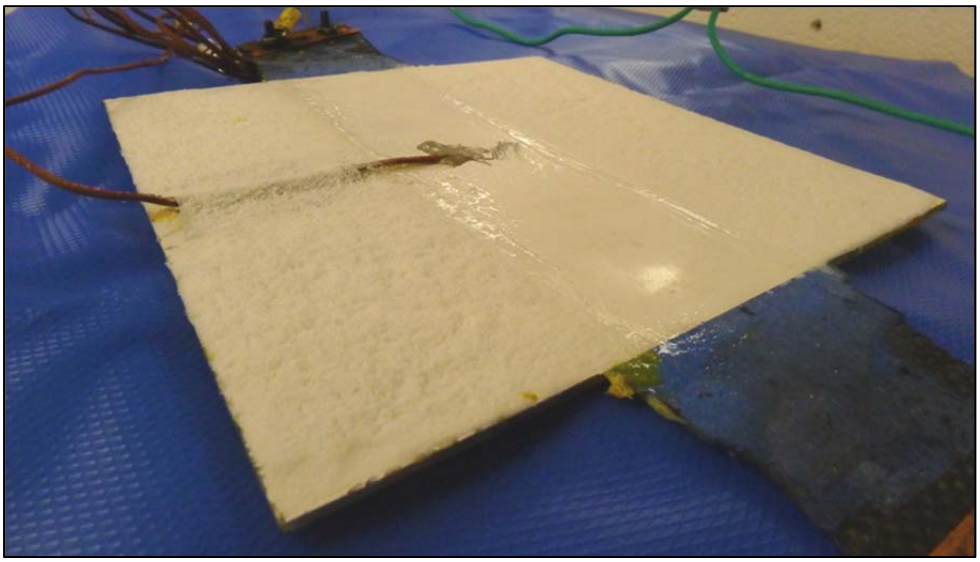

(b)

Figure 25: Photo of sample after anti-icing test with (a) no heating, (b) on-off control

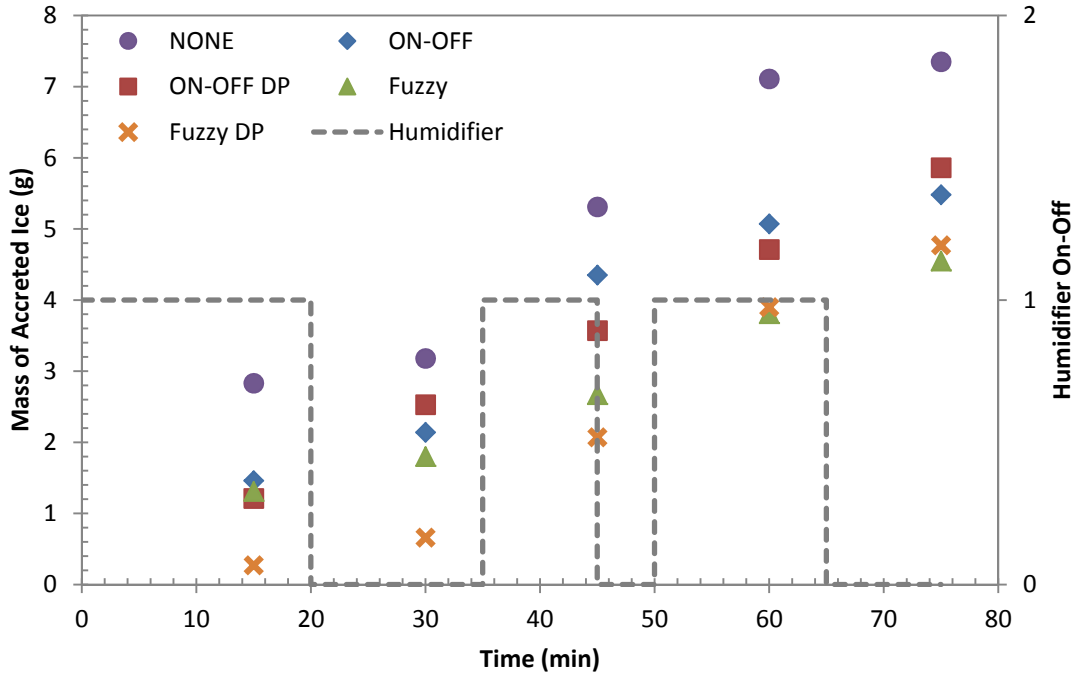

Figure 26: Mass of accreted ice

To further justify the use of the more complicated DP enhanced fuzzy logic controller, a comparison of the power used during the anti-icing tests is presented in Figure 27. The summary of the power usage is given above in Table 5. As expected, the on-off controller was the least power efficient, with the original fuzzy logic based controller approximately 19% more power efficient over the anti-icing duration. Additionally, both DP based power controllers offered significant additional power savings. As compared to the on-off controller, the on-off DP and fuzzy DP controllers each had a power savings of 35% and 38%, respectively. Though the on-off DP showed the largest power savings, it should be remembered that the on-off controllers had slightly more ice accretion compared to the tested fuzzy logic controllers. Thus, in practical applications, the decision to balance power efficiency and effectiveness must be made. With this balance in mind, the fuzzy logic DP based controller provides a good balance between power usage and performance, reducing power usage by taking DP and condensation conditions into

consideration, while providing a mild level of preheating to prevent the freezing of melted ice back on to the surface of the blade.

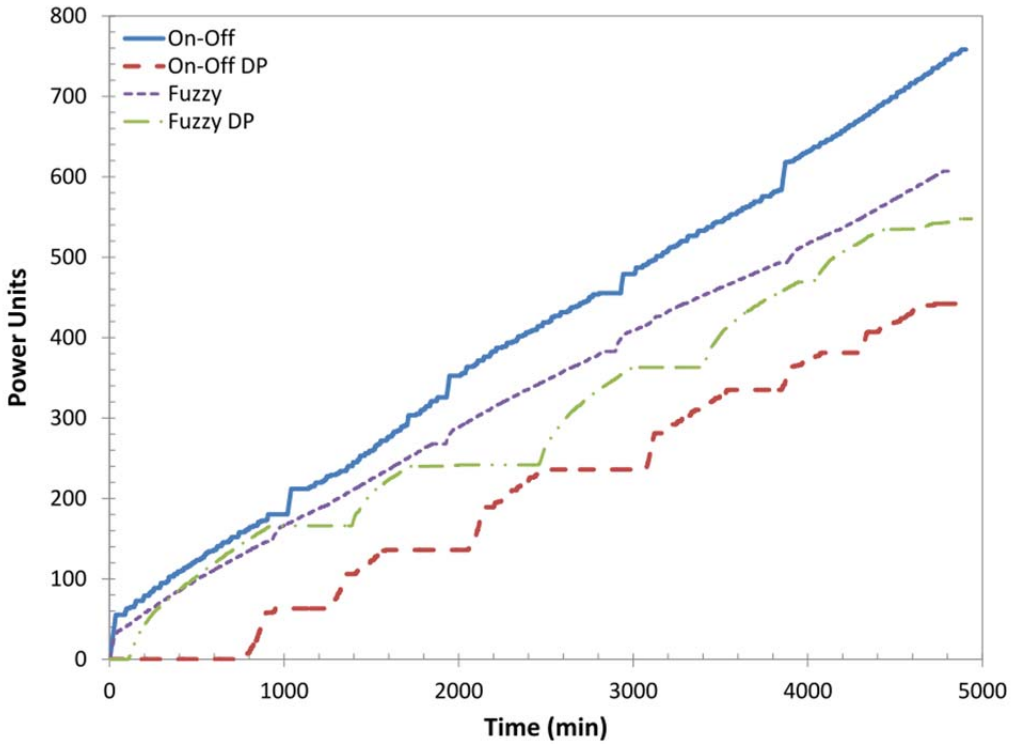

Figure 27: Energy vs. time during anti-icing

3.6 FIELD TESTING OF CONTROL SYSTEM

3.6.1 Fabrication of Small Scale Wind Turbine Blades with CF Laminate Based Heating System

To test the developed self-heating CF laminate composite in the field, a set of three small-scale turbine blades were custom made with the CF heating layer and thermocouple sensors. To form the small-scale turbine blades, the laminate was formed in 1.5m long wind turbine blade molds in two parts – one half for the low pressure side of the blade and one half for the high pressure side of the blade. Following the procedure used to make the lab scale plate samples, 5 ply fiberglass laminates with an embedded CF tape interlayer were fabricated by hand lay-up,

with a schematic of the lay-up and thermocouple positions given in Figure 28. To provide electrical power to the CF tapes, the ends of the CF tape were sandwiched between two thin copper plates, with the connection filled with carbon black conductive grease to reduce contact resistance.

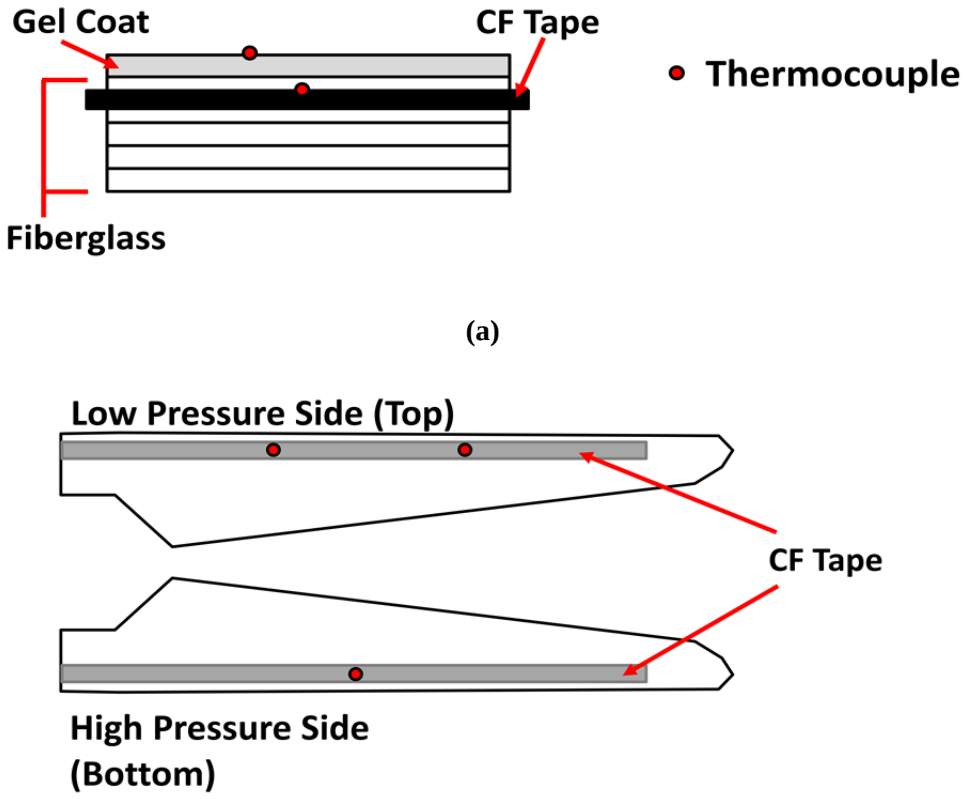

Figure 28: Schematic of wind turbine blade (a) lay-up and (b) sensor placement

After the lay-up was formed and wetted with epoxy, vacuum bagging was used during the 24 hour curing time at room temperature. The cured halves of a single wind turbine blade were then de-molded and bonded together using a high strength, structural bonding epoxy. Finally, to give the blade some weather protection, a clear gel polyester gel coat was applied to the surface and allowed to cure overnight at room temperature. A photo of a completed blade is given in Figure 29.

Figure 29: Photo of completed wind turbine blade with CF heating layer

3.6.2 Field Installation of Test Blades at UAA Campus

Through ongoing research collaboration, a test site at the University of Anchorage Alaska (UAA) campus was granted to erect and test the self de-icing wind turbine blade system during the winter of 2012-2013. The selected site was a secluded pavement site next to the UAA Lake Annex building where a mock-up mounted turbine blade system and data acquisition system could be installed.

For the field installation, three wind turbine blades were fabricated using the methodology described in the preceding section. The blades were fixed in the stall position on a simple hub fixture atop an 8-ft pole on the west side of the annex building. An anemometer was mounted an additional 3 feet above the hub to monitor the local wind speed. To power the CF heating elements, a power junction box was installed using transformers to step down the 120V grid voltage to 24V applied to the CF tapes to comply with UAA safety policies. A schematic of the electrical system is given in Figure 30. A photograph of the installation site is given in Figure 31. To control the power to wind turbine blade CF elements, a National Instruments (NI) 9184 compact data acquisition (DAQ) system was installed outdoors and a laptop located inside the

adjacent annex building was used for data collection. The DAQ was equipped with the NI 9213 16 channel thermocouple module, the NI 9481 4 channel relay module to control the power supply the CF tape elements, and the NI 9201 8 channel analog input module to monitor the wind speed data from the installed anemometer.

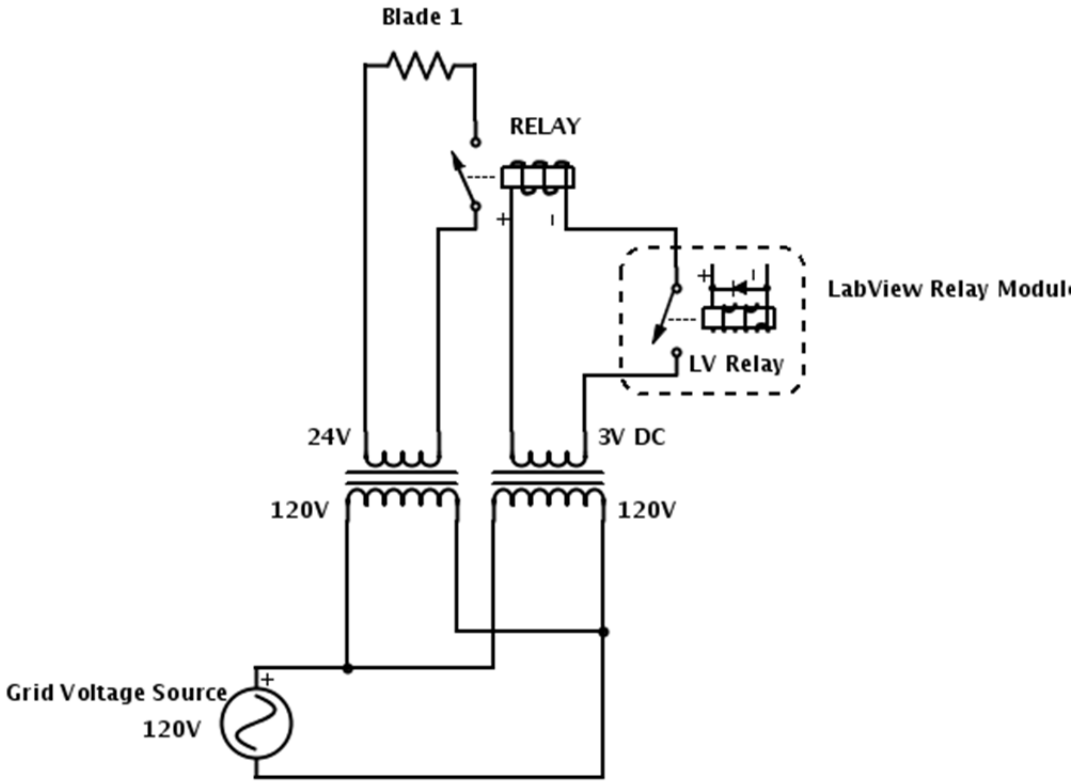

Figure 30: Schematic of electrical system for UAA field installation for single blade

Data collection and system control was performed using a LabView VI run by a computer connected to the DAQ hardware module. A block diagram of the controller is provided in Figure 32. Similar to the lab tests, the controller program included options for using an on-off controller with dead zone or the designed fuzzy logic controller developed through laboratory testing in a preceding section. In addition, the program collected weather forecast information from a Simple Object Access Protocol (SOAP) system proved through the weather.gov public website. Additional comments on the possible functionalities of this weather forecast information is given in Chapter 6

Figure 31: Photo of UAA mock-up wind turbine tower installation

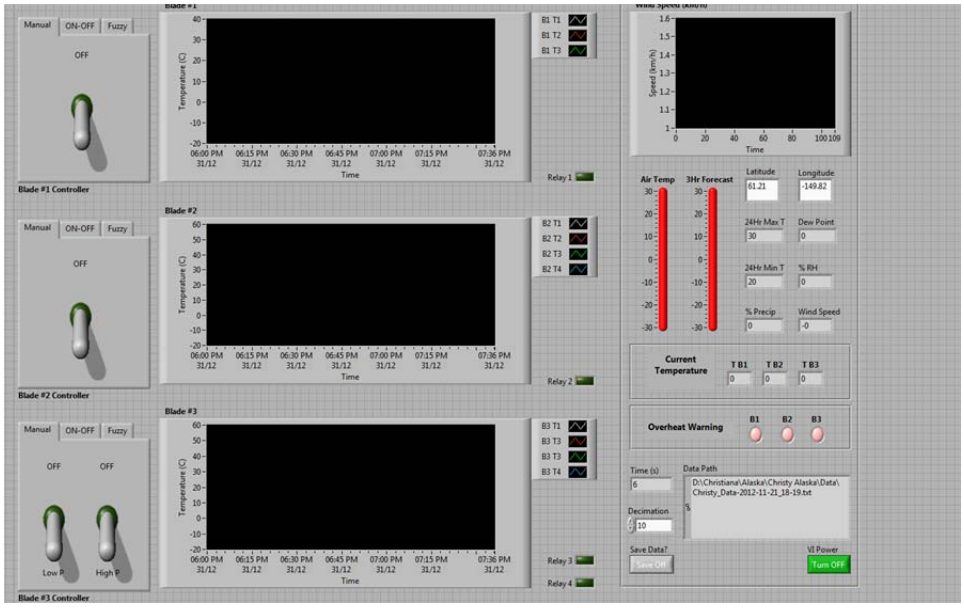

Figure 32: Front panel of UAA field experiment controller

3.6.3 De-icing and Anti-icing Test Procedures

To demonstrate the ability of the developed CF based laminate for de-icing and anti-icing applications, two sets of tests were conducted at the UAA using the erected mock-up wind turbine system.

In the de-icing tests, the dry blades were allowed to cool over night to below -15°C. After the blades reached their target temperature, a high pressure sprayer was used to mist cooled liquid water into the air surrounding the blade. To create a thin layer of ice on the blades' surface, 30second misting events were performed, after which the blades were given a cooling period of 5 minutes to bring the blade surface temperature to below -5°C before the next misting event was performed. For each de-icing test, 10 misting events were performed. A detail photograph of the blade surface with ice is presented in Figure 33. The iced wind turbine blade was then allowed to cool overnight again to below -15°C before the heating controllers were activated and the heating systems powered.

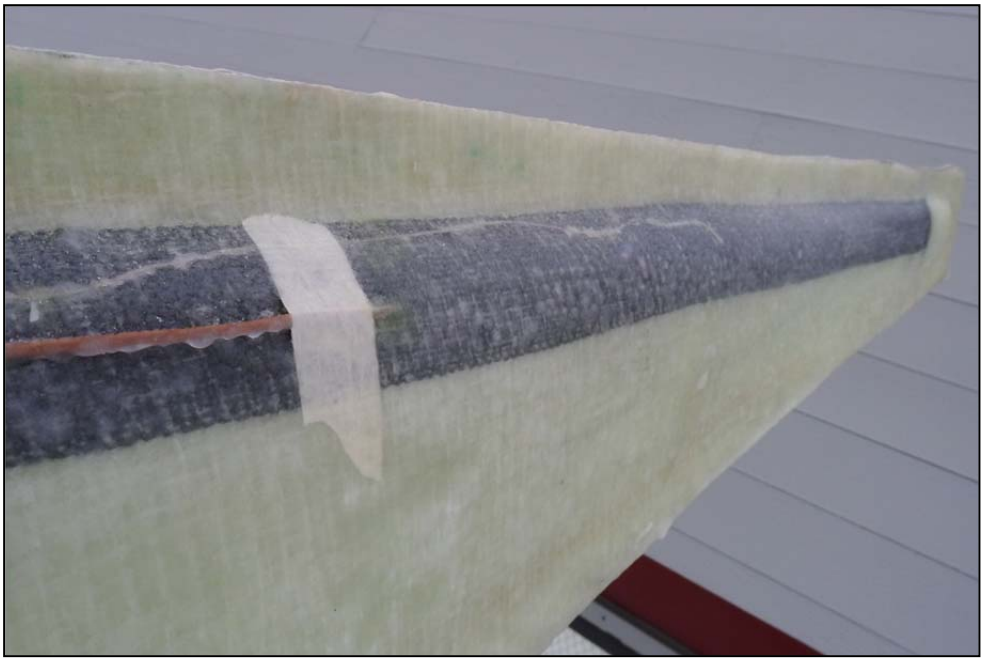

Figure 33: Photograph of installed wind turbine blade after ice formation

In the anti-icing tests, the focus of the testing was the ability of the CF laminate to prevent the formation of ice on the wind turbine blade surface. Similar to the de-icing tests, the blades were first allowed to cool overnight to temperatures below -15°C. Then, the power controller was turned on to allow the blades to heat and reach their target temperature. With the power controller active, the misting events described in the de-icing procedure were performed.

3.6.4 De-icing and Anti-icing Test Results

To demonstrate that the heating is even across the CF footprint within the blade, thermal images of the on-off controlled de-icing test is presented below in Figure 36 throughout the duration of the test. Photographs of the blade surface during the de-icing procedure given in Figure 34 show that within 10 minutes, the ice has begun to melt off of the CF footprint area and that within 30 minutes, the full extent of melting has been reached. Beyond 30 minutes, no additional ice is melted beyond the CF footprint, indicating that the de-icing procedure can be shortened in time considerably while retaining its effectiveness. Visual inspection of the blades showed that, like the lab experiments, the heating was highly localized to the CF footprint and that no significant de-icing was performed outside of the CF boundaries.

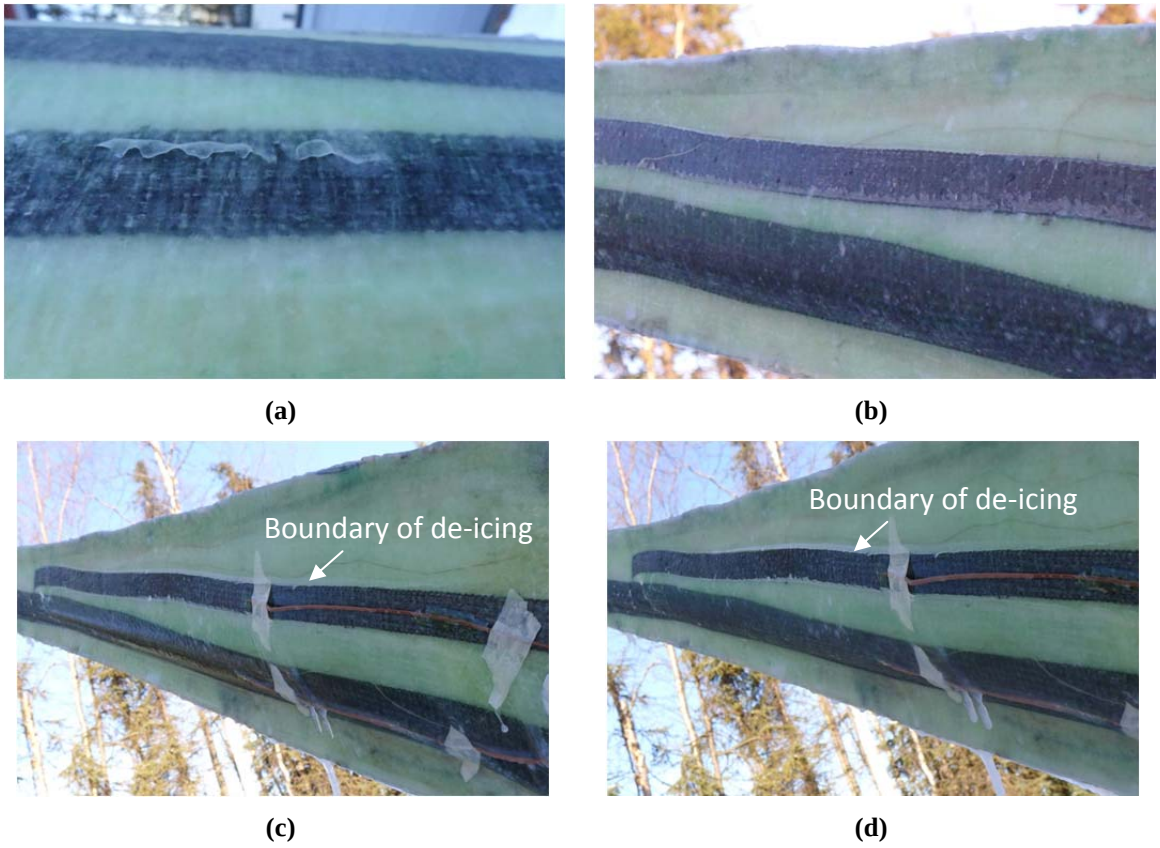

Figure 34: Photographs of blade surface during on-off controlled de-icing procedure after (a) 0 minutes (b) 10 minutes (c) 30 minutes (d) 60 minutes

The temperature history of the two tested blades are given below in Figure 35. It can be seen that the behavior between the two controllers is similar and only some subtle differences distinguish their performance. In the case of both controllers, and initial, high heating rate region is first seen at the onset of the control action as the blade is heated up from the start temperature at full power. Then, the temperature plateaus very near the 0°C threshold as the solid ice begins to undergo phase change to liquid water. When a thin layer of ice on the surface is melted, the temperature again rises to the set point temperature. Beyond the end of the phase change plateu, photographs of the blades, given in Figure 34, and visual inspection indicate that little ice melts after this point. At the set point temperature, the area above the CF tape is either completely deiced or only a thin layer of ice remains with warmed air separating the layer from the blade

surface. In the case of the remnant thin ice layer, it is believed that during dynamic operation of the wind turbine rotor, these light layers can be cast off due to the rotation of the turbine blades.

Thermal images of the installed blades during the de-icing test are presented in to confirm even, localized heating at the CF footprint. The thermal images clearly indicate the position of the CF tape as they are heated using electrical power. The progression of images supports the collected thermocouple data, indicating a fast initial heat up period, followed by a slowing heating rate as the ice melts away, exposing the hot CF to the thermal sensor. Finally, the thermal images confirm that in the operational strips, there are no hot spots at the electrical connections, which could potentially impact structural properties of the epoxy matrix.

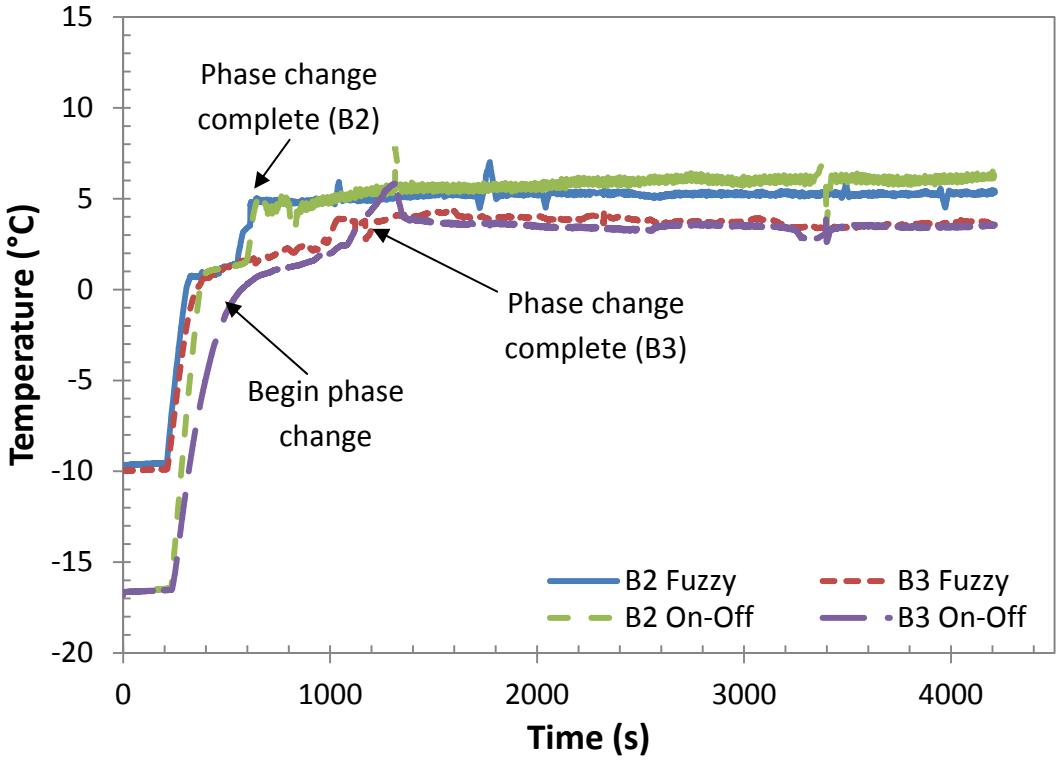

Figure 35: Temperature history of blades during de-icing test

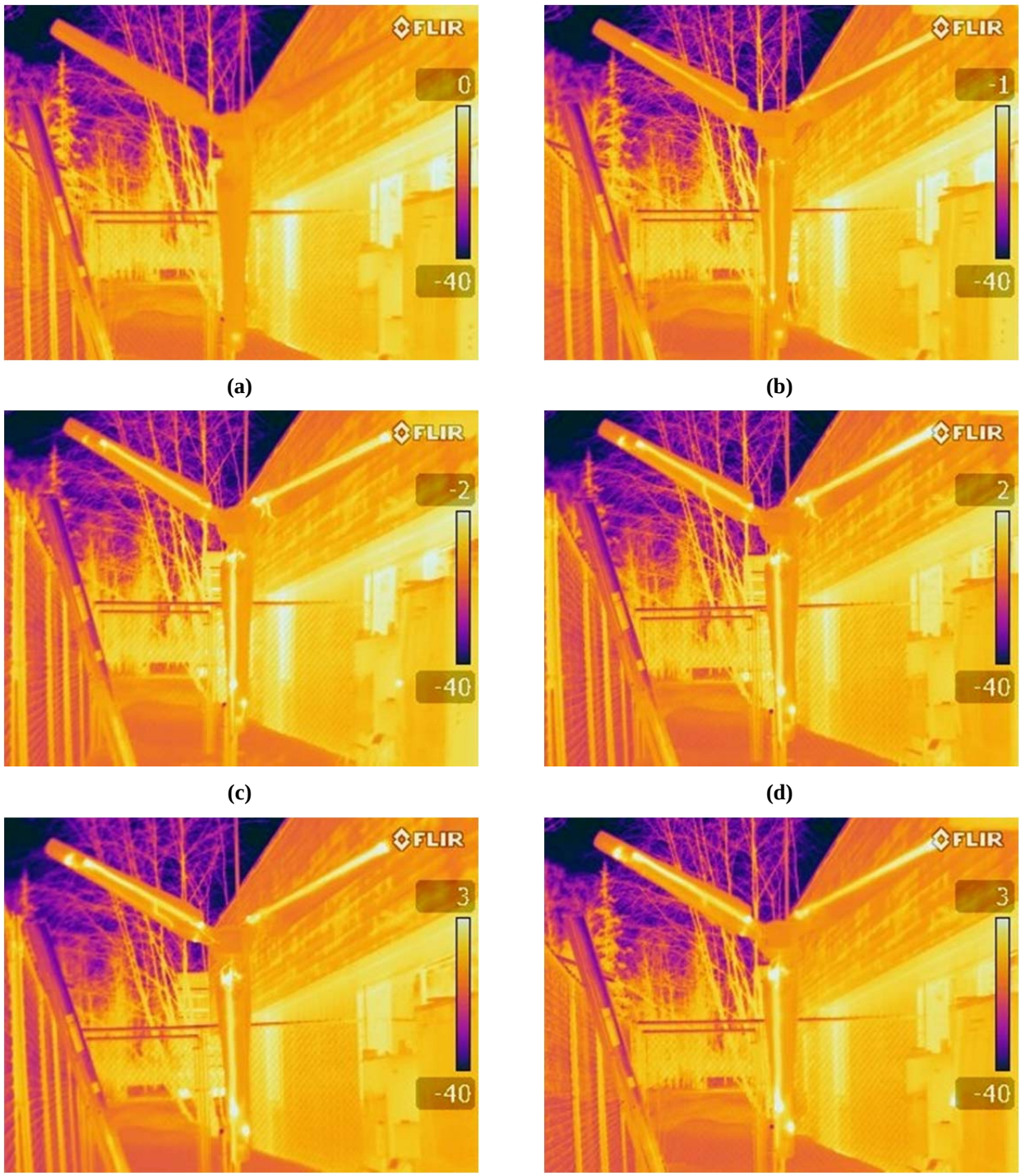

Figure 36: Thermal images of wind turbine during on-off de-icing procedure after (a) 0 minutes (b) one minute (c) 5 minutes (d) 10 minutes (e) 20 minutes (f) 30 minutes

(g) **(h)**

Figure 36: (g) 40 minutes (g) 50 minutes (h) 60 minutes (Temperature in °C) (continued)

The consumed energy of the individual wind turbine blades using the two different temperature controllers was analyzed and is presented in Figure 37. In each of the energy curves, two distinct linear regions are present: Region I corresponds to the initial heat up time and phase change durations of the de-icing process. To overcome the energy barrier to phase change, the controllers operate at full power until the blade surface temperature surpasses the phase change temperature, 0°C. Region II corresponds to the "maintenance" portion of the de-icing process during which the surface temperature is maintained at the set point while a small amount of additional ice is melted, mostly just above the air gap between the surface and the cover layer of ice and at the periphery of the CF tape border. These two regions indicate that it takes less power (energy rate) to maintain the temperature than to provide heating, lending strength to the argument for anti-icing (preventative pre-heating) rather than de-icing.

From the computed energy results, it can be seen that there is variability in the energy efficiency of the fuzzy logic controller as compared to the on-off controller. For blade #3, there is minimal energy savings beyond the phase change point and, in fact, the power rate (slope of line) is higher than that of the on-off controller. This may be due to the positions of the blades – blade #3 was further from the building face and was exposed to more wind. It may be possible

that the wind conditions were different during the two tests. Blade #2 was next to the building face and experienced much less wind. However, in the case of blade #2, the energy savings are significant, with a divergence from the on-off controller beginning at the end of the phase change point. At the end of the test, the energy savings of the fuzzy controller was 23% compared to the on-off controller. Most importantly, it should be noted that the rate of power usage is lower, indicating that the fuzzy controller requires a lower power rate to maintain the set-point temperature.

Anti-icing tests were also performed and the results presented in Figure 39 and Figure 38. From visual inspection of details of the post icing event photograph in Figure 39a, it is seen that the CF pre-heating was effecting in preventing the formation of ice on the targeted areas. The photos show only liquid water, which is easily thrown off during rotor rotation, on the CF heated area. Conversely, at the edges of the CF tape, we can see the formation of ice layers, indicating that the CF tape is able to provide highly target heating. To further emphasize the effectiveness of the CF heating strategy, frozen run-off water on the blade is shown in Figure 39c.

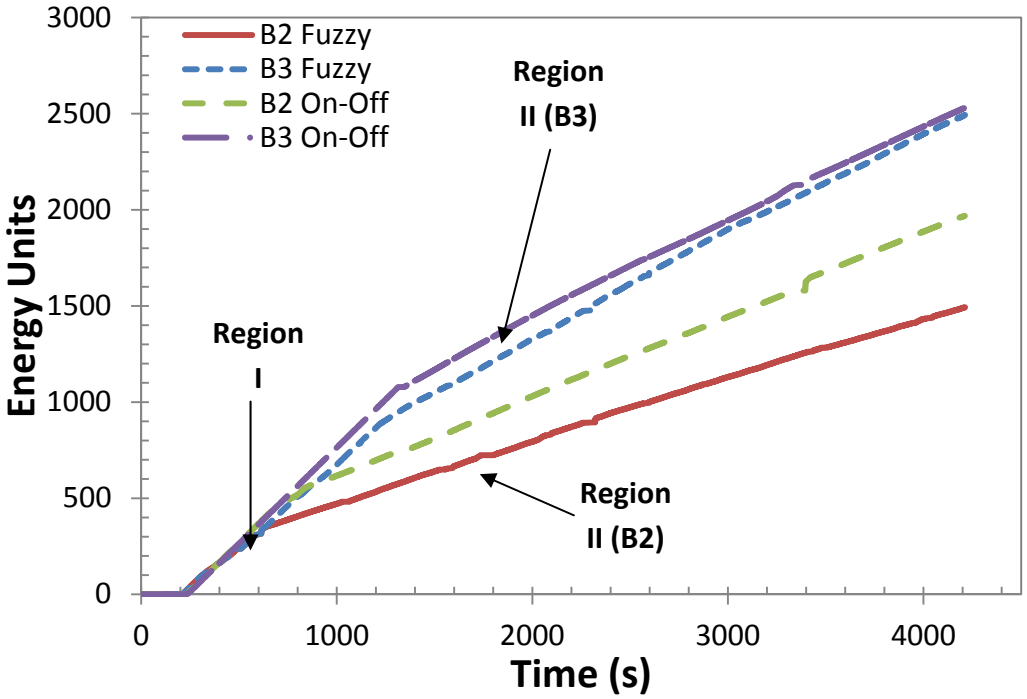

Figure 37: Energy vs. time during on site de-icing test

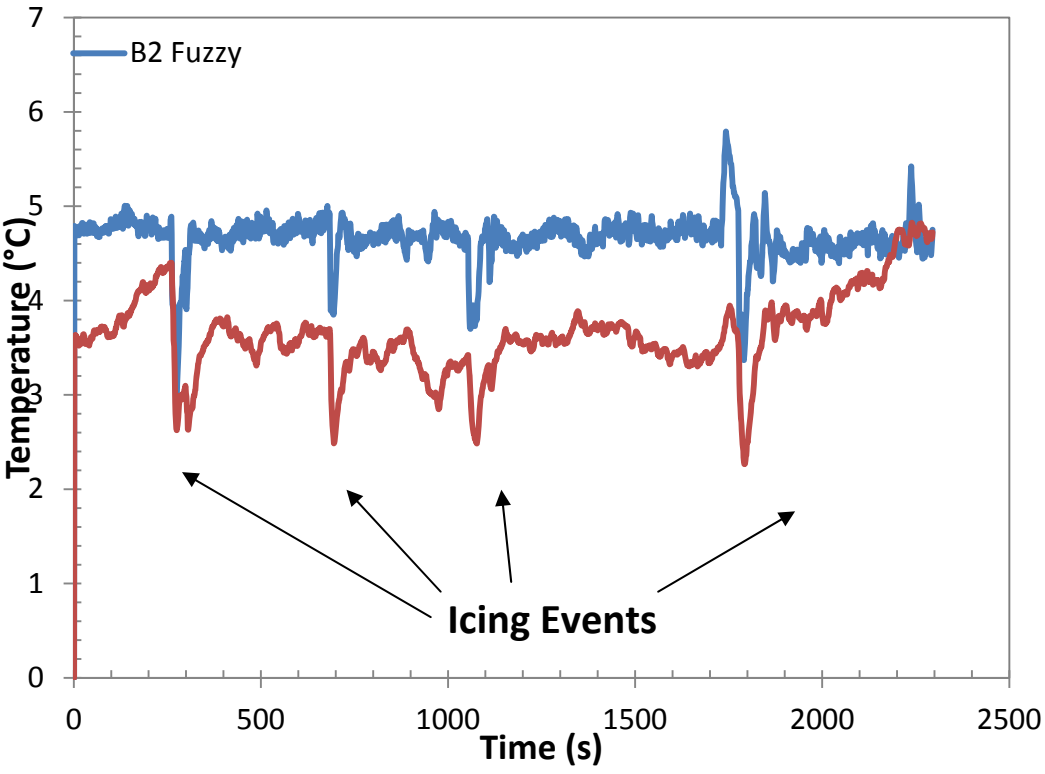

Figure 38: Sample temperature history during anti-icing test

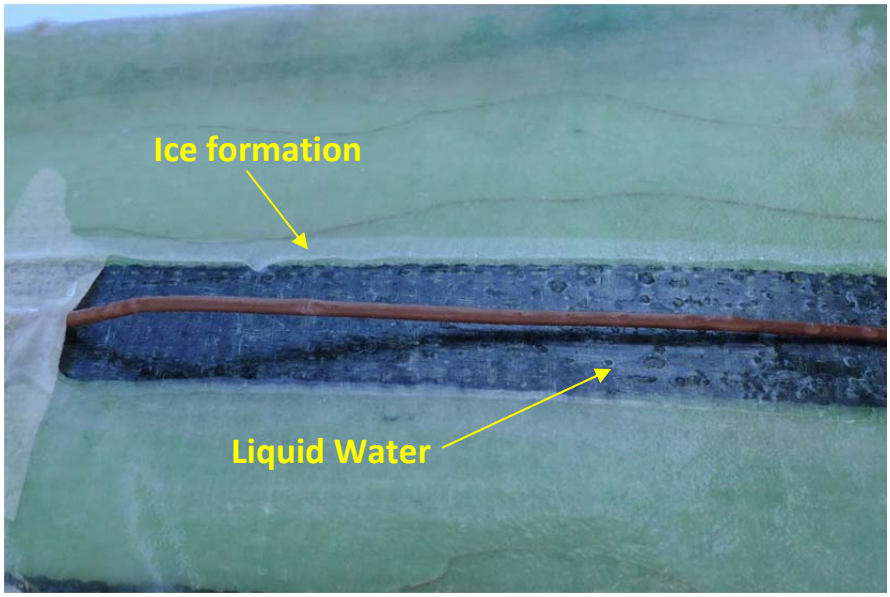

(a)

(b)

Figure 39: Photos of wind turbine blades during anti-icing test – (a) detail of CF tape, (b) detail of blade #2

(c)

Figure 39: (c) frozen run off water (continued)

A sample temperature history of the blades during the de-icing test is given in Figure 38. It can be seen that throughout the test, the CF tape was able to maintain the surface temperature above freezing, despite the presence of freezing water vapor absorbing heat from the blades during misting events. During the misting events, the surface temperature dropped no more than 1.9°C, leaving a significant buffer zone above freezing to prevent freezing in the case of longer icing events.

3.7 DISCUSSION

In this chapter, work toward the development of a CF based self-heating laminate composite for de-icing purposes and a supporting fuzzy logic based surface temperature controller for both de-icing and anti-icing functions was presented. From the feasibility tests

performed, it can be seen that not only is the proposed CF-fiberglass-epoxy laminate system effective in both the de-icing and anti-icing functions, both effectiveness and efficiency can be improved using the proposed fuzzy logic controller which is based on experimentally obtained minimum specific power requirements to maintain a 4°C set point. In laboratory testing, the fuzzy logic based controller out performed a traditional on-off controller in terms of both capacity to melt formed ice off the surface of the CF based laminate and to prevent ice formation on the surface while reducing the power consumption of the CF heating element by as much as 24%. Though the proposed fuzzy logic controller adds additional complexity to the turbine system, particularly the DP enhanced fuzzy logic controller which also requires the installation of a DP sensor, it should be noted that given the same effectiveness in de-icing or anti-icing, reduction in power consumption is a dual benefit – not only is the cost of energy used reduced, but also the available product from a wind turbine is increased, allowing both continuous operation of the turbine during icing conditions and a larger share of the produced electricity to be sold. Furthermore, modern commercial wind turbines already have the capacity for complex, computer based control schemes, particularly for production regulation, and have weather stations installed in the turbine hub; thus, it is believed that the proposed fuzzy logic controller would add minimal cost to existing turbine technology.

In the field installation of the mock up turbine system with the proposed CF based self heating laminate, a number additional challenges to successful scale-up of the proposed system were encountered. Again, the mock up turbine system confirmed the laboratory results in demonstrating both the material system's effectiveness to perform the de-icing and anti-icing functions on a larger scale and the proposed fuzzy logic control system's improved efficiency as compared to on-off control, upon which most thermal control systems are based. In the on site testing in Alaska, the proposed controller had an energy savings of 23% in de-icing functions while maintaining comparable performance. Thermal images of the turbine blades throughout the

on-site testing demonstrated that the embedded CF elements are highly effective at providing targeted heating. Investigations of ice formation on installed commercial wind turbines as well as laboratory tests on small scale airfoils indicate that most rhime ice formation is localized to the leading edge of the blade and occurs most often near the tip of the blade. Thus, it is believed that the CF based laminate system can be designed to target only the most likely areas of ice formation on the blade, reducing material and electrical costs by reducing the area of the required heating footprint.

However, during the process of the on site testing, significant challenges to scale up of the proposed CF based laminate system for wind turbine blade de-icing where encountered. First, the installation of electrical connections between the embedded CF element and the power source was non-trivial. Due to both contact resistance and the Peltier effect, the contact points between the copper wiring and the CF rose to temperatures significantly higher than the target heating area, in some cases reaching temperatures as high as 100°C. In fact, during transportation of the blades from UH to UAA, on electrical connection was damaged and the resulting increase in contact resistance resulted in the eventual burning of the electrical connection after installation. Due to the temperature sensitive mechanical properties of viscoelastic thermosetting polymers, such as epoxy, which lose significant stiffness beyond its glass transition temperature (typically 100-150°C), thermal management around the electrical connections is key to not only long term operation of the heating system, but also the structural integrity of the turbine blade.

Additionally, it should be remembered that the target application of the proposed CF based heating laminate is in large scale structures. Thus, some understanding of how the structural properties of the material may be altered to the repeated heating and cooling of de-icing and anti-icing functions should be understood. In the following chapter, an investigation of the effect of the thermal cycling induced by the embedded CF element on the tensile material properties of the CF-fiberglass-epoxy laminate will be presented.

Chapter 4 Investigation of Thermal Cycling Effects on Mechanical Properties of Self-Heating Carbon Fiber Reinforced Laminate Composites

4.1 INTRODUCTION

Though the CF tape enhanced laminate composite has shown great potential as a multi-functional material which provides self heating capabilities, for practical application and deployment, it must be ensured that the heating function of the materials does not compromise the actual structural properties of the composite. Though CF has been shown to significantly increase the strength of composite materials, it must be kept in mind that with repeated heating, the material must now be considered, in a way, a dynamic material whose properties may be altered over time due to repeated operation. Proposals to use the heated CF laminate must, therefore, be accompanied with some study of the progression of material properties with repeated heating and cooling cycles to gain a more complete understanding of the material system's behavior.

This chapter presents the experimental work done to understand the progression of basic tensile material properties of the proposed self-heating CF enhanced polymer laminate composite with repeated heating and cooling cycles. The chapter begins with a literature review on thermal effects on laminate composite mechanical properties, focusing on the two main topics of thermal fatigue and thermal shock. Then, the experimental procedure is presented, including the fabrication and design of samples and tensile testing procedures. Finally the tensile testing results with respect to number of heating and cooling cycles will be presented and discussed.

4.2 LITERATURE REVIEW OF THERMAL EFFECTS ON LAMINATE COMPOSITE MECHANICAL PROPERTIES

In the case of the proposed self-heating CF-fiberglass-epoxy laminate system, repeated thermal cycling is an integral portion of its operation. Since the heating element itself is embedded into the laminate and a sizeable portion of the laminate participates in the heating event, it is of great importance to investigate the effects of repeated thermal cycling on the material mechanical properties.

Thus far, reports of thermal cycling fatigue have focused on relatively high thermal gradients, with a focus on the effect of microcracking due to thermal expansion mismatch between constituent components. Papanicolaou et al. investigated the effect of repeated thermal shock on the creep compliance of fiberglass-epoxy specimens with a cycling profile of -27°C to 50°C at a duty cycle of 10 minute interval (5 minutes at each temperature) over 50 cycles. They found that due to thermal expansion mismatch between the constituent components, microdamage was accumulated quickly with increasing number of cycles until a damage saturation plateau was reached. Owens and Schofield [58] employed high thermal gradient thermal shock (from -18C° to 232°C) with a high degree of thermal cycling (up to 5000 cycles) on carbon fiber-polyimide polymer laminates. Their findings indicate that thermal cycling at high thermal gradients resulted in microcrack initiation and growth throughout the thermal cycling process. Matrix dominated properties, such as compressive strength, were degraded while fiber dominated properties, such as tensile strength, so no reduction. Ray found that [59][60] while there is significant reduced strength in polyester-fiberglass composites due to thermal cycling, these effects were much less pronounced in epoxy-fiberglass composites due to better matching in the thermal expansion properties. The general findings above were supported by the review by Hancox [61], who found that most investigations of thermal cycling reported micro-cracking due to internal stresses in the

composites were reported along with reduced flexure and tensile strength with increased thermal cycling.

While the literature indicates that thermal cycling can have detrimental effects on the materials' mechanical properties, these reports largely focus on large thermal gradients, sometimes in the hundreds of degrees Celcius. Furthermore, the sources of the thermal heating were external; in the proposed system, the internal heating source may lead to reduced thermal shock since the temperature distribution is not uniform through the sample and more subtle differences in thermal expansion may result. The following presents the experimental work conducted on measuring effect of thermal cycling on the tensile strength of the proposed laminate composite samples.

4.3 SAMPLE PREPARATION

4.3.1 CF Reinforced Laminate Fabrication

Self heating composite laminate samples were prepared to match those used in the de-icing applications presented in Chapter 3. In accordance to ASTM D3039 testing standards for tensile properties of laminate composites, laminate bar samples of the proposed CF reinforced self heating composites were prepared. For uniformity of properties, two sets of samples were prepared. For each set, the samples were formed by hand lay-up from the same batch of amine hardened epoxy and 18" x 30" swaths of woven fiberglass roving fabric. To provide the self heating functionality, 1" wide, 22" long carbon fiber tapes were placed in the lay-up as shown in Figure 40. After the lay-up procedure, the laminate was vacuum bagged at 25" Hg vacuum pressure for 24 hours before being demolded. The samples were allowed an additional 24 hour cure time before being cut apart into the samples of dimension shown in Figure 40.

Thermocouples were embedded into each individual sample in the lay-up to provide temperature monitoring capabilities of the CF and surface layer temperatures at the positions.

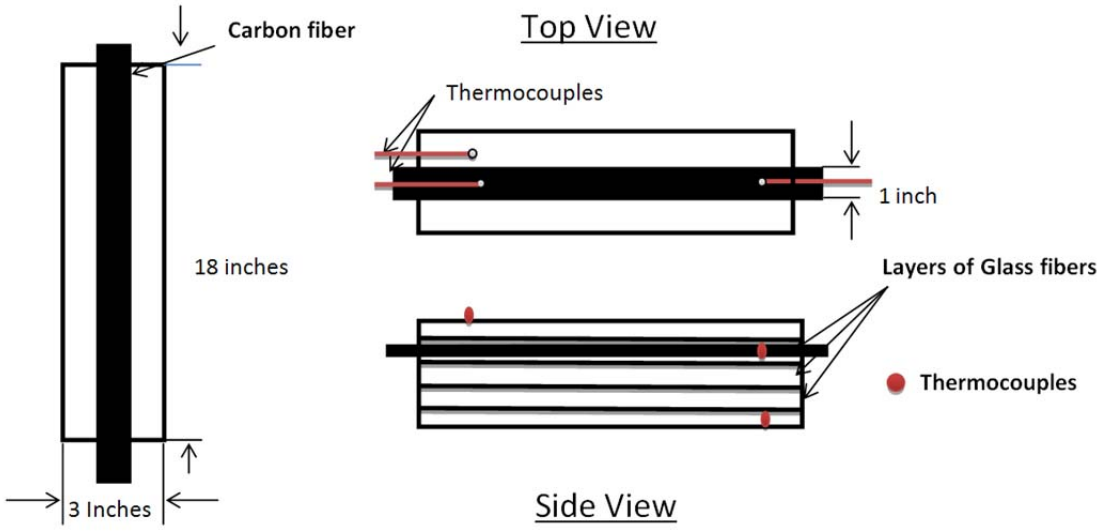

Figure 40: Lay-Up and dimensions of thermal cycling samples during fabrication

4.3.2 Thermal Cycling Procedure

To simulate the conditions of the de-icing application presented in Chapter 3, the CF reinforced laminate samples were placed into a freezer and brought to -20°C internal temperature. To provide the thermal cycling, the heating control system shown in Figure 41 was used to control heating of the CF to provide the desired surface temperature of 4°C, maintain the set point temperature for a period of 45 minutes, allow the system to cool back to -20°C, and maintain this cold temperature for a period of 45 minutes before repeating the heating-cooling cycle again. Thus, the term "thermal cycle" to be used in the rest of this chapter refers to a complete cycle of heating, maintain the "hot" temperature, cooling, and maintaining this "cold" temperature.

To investigate the progression of laminate mechanical properties with increased heating-cooling loading cycles, samples within the same set fabricated according to the procedure in the above section were heated through 0, 10, 25, 50, or 100 cycles before destructive tensile tests for

strength were performed. A sample time profile of a 6 thermal cycles is provided in Figure 42. The LabView block diagram for the automated sample thermal conditioning process is presented in Figure 41. During the heating-cooling treatment, the temperatures of the layers indicated in Figure 40 were recorded.

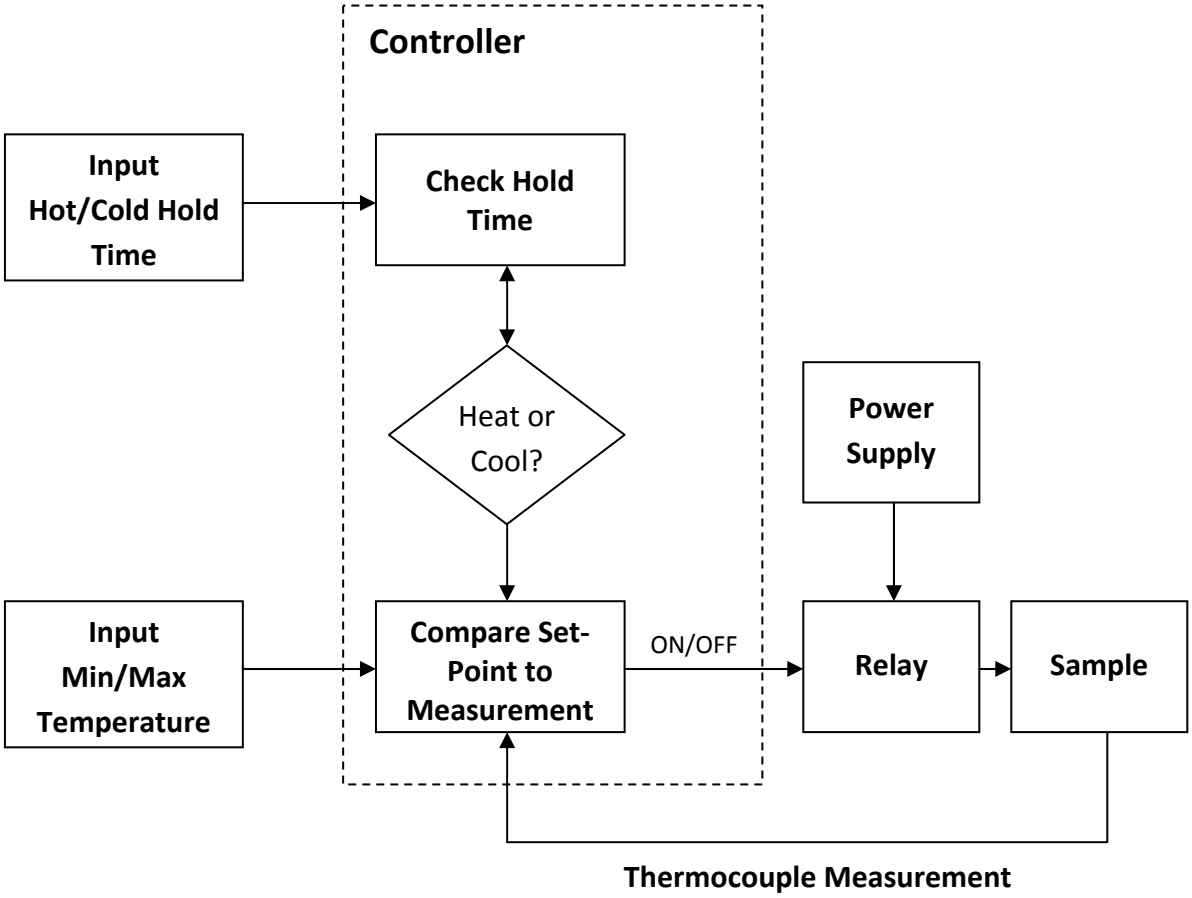

Figure 41: Block diagram of automated thermal cycling process

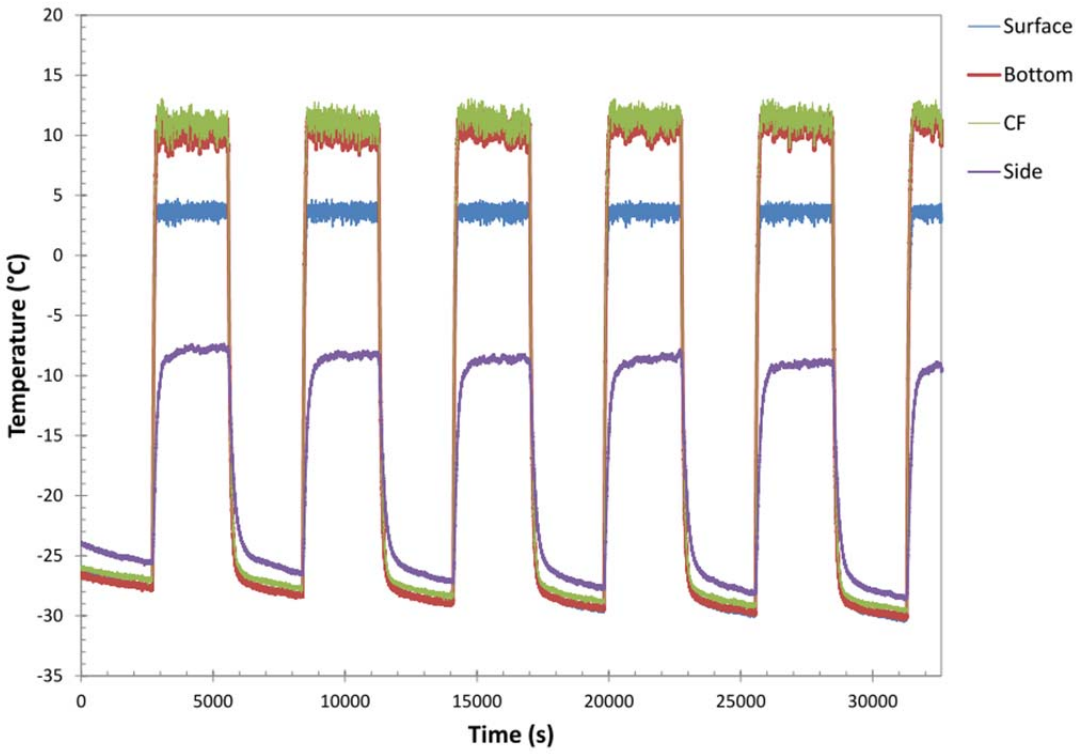

Figure 42: Thermal cycling treatment temperature recording (6 heating-cooling cycles)

4.4 MECHANICAL PROPERTY TESTING

After the thermal cycling treatment described in the above section was completed, tensile properties of the laminate specimens under uniaxial loading were measured using an Instron 6959 material testing machine. To fit the test fixture, the samples were cut to a nominal size of 2 inches × 12 inches. A photograph of the test set-up is presented in Figure 43. To allow proper stress distribution from the test grip to the composite sample, 2 inch wide aluminum tabs were bonded to the composite bars using high strength structural epoxy and the aluminum tabs were held by the test grip, as described in the ASTM D3039 standards [62]. A photograph of the test specimen is presented in Figure 44. Displacement quasi-static stress-strain tests were performed at a displacement rate of 0.01 mm/s.

Figure 43: Photograph of specimen in uniaxial testing machine

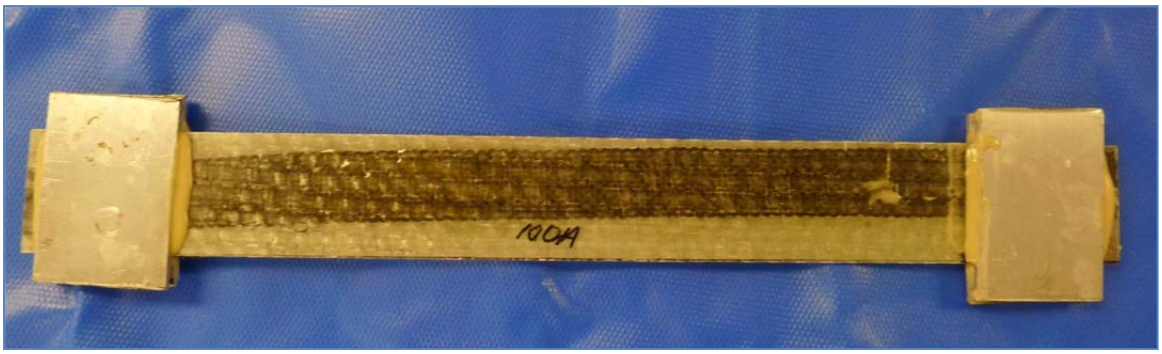

Figure 44: Photograph of laminate specimen with aluminum grip tabs for tensile property testing

4.5 RESULTS

The laminate coupon samples were extended in uniaxial tension until fracture. Due to the brittle nature of both the glass fiber and carbon fiber reinforcement, the coupon specimens experienced brittle failure due to fiber fracture. A photograph of a fractured sample is presented in Figure 45. It can be seen that the relatively straight fracture surface is consistent with brittle

fracture, with the fracture angle lining up with the offset skew angle of the cross-weave of the glass fiber.

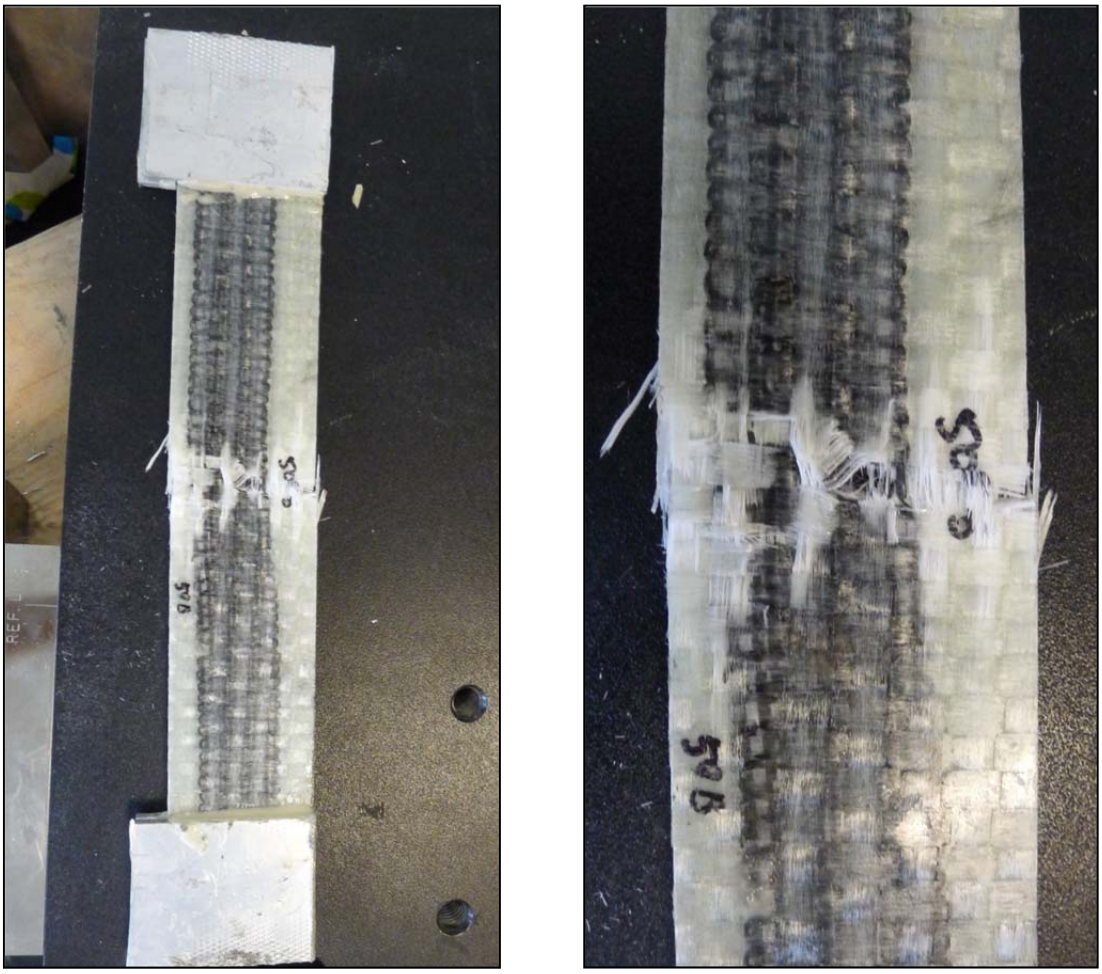

(a) **(b)**

Figure 45: Photograph of fractured laminate sample (a) full length of sample and (b) detail of fracture

The stress-strain results from the tensile tests are presented below in Figure 46. From the stress-strain curves, it can be seen that the specimens load history is consistent with brittle failure – from the onset of loading, the behavior of the composite is almost completely linearly elastic, followed by an abrupt drop in supported load due to fiber failure. Failure occurs at low strain levels, in this case 4.2% and below of the original sample gage length. Though there is

some variability in the fracture strain, it can be seen that both the ultimate stress and the slope of the linear sections of the stress-strain curves (and thus the elastic modulus) are comparable.

However, due to the amount of data, direct comparison of the stress-strain curves does not clearly give any relationship between thermal cycling and mechanical properties of the composite samples. Using the results of the tensile tests, the fracture stress, fracture strain, and the elastic modulus of the laminate samples were computed and plotted against the number of thermal cycles to track the effect of thermal cycling on these major mechanical material properties. The results are presented below in Figure 47 to Figure 49, respectively.

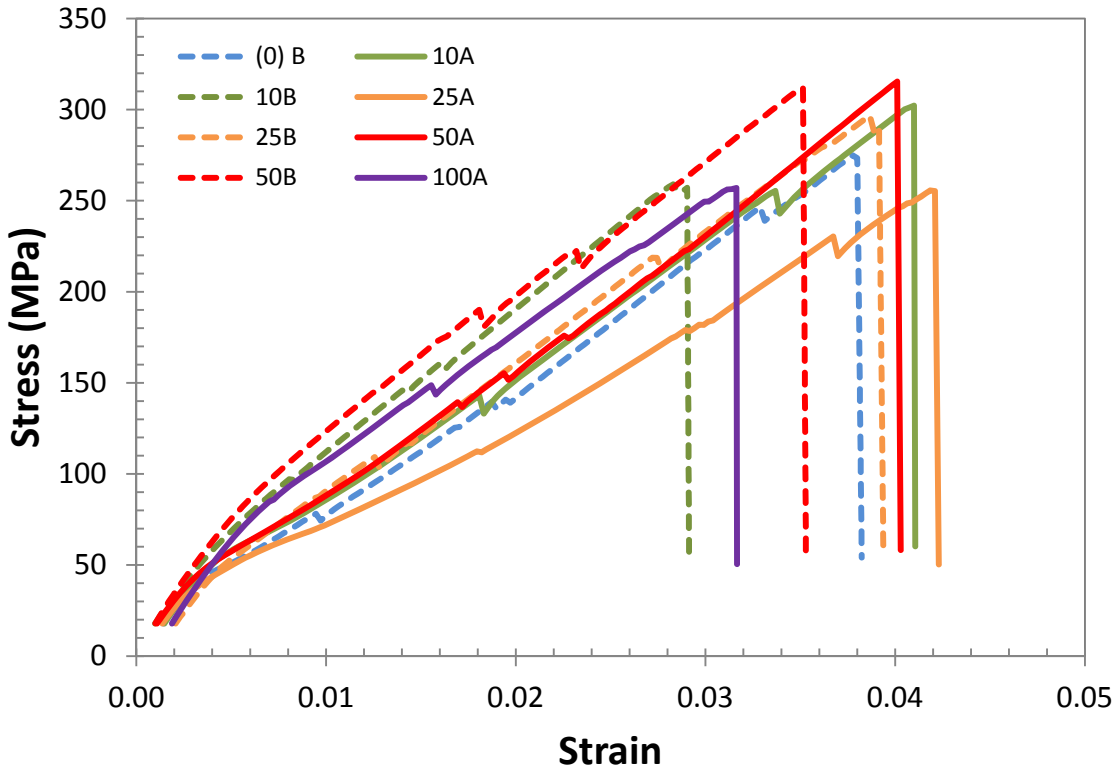

Figure 46: Stress-Strain Curves of Thermally Cycled Laminate Samples

First, the fracture stress was taken to be the engineering stress of the material just prior to material failure and the sudden drop in supported load. The fracture stress of the samples is

plotted against the number of thermal cycles in Figure 47. From the figure, no significant change in fracture stress is observed as the number of thermal cycles is increased. For all samples, the average failure stress was calculated to be 292 MPA, with all data points falling within ±12% of the average failure stress.

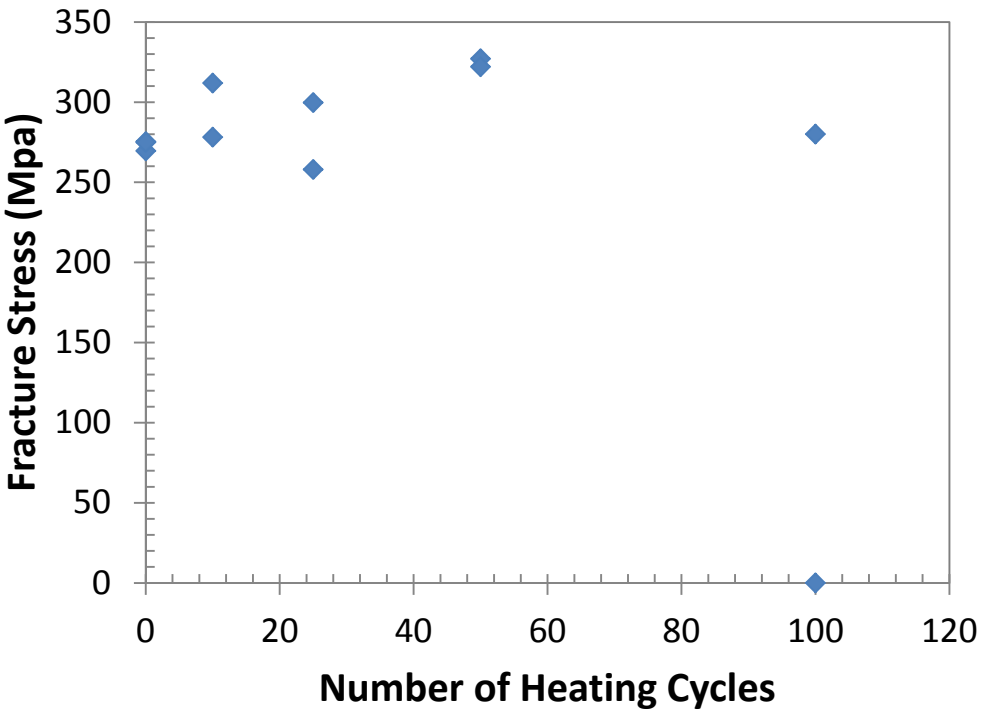

Figure 47: Fracture Stress of Thermally Cycled Laminate Samples

In addition to the fracture stress as a measure of strength, the fracture strain corresponds to the ductility of a material and provides a measure of the amount of deformation which can be sustained before total failure of the material. The fracture strain plotted against the number of heating cycles in presented in Figure 48. Here, it can be seen that as the number of thermal cycles increases, there is a gradual decrease in fracture strain from 25 cycles to 100 cycles; however, considering the whole of the data, there is no appreciable decrease in fracture strain. In fact, as compared to the unheated samples, the fracture strain of the heated samples has increased.

The scatter in the data, however, suggests that any small observed trend in fracture strain should be investigated further with more testing to develop a better statistical profile of the fracture strain.

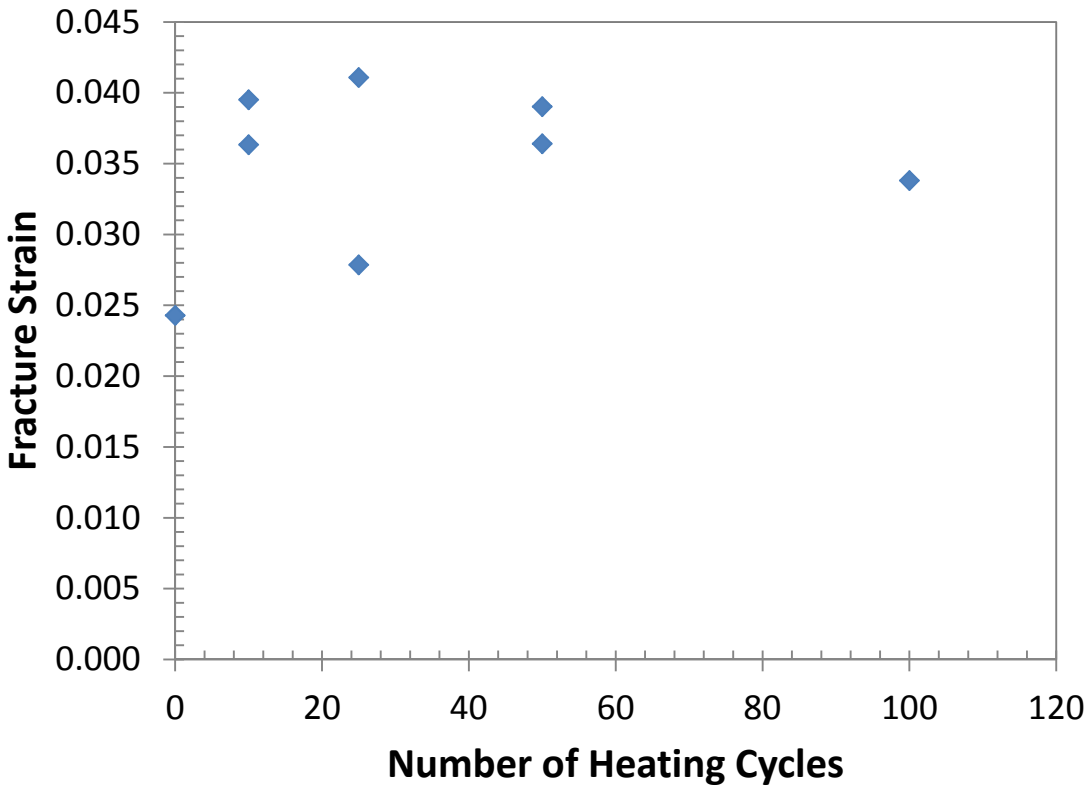

Figure 48: Fracture Strain of Thermally Cycles Laminate Samples

Finally, a comparison of the elastic modulus is presented in Figure 49. The elastic modulus directly indicates the stiffness of a material, which in turn is a direct factor in both static (such as displacement of a beam due to an applied load) and dynamic (such as the natural frequency) behavior of structures made of the material. To calculate the elastic modulus, a linear regression fit of the stress-strain curve data from 0.8% strain to failure was conducted and the slope value taken to be the elastic modulus. In the small region from 0%-0.8% strain, all samples exhibited a small non-linear region. This non-linear behavior is likely due to the stretching of the complex, folded polymer chains in the epoxy matrix prior to full load transfer of the stress to the stiff glass and carbon reinforcements. Consistent with the visual observation of similar slopes in

the stress-strain curves in Figure 49, it is seen in the plot of elastic modulus vs. number of thermal cycles that there is no significant change in stiffness of the material despite thermal conditioning.

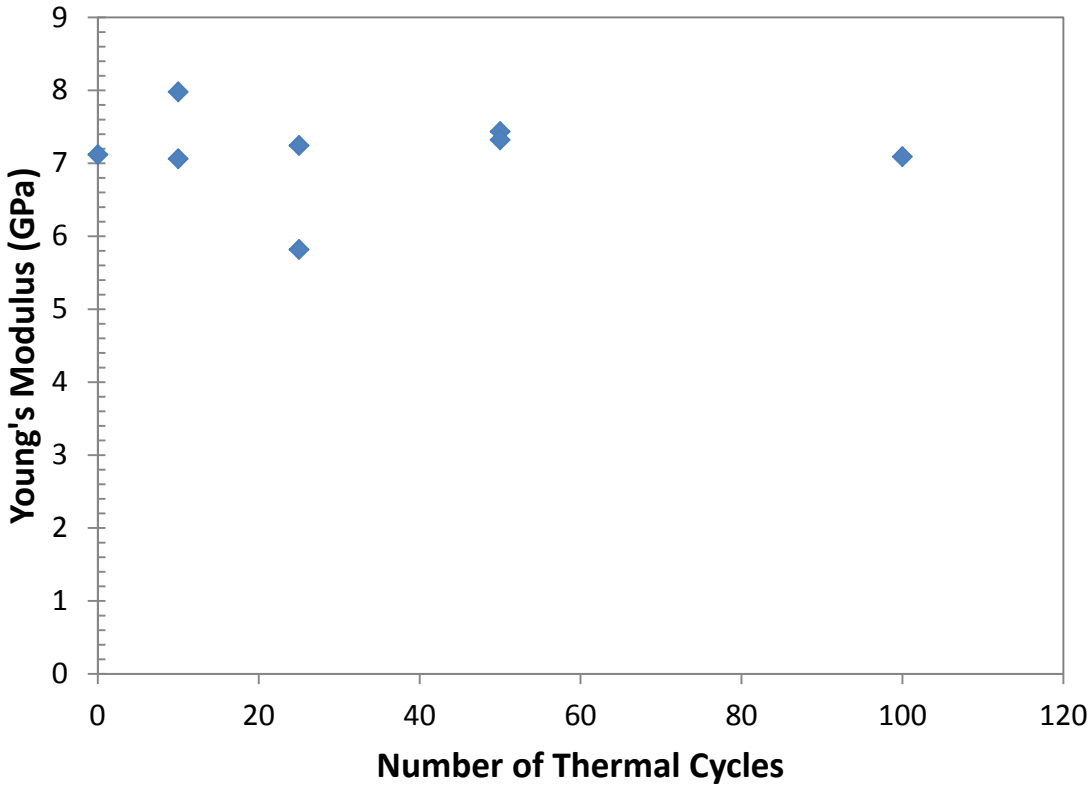

Figure 49: Elastic Modulus of Thermally Cycled Laminate Samples

4.6 DISCUSSION

From the presentation of the progression of fracture stress, fracture strain, and elastic modulus with increasing numbers of thermally cycling using the proposed embedded CF tape self-heating strategy, it can be seen that this internal heating has minimal effect on these major tensile material properties up to 100 thermal cycles. In the case of the fracture stress, which in this case is also the ultimate strength of the composite, and the elastic modulus, there was no significant change in properties as the samples underwent increased thermal cycling, with all data points falling within 12% and 18% of the control samples (i.e., – samples which underwent no thermal cycling but were cured in identical conditions) for stress and modulus, respectively.

These findings are encouraging, as they indicate that the self-heating laminate composite strength will not deteriorate due to the heating process and that no loss of structural rigidity will be seen. Though strength is often a key marker for structural properties, it should be remembered that in the case of wind turbine rotors, the constant rotational motion of the blades make the structural dynamics of the system equally, if not more, important due to the implications on structural loads and fatigue. Thus, the relative stability of the elastic modulus, and thus stiffness, of the material helps to ensure stable dynamic properties, such as natural frequencies and mode shapes, which can significantly compromise the structural design due to redistribution of structural loads and strains.

However, as the number of thermal cycles increased, there was a slight decrease in the fracture strain, indicating that the thermal cycling procedure may adversely affect the ductility of the material. Knowledge of the fracture strain of brittle materials is critical due to their sudden, catastrophic failure nature. In our experiment, at fracture the samples nearly universally experienced complete fiber fracture throughout the cross-section of the material, resulting in sudden loss of all load bearing capacity. Again, as noted earlier, the fracture stress remained relatively constant for all samples though the fracture strain had larger variability. In the case of structural design with our proposed self-heating CF laminate, it may be advisable to use fracture strain limits as the major design parameter rather than fracture stress to safely account for the gradual loss of ductility. With additional testing with greater numbers of thermal cycles, a safe limit of ductility can be established for design purposes.

Overall, though, the thermal cycling procedure examined here resulted in only very limited effects on the tensile material properties of the self-heating CF laminate composite. Furthermore, it should be remembered that each heating-cooling cycle represents activation of the heating system for only a single icing event. In their review of icing event data in Europe, Durstewitz et al. [1] found that an average winter season saw only 10-15 icing events; thus, from

our experimental design, 100 thermal cycles corresponds to 6-10 years of field operation of the wind turbine blade. If we consider proposed Eurpoean classifications of icing site risk, "moderate" icing risks are defined by 1-5 icing days per year, with "heavy" risk ranging from 5-25 icing days per year. With these guidelines in mind, a wind turbine sited at a "moderate" icing risk site would experience 20 years of operation under the 100 thermal cycles considered in this dissertation. Although the design life of wind turbines is generally 20 years, an records of real world maintenance of wind turbines concluded that the actual average operation life of current technology wind turbine blades is only 6-10 years [63][64]. Thus, it is reasonable to believe that any degradation of mechanical properties seen in the results here would be in line with the overall damage accumulation over the typical operation life of the wind turbine blade. With proper design parameters accounting for the reduction in ductility over time, it is believed that the proposed self-heating CF laminate composite can be integrated with existing composite wind turbine blade designs with little change in structural properties.

In this chapter, the tensile mechanical properties of coupon samples of the proposed CF-tape reinforced self-heating laminate composite were experimentally obtained over range of thermal cycles to track the progression of the mechanical properties with repeated thermal loads due to the proposed de-icing function of the laminate. The results indicate that the fracture stress and elastic modulus had no significant change with increasing number of thermal cycles, while the fracture stress saw a 25% decline from 4% to 3% over 100 thermal cycles. However, the observed decline in fracture stress corresponds to a gradual decline over 7-10 years of a wind turbine blades operating life, after which most blades are replaced.

Chapter 5 Temperature Dependent Monte Carlo Simulation of Carbon-Polymer Nanocomposite Resistivity

5.1 INTRODUCTION

5.2 LITERATURE REVIEW OF FUNCTIONAL NANOCOMPOSITES

Though composites have been used as structural materials for some time, the development of nano-scale fillers and reinforcements has ignited a renewed excitement in composites due to the ability of nanofillers to enable additional functionalities, such as enhanced piezoresistivity, improved thermal conductivity, controllable optical properties, and chemical sensing abilities. In particular, carbon based nanofillers, such as carbon black, carbon nanotubes (CNTs), and carbon nanofibers (CNF), and graphene have drawn particular interest due to the extraordinary material properties enabled by their nanoscale architecture. High tensile strength, electrical conductivity, thermal conductivity, and aspect ratio have been predicted in theory and proved in experimentation. With extensive work already conducted on understanding the individual filler particle properties, work now commences on applications of these nanofiller composites, or nanocomposites, and constructing theoretical frameworks on how to control their bulk properties.

Though these carbon nanofillers have interesting physical properties of their own, it is perhaps what their nanoscale geometry enables that makes them of most interest in advanced material development. As shown by Alamusi et al., the addition of carbon black and multiwalled carbon nanotubes (MWCNTs) polyvinyl (vinyl fluoride) (PVDF) enhanced the polymer's piezoresistive properties by providing enhanced nucleation sites for the formation of piezoresistive β-phase polymer crystals. The high aspect ratio of CNTs and CNFs provides high

surface-area to volume ratios in the fillers, resulting in increased frictional contact between filler and matrix.

5.3 MONTE CARLO NUMERICAL SIMULATION OF TEMPERATURE DEPENDENT BULK RESISTIVITY

5.3.1 Monte Carlo Generation Of Physical Model

To represent the physical configuration of the nanoparticle reinforced polymer composite, Monte Carlo method is used to generate a random configuration of conductive stick elements within a representative volume of the bulk composite. In the numerical model, each conductive element is represented as a straight cylinder, or stick, of a prescribed diameter and aspect ratio, capped by two hemispheres. The position and orientation of the stick is generated randomly according to the following distribution:

$$x_0 = L_c \times \mathrm{rand}[0,1] \qquad x_f = x_0 + L_S \times \cos\phi\cos\theta, \tag{2}$$

$$y_0 = L_c \times \mathrm{rand}[0,1] \qquad y_f = y_0 + L_S \times \cos\phi\sin\theta, \tag{3}$$

$$z_0 = L_c \times \mathrm{rand}[0,1] \qquad x_f = x_0 + L_S \times \sin\phi, \tag{4}$$

where *x,y,z* gives the Cartesian coordinates of the endpoints of an individual stick and the subscripts *0* and *f* represent the origin and endpoint of the stick, respectively. *Lc* is the length of one edge of the cubic unit cell and L_S is the length of the stick, as determined by the stick diameter and aspect ratio. The angles ϕ and θ describe the rotation of the stick about its origin and are defined in Figure 50. The values of ϕ and θ are determined by the distribution given by

$$\theta = 2\pi \times \mathrm{rand}[0,1] \tag{5}$$

$$\phi = \mathrm{acos}(1 - 2 \times \mathrm{rand}[0,1]), \tag{6}$$

where *rand()* is a uniform distribution over the input interval.

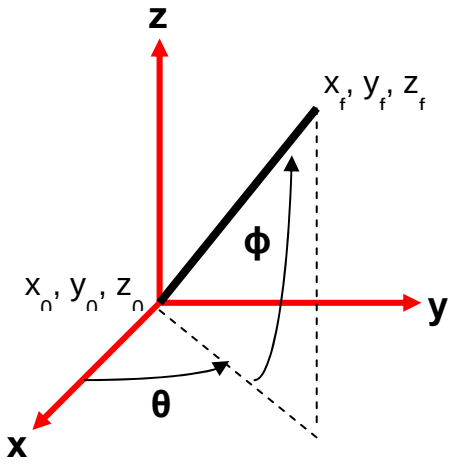

Figure 50: Definition of Stick Orientation Angles

5.3.2 Monte Carlo Simulation Procedure and Structure

With the physical parameter models described in the previous sections, a Monte Carlo simulation was developed to produce conductive fiber networks matching given fiber volume fraction loadings and to transform the fiber network into a corresponding resistor network model for final analysis in commercial SPICE based circuit analysis software. As this project is a continuation of that of Yu et al., the methodology presented is very similar to that described in [65].

A flow chart of the Monte Carlo simulation procedure is given in Figure 53; the overview is given here and detailed algorithms in following sections. At the beginning of the simulation, and empty representative volume element (RVE), essentially a unit cell volume within the bulk composite material, is created and Stick objects representing individual fiber elements are individually added into the RVE. In our simulation, the RVE is taken to be a cube element with edge length equal to 3-5 times the length of a single Stick objects. After a single Stick object is created in the RVE, a periodic boundary condition (PBC) is enforced by preventing individual

Stick elements from crossing the faces of the RVE. If the Stick element does cross the face of the RVE, the point of intersection is calculated and the out-cropping portion of the Stick is translated to the opposite face such that if two RVE are placed adjacent to each other, tessellation results. A 2D representation of this tessellation concept is presented in Figure 53. A low loading RVE is presented in Figure 52 for visualization.

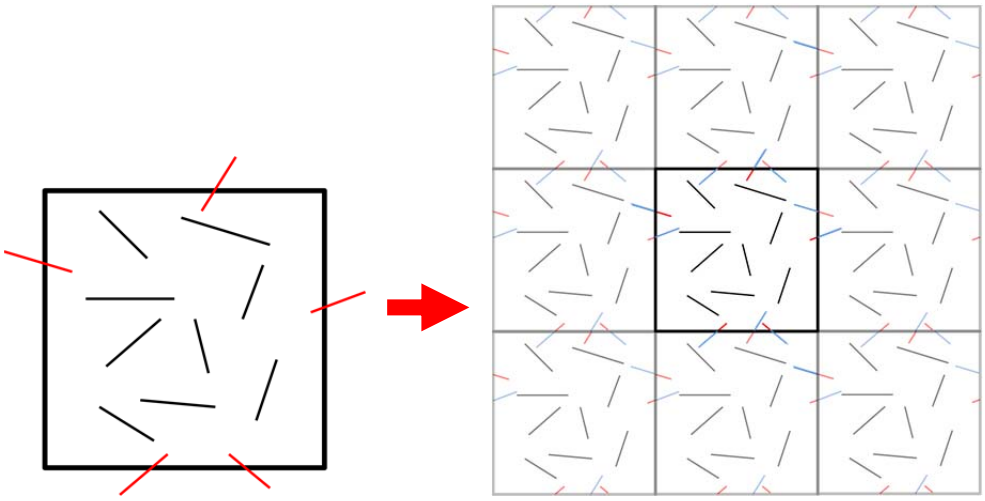

(a) **(b)**

Figure 51: PBC enforcement - (a) individual RVE and (b) tesselated RVE

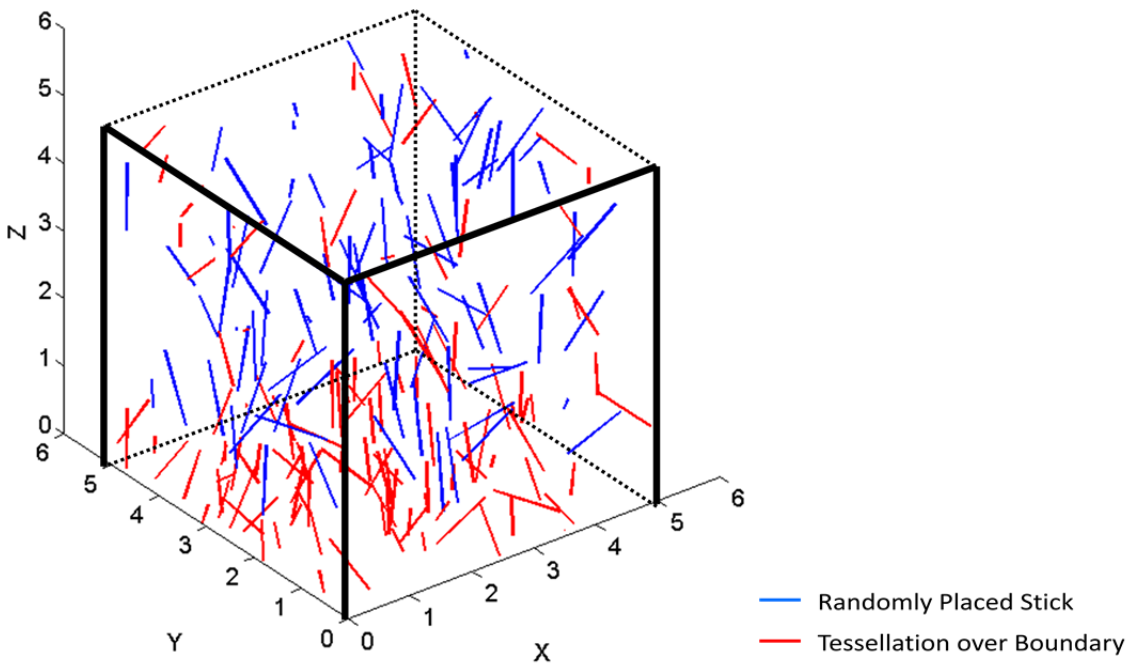

Figure 52: 3D RVE with enforced PBC conditions

A conductive network exists when there is a path from one face of the RVE to the opposite face of the RVE comprised of connected Stick elements. After a Stick is added to the RVE and the PBC condition enforced, the shortest distance between each pair of Sticks in the network is calculated to determine if the pair of Sticks are in contact. If the pair is in contact, they are assigned to the same cluster of Sticks. If a single cluster is found to span across the RVE from one face of the cube to the opposite face, then the cluster is said to span the RVE and the network is percolated. Sticks are added until the network percolation condition is met; if percolation is not detected, then the network is represented as an open circuit and no effective resistance of the RVE can be calculated. Once network percolation is achieved, Sticks continue to be added to the RVE until the total volume fraction specified by the simulation is reached.

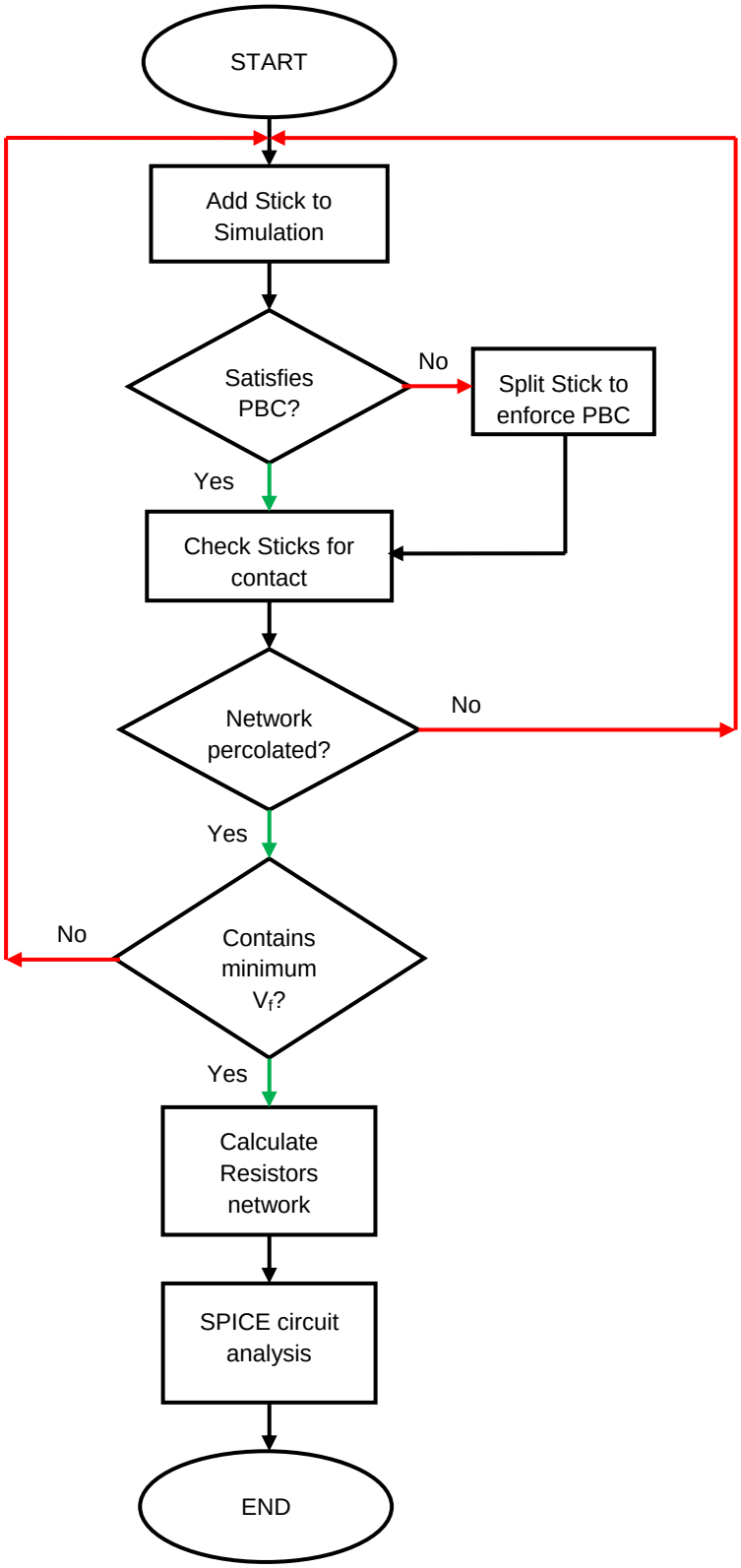

Figure 53: Monte Carlo Simulation Flow Chart for Percolation Threshold

After the tunneling conductivity for each fiber-fiber connection is calculated, the resistor network is compiled into a netlist compatible with SPICE circuit simulation software to calculate the effective resistance of the resistor network. Though there are many commercial SPICE based circuit simulation packages available, the program LTSpice IV was used in this research to complete the circuit analysis.

5.3.3 Modeling Of Junction Resistance

In the case of filled polymer composites, thin layers of the polymer matrix separating individual filler particles provides an electrically insulating layer which inhibits the transport of electrons from one filler particle to the other. However, though the polymer is insulating, the combination of thermal energy and electrical potential across the polymer at the particle-particle junction site can overcome the electron transport barrier, resulting in electrical tunneling of electrons through the insulating polymer. A number of analytical models to estimate the resistance of such tunneling junctions have been given. Simmons gives a generalized expression for the tunneling resistance between two similar electrodes through an insulating layer for a range of applied voltages [66]. For low applied voltages, generalized tunneling current density expression can be simplified to

$$J = \frac{I}{A} = J_L V\sqrt{\lambda}\exp\left(-A_D\sqrt{\lambda}\right), \tag{7}$$

where J is the tunneling current density, I is the tunneling current, A is the tunneling cross-sectional area, V is the applied voltage, λ is the barrier height of the insulating film, and A_D is the expression

$$A_D = \left(\frac{4\pi d}{h}\right)\left(\sqrt{2m}\right), \tag{8}$$

resulting from the tunneling probability function $D(E_x)$ where E_x is the electron energy component in the x-direction (direction of tunneling), d is the separation distance between conducting elements (or, equivalently, the thickness of the insulating film), h is Planck's constant, and m is the electron mass. Also, the expression J_L is given as

$$\mathrm{J_L} = \left(\frac{\sqrt{2\mathrm{m}}}{\mathrm{d}}\right)\left(\frac{\mathrm{e}}{\mathrm{h}}\right)^2. \tag{9}$$

Substituting (8) and (9) into (7) and recognizing that Ohm's law can be rewritten as

$$\mathrm{V} = \mathrm{IR} = (\mathrm{AJ})\mathrm{R}, \tag{10}$$

the tunneling resistance, R_{Tunnel}, can be written as

$$\mathrm{R_{Tunnel}} = \frac{\mathrm{V}}{\mathrm{AJ}} = \frac{\mathrm{h^2 d}}{\mathrm{Ae^2}\sqrt{2\mathrm{m}\lambda}} \exp\left(\frac{4\pi\mathrm{d}}{\mathrm{h}}\sqrt{2\mathrm{m}\lambda}\right). \tag{11}$$

Thus, we can calculate the tunneling resistance between two conducting fibers due to a thin insulating film as a function of the separation distance between the two fibers, d, and the barrier height of the insulating matrix material, λ. The tunneling conductivity can be calculated as

$$\sigma_{\mathrm{Tunnel}} = \frac{\mathrm{d}}{\mathrm{AR}} = \frac{\mathrm{e^2}\sqrt{2\mathrm{m}\lambda}}{\mathrm{h^2}} \exp\left(\frac{-4\pi\mathrm{d}}{\mathrm{h}}\sqrt{2\mathrm{m}\lambda}\right) \tag{12}$$

and gives us a material property of our system with which we can use to compare to the electrical properties of different materials. The tunneling resistance and conductivity for different barrier height values over a range of separation distances is given in Figure 55. From the conductivity plot, it can be seen that the ability of charge to tunnel through an epoxy thin film insulation layer drops off very quickly with increasing film thickness; it is reasonable, then, to set a cut-off separation distance, d_{max}, beyond which the conductivity of the tunneling junction is negligible and the two conducting fibers are not considered to be in contact. In this simulation, the cut-off distance is taken to be 1.0 nm, at which the tunneling conductivity is very low ($< 10^{-2}$ S/m) and is 3 orders of magnitude lower than the conductivity of CNT. Furthermore, in reality, the CNT and

epoxy molecules cannot penetrate into each other. Thus, there are limits to the separation distances between the CNTs; at the lower limit, the individual CNTs are separated by the epoxy molecules. Studies have shown that taking into consideration Lennard-Jones potential or van der Waals forces, the average minimum separation distance, d_{min}, ranges from 0.3 nm to 0.5 nm. Thus, though the CNTs are considered to be in contact if the distance between the centerlines of the two CNTs, d_{CNT}, meets the condition

$$d_{CNT} \leq D + d_{max}, \tag{13}$$

where D is the diameter of an individual CNT, the actual separation distance between the CNTs is adjusted such that

$$D + d_{min} < d_{CNT} \leq D + d_{max}. \tag{14}$$

It should be noted, however, that it is the insulating film thickness, d, where

$$d = d_{CNT} - D, \tag{15}$$

that determines the tunneling resistance as calculated in (11), not the strict distance between CNT elements. A schematic diagram of the tunneling resistance distances are presented in Figure 54.

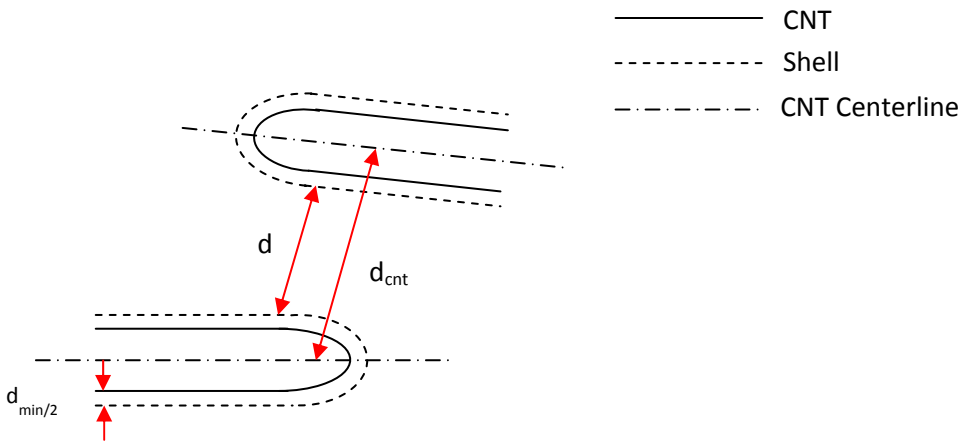

Figure 54: Schematic of separation distances for tunneling resistance calculation

In addition to the tunneling resistance, the inherent resistance of the conducting CNT elements also contributes to the network resistance. However, the conductivity of CNT is very high, measured experimentally to be between 10^4 - 10^7 S/m. In this paper, the inherent resistivity of CNT is taken to be 10^4 S/m; additionally, the CNT is considered to be multiwalled CNT (MWCNT) consisting of three layers of graphene. As the effective thickness of a single graphene layer is approximately 0.1nm, the CNT is considered to be a cylinder with outer diameter of 50nm and inner diameter 49.4nm. The resistivity of the CNT segment is calculated using the bulk resistivity equation and the length of CNT between contact points.

A summary of the material system physical parameters used in the Monte Carlo numerical simulation is given below in Table 6.

Table 6: Monte Carlo numerical simulation physical parameter values

Property	***Value***
d_{min} (nm)	0.43
d_{max} (nm)	1.0
Epoxy Bandgap (eV)	1.25
CNT Aspect Ratio	100
ρ_{CNT} (Ω-m)	10^{-4}

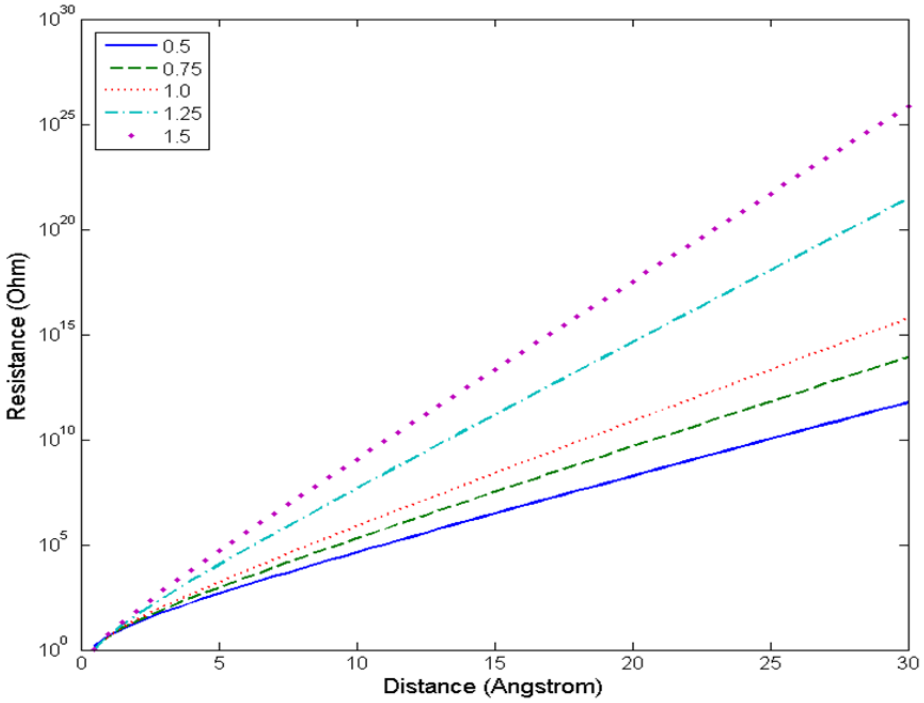

(a)

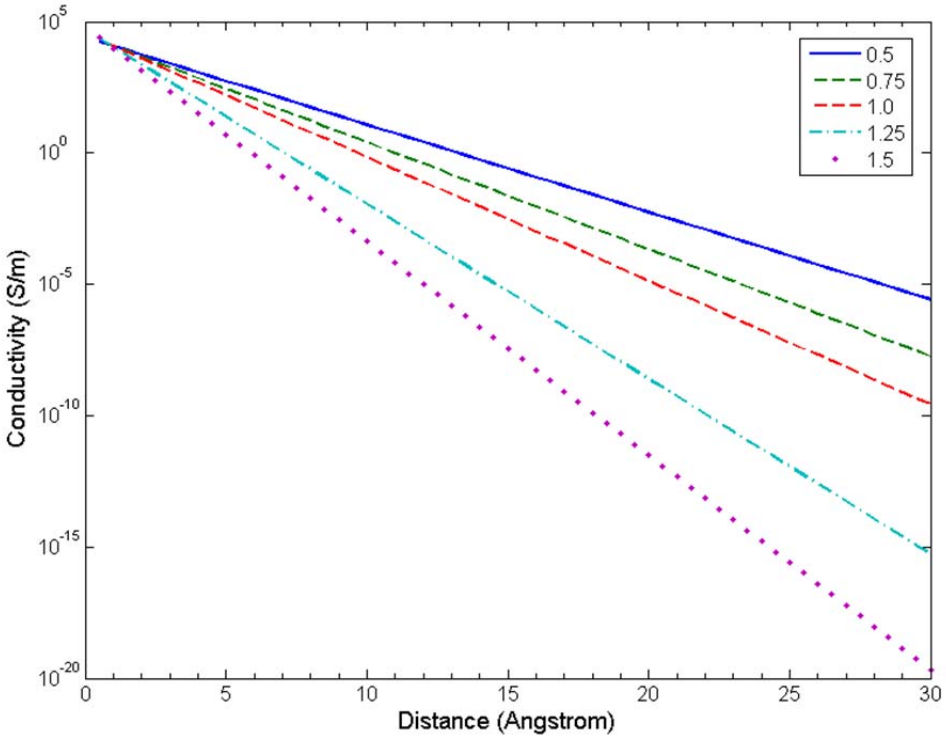

(b)

Figure 55: (a) Tunneling resistance and (b) tunneling conductivity of CNT-epoxy junction with varying band gap energy and separation distance

With the resistances between pairs of contacting CNTs calculated, a resistive network can be formed if the network is percolated, or forms a connected path from one electrode face to the other. A schematic of the resistor network formation is given in Figure 56. First, individual pairs of connected CNTs are checked for separation distance and a resistor element is assigned with connectivity between these two fibers, as shown in Figure 56(a). Such connectivity testing is performed for all pairs of fibers in the RVE. After the all resistor elements have been created, a further connectivity check is performed to filter out only the resistors which contribute to conducting clusters, or groups resistors which have connectivity to the conduction path. Finally, a second round of filtering creates a final resistor network node graph which contains only fully connected resistors (both ends of the resistor are connected to CNTs) participating in the conduction network. The final resistor network, as shown in Figure 56(b), is entered into the LT Spice IV commercial circuit simulation tool with an applied DC voltage of 1 nV and the resulting DC source current (current across the 1 nV source) calculated numerically using an iterative Newton-Ralphson solver. The resistance of the RVE was calculated using Ohms law and the dimension of the RVE further used to calculate the bulk resistivity according to

$$\rho = R\frac{A}{L}, \tag{16}$$

where A is the cross-sectional area of the bulk sample perpendicular to the current flow and L is the length of the bulk sample along the length of the current flow.

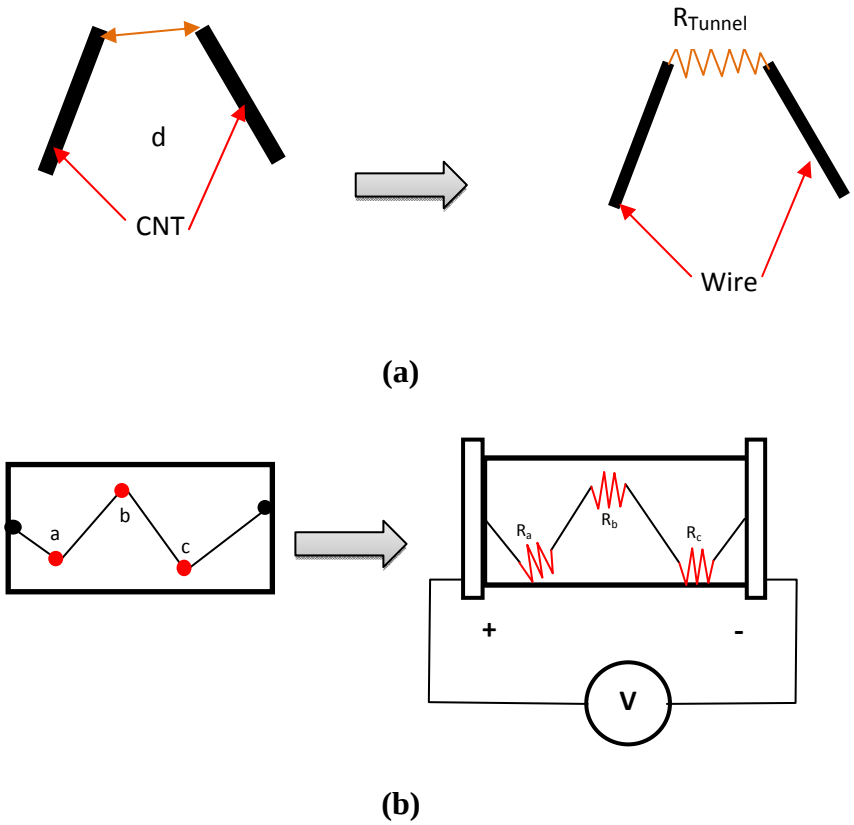

Figure 56: Schematic of tunneling resistance (a) Resistor between individual fibers and (b) formation of resistor network

The percolation thresholds (i.e., – the minimum volume fraction of CNT at which a conducting network is formed) calculated by the designed Monte Carlo simulation for different aspect ratios (the ratio between CNT length and diameter) is presented below in Figure 57. Though experimental and numerical results give percolation thresholds of as low as 0.03% volume to as high as 3% volume for CNT, the results presented fall well within that range and match well with [67] and [68]. As it can be seen, the percolation threshold is dramatically reduced with long aspect ratios, highlighting the appeal of extremely high aspect ratio fibers such as CNT. As the fibers become more slender, less volume of filler is needed to produce conductive networks, reducing the amount of filler needed (which can degrade mechanical performance) and providing additional advantages such as maintaining the transparency of the matrix [44]. Low filler contents also aid in fabrication processes by maintaining the low viscosity

of uncured matrix resins. However, beyond and aspect ratio of 250, the rate at which the percolation threshold decreases flattens and diminishing returns are seen as the aspect ratio increases to 500. Thus, it is reasonable to believe to that in most applications, aspect ratios of up 250 (a range which includes multiwalled CNT) are sufficient.

For the purposes of the temperature effect study, the CNT aspect ratio is taken to be 100 to match with the experimental verification presented in a later section. At 100 aspect ratio, the calculated percolation threshold is 0.764% volume, similar to values found in other Monte Carlo simulations [67][68] which found the percolation threshold to be approximately 0.68% volume. This slight difference may be due to slight variations in the simulation, such as the ratio of CNT length to RVE size, the enforcement of the PBC condition, and the form of the CNT element.

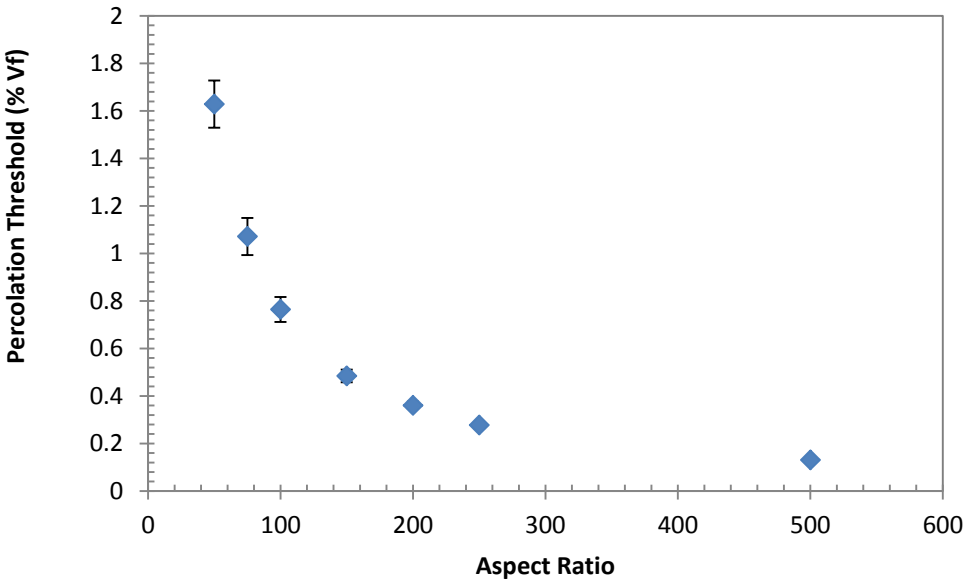

Figure 57: Percolation threshold vs. aspect ratio

After the percolation of the network was calculated, the constructed resistor network was evaluated for its DC electrical properties. The conductivity (inverse of resistivity) of CNT aspect ratio 100 and volume fraction loading ranging from 1%-10% is presented below in Figure 58. The numerical results show the expected percolation behavior, with the conductivity (a

normalized, bulk measurement of electrical conductance) suddenly shooting up beyond the calculated percolation threshold of 0.764% volume and remaining within the same range as additional conducting fibers are added. Comparison with other numerical and experimental results shows good agreement Figure 58, with results falling within the same order of magnitude. Some value differences can occur due to variations in simulation parameters and experimental parameters that are difficult to control, such as fiber alignment.

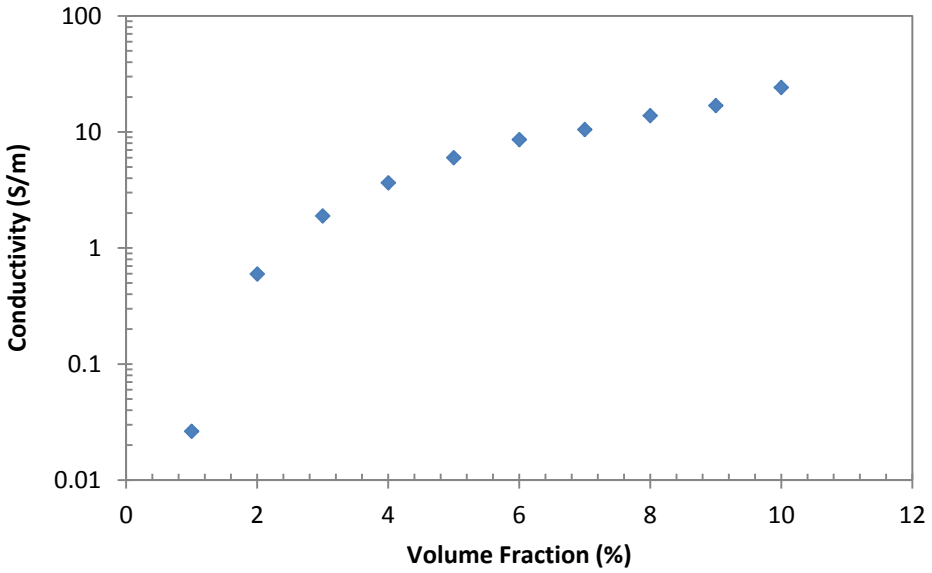

Figure 58: Conductivity vs. Volume Fraction

5.3.4 Strain and Conduction Network Breakdown

The electrical conduction of the composite is directly related to the connectivity of the network of conducting fiber elements, called the conduction network, and its ability to allow electrons to travel through the fibers and thin insulating layers of matrix material. It has been shown through modeling and experiment that straining the composite leads to shifts in the positions of the conducting fibers and, ultimately, changes in the connectivity of the conduction network. Though the shifts in position are small, the aggregate result on the conductivity of the conduction network is significant and leads

of observable changes in the composites' electrical behavior. Thus, it is reasonable to consider the possible effects of thermal expansion on the repositioning of fibers in the conduction network as a possible source of temperature sensitivity of short fiber reinforced composite electrical conductivity.

Prior to application of composite thermal expansion to the conductive network, verification of the effects of strain on the designed Monte Carlo model were conducted to ensure accurate reproduction of thermal expansion effects on the resulting conductive network breakdown. It has been frequently observed that conductive fiber filled composites can be effective strain sensors, likely due to reorientation and repositioning of conductive fibers due to the composite strain resulting in altered conductive network structures. The method presented by Hu et al. [40][39] is used here to verify the accuracy of the developed Monte Carlo model to represent the effects of strain on the conductive network.

To calculate the effect of strain on the physical reorientation of individual conductive fibers in the matrix, the strain reorientation model presented by Taya et al. [6] was used to update the fiber orientation angles after the virtual application of a specified axial strain along one dimension of the representative volume element (RVE) of the composite. Consider the 3D orientation of a short fiber element in an RVE as described in Figure 59. Note, the definitions of the orientation angles differ slightly than presented previously; the notation used in the reference [6] is kept for clarity. The cubic RVE surrounding a single short fiber with edge length L prior to the applied strain, as shown in Figure 59b, is considered. After the application of a finite strain, $\Delta\varepsilon$, the RVE is elongated and in the x-direction and contracted in the y- and z-directions, as shown in

Figure 59. As a result, the orientation angle of the short fiber, θ, and the position of the mid-point of the short fiber, denoted using the coordinates x, y, and z, are changed and denoted with the ‘ marker.

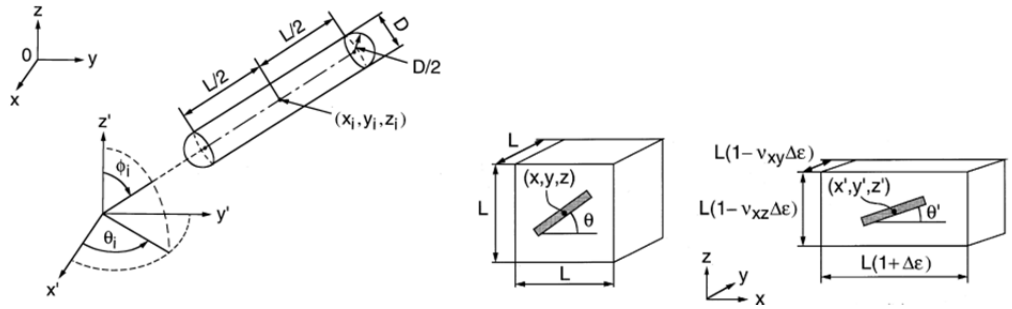

(a) (b) (c)

Figure 59: Physical representation of short fiber during strain reorientation process (a) Short fiber orientation and (b) Short fiber orientation in RVE before strain and (c) Orientation after strain[6]

Representing the short fiber as a line segment and applying an affine transformation, which preserves straight lines and midpoints of line segments, to the RVE and assuming incompressibility of the matrix and strain only along the x-direction, we can express the post-strain RVE dimensions and short fiber midpoint location as

$$\begin{aligned} L'_x &= L_x(1+\Delta\varepsilon), \\ L'_y &= L_y\big(1-\nu_{xy}\Delta\varepsilon\big), \\ L'_z &= L_z(1-\nu_{xz}\Delta\varepsilon), \end{aligned} \tag{17}$$

and

$$\begin{aligned} x' &= x(1+\Delta\varepsilon), \\ \mathrm{y}' &= \mathrm{y}\big(1-\nu_{\mathrm{xy}}\Delta\varepsilon\big), \\ z' &= z(1-\nu_{xz}\Delta\varepsilon), \end{aligned} \tag{18}$$

where v_{ij} is the Poisson’s ratio of a composite defined as

$$\nu_{ij} = \left|\frac{\varepsilon_i}{\varepsilon_j}\right|. \tag{19}$$

To describe the change is orientation due to the applied strain, we can consider the components of length of the short fiber before and after the applied strain, denoted as u and u', respectively. Using the orientation angles defined above, the strain length components can be written as

$$\begin{aligned} u_x &= u \sin\phi \cos\theta, \\ u_y &= u \sin\phi \sin\theta, \\ u_z &= u \cos\phi \end{aligned} \tag{20}$$

prior to applying strain and as

$$\begin{aligned} u'_x &= u' \sin\phi' \cos\theta', \\ u'_y &= u' \sin\phi' \sin\theta', \\ u'_z &= u' \cos\phi' \end{aligned} \tag{21}$$

after application of strain. Applying the affine transformation and combining (17), (18), (20), and (21), we obtain the relations

$$\begin{aligned} 1 + \Delta\varepsilon &= \frac{u' \sin\phi' \cos\theta'}{u \sin\phi \cos\theta}, \\ 1 + \Delta\varepsilon_y &= \frac{u' \sin\phi' \sin\theta'}{u \sin\phi \sin\theta'}, \\ 1 + \Delta\varepsilon_z &= \frac{u' \cos\phi'}{u \cos\phi}. \end{aligned} \tag{22}$$

Combining the relations given in (22), we obtain the reorientation angles (short fiber orientation angles AFTER application of strain $\Delta\varepsilon$),

$$\theta' = \tan^{-1}\left[\frac{(1-\nu_{xy}\Delta\varepsilon)}{(1+\Delta\varepsilon)}\tan\theta\right] \tag{23}$$

and

$$\phi' = \tan^{-1}\left[\frac{(1-\nu_{xy}\Delta\varepsilon)}{(1-\nu_{xz}\Delta\varepsilon)}\frac{\sin\theta}{\sin\phi}\tan\phi\right], \tag{24}$$

The new endpoints of the short fiber can then be calculated using the reorientation angles and the lengths of the fiber relative to the reoriented midpoint of the fiber due to the results of affine transformation.

Finally, though the original work upon which this project is based [65] considered the CNT elements to be soft-core elements (i.e., – inter-penetration of CNT is allowed) to simplify computational costs, it is important to note that this methodology can significantly underestimate the contribution of tunneling resistance given the exponential relationship between separation distance between CNT and resistance, as given in (11). Thus, to compromise between computational costs and accuracy, a pseudo hard-core model is employed in this dissertation. In hard core models, when two CNT are found to penetrate each other, the CNTs are translated slightly so that they are no longer overlapping. Though the concept is simple, the computational costs escalate quickly as the volume fraction increases, especially since the CNT elements are considered to be rigid cylinders and cannot bend around each other. To avoid these computational costs while maintaining the accuracy of separation distance growth as the CNT are reoriented, a pseudo hard-core strategy which initially allows CNTs to penetrate each other, but tracks the GROWTH of separation distance as the model is strained was employed. A connectivity map between all CNT elements recording the initial separation distance was employed. Then, as the model was strained, the separation distance between CNT was taken to be DIFFERENCE in the strained separation distance and the initial separation distance. This difference scheme eliminates the overlap between CNT allowed in the initial population of the RVE.

To verify the ability of the Monte Carlo simulation to account for network breakdown due to fiber repositioning, the above reorientation network was used to reposition fibers in conducting networks for a range of applied virtual strains to track the change in network resistivity. An updated flowchart of the simulation is presented in Figure 61. Unstrained,

conducting CNT-epoxy networks corresponding to 1-5% weight CNT were first generated and the resistance calculated. An applied strain ranging from 0.1% - 1.0% was then applied to the conducting networks and the change in resistance from the unstrained case recalculated. The plot of the normalized change is resistance value vs. applied strain for the different CNT compositions is presented in Figure 60.

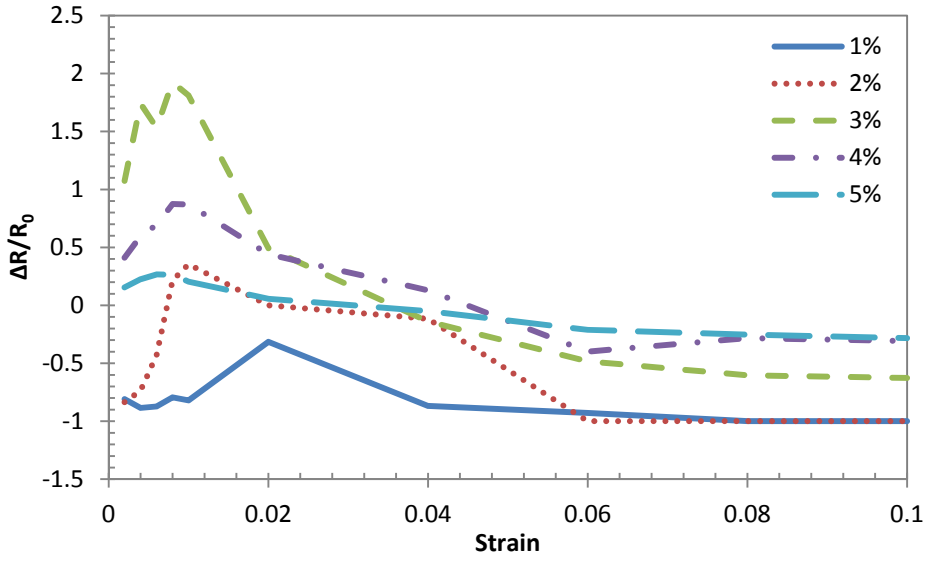

Figure 60: Normalized resistance change vs. applied strain for 1-5% wt CNT composites

From the simulation results, we can see that at small strains up to 1%, there is an initial large increase in resistance as the fibers are initially perturbed and redistributed within the matrix. Beyond 1% strain, the resistance change begins to drop and eventually becomes negative, indicating a net reduction in resistance. This is consistent with the strain reorientation model's effect on alignment [6]. As the strain increases, the fibers become increasing aligned in the X direction, which has been shown experimentally and numerically [69] to reduce the net resistance of the bulk. Also, at high strains, we can see that as the fiber loading increases, the sensitivity of the network to strain reduces, with much smaller normalized resistance changes at 4-5% weight loading.

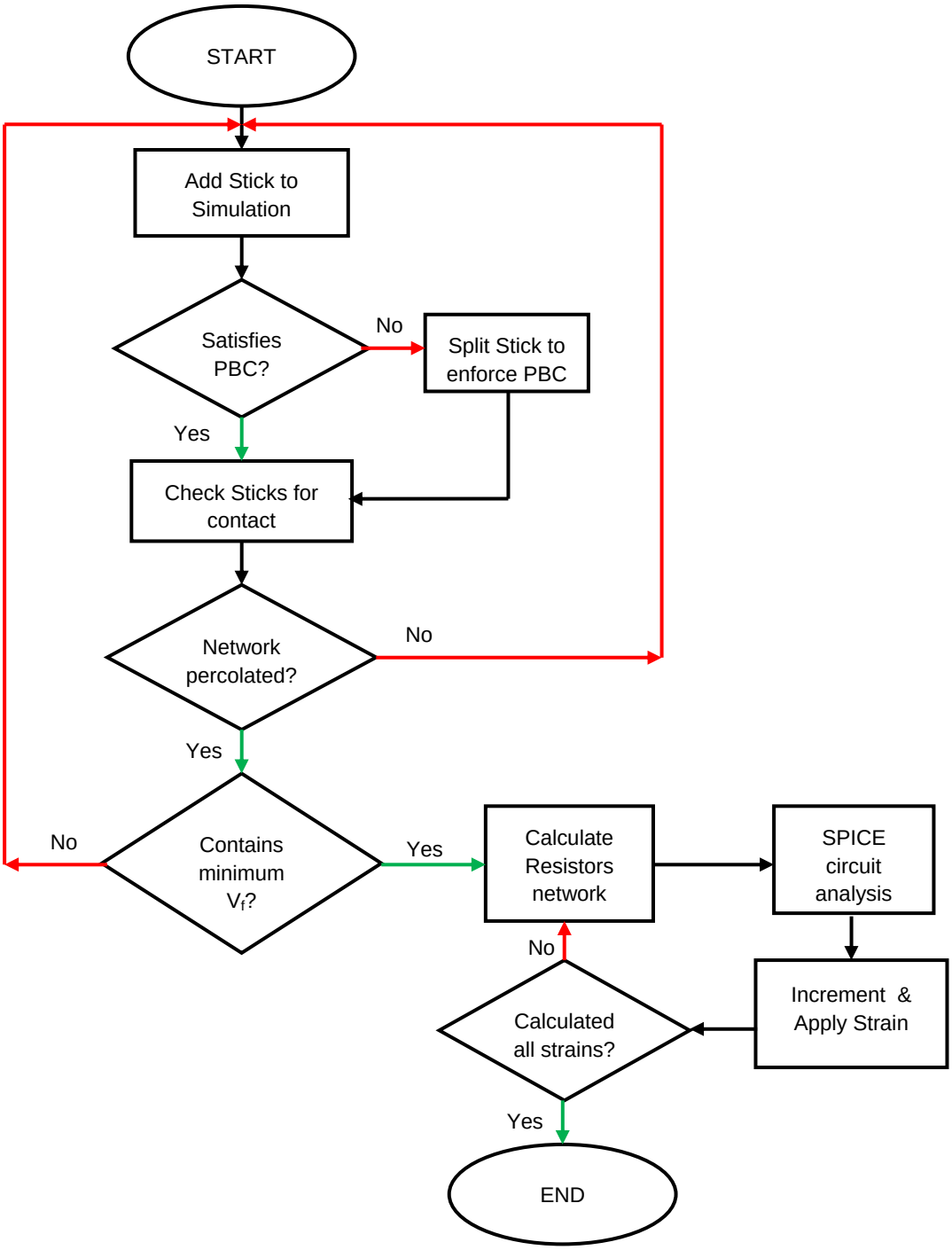

Figure 61: Flow chart of for strain based Monte Carlo CNT-epoxy simulation

5.3.5 Thermal Expansion Based Network Breakdown And Temperature Sensitive Resistivity

Prediction of the thermal expansion coefficient of carbon nanotube reinforced composites was recently explored by Alamusi et al.. In their work, FEM and analytical modeling was compared with experimental results to determine the effects of CNT loading on the coefficient of thermal expansion (CTE) of the short fiber composite. To analytically predict the CTE of the composite, effective medium theory was used in three dimensions for the calculation of the CTE as a weighted average of the individual properties of epoxy and CNT. At varying temperatures, the CTE of the epoxy and CNT constituents were measured (in the case of epoxy) or calculated (in the case of CNT) and used to calculate the corresponding effective CTE of the composite at a given temperature. To facilitate these calculations, the CTE and other relative properties of epoxy and CNT were given by Alamusi et al. in Figure 62 and Table 7, respectively.

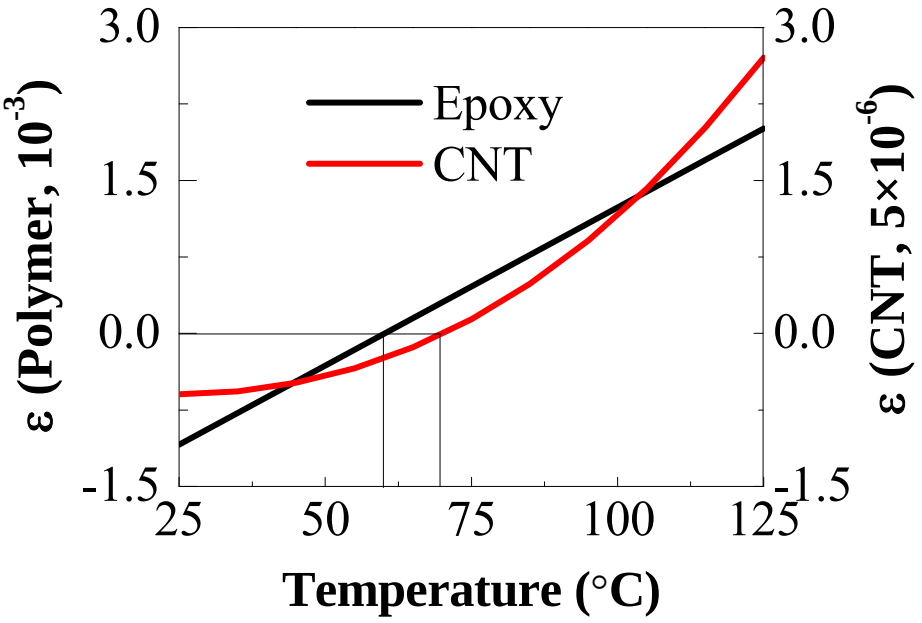

Figure 62: CTE of epoxy and CNT[69]

Table 7: Material properties of epoxy and CNT[69]

Property	***CNT***	***Epoxy***
Density (g/cm^3)	2.1	1.1
Young's Modulus(GPa)	1,000	3.2
Poisson's Ratio	0.1	0.34
Specific Heat (mJ/g-K)	650	1,000
Thermal Conductivity (W/mm-K)	6.7	2×10^{-4}

To facilitate calculation in the simulation, the CTE data was fitted to polynomial trend approximations [70] such that

$$\alpha_m(T) = -0.005 + \frac{0.015}{106-39.0}\ (T - 39), \quad (25)$$

$$\alpha_f(T) = 6.099 \times 10^{-13}\ T^4 - 3.236 \times 10^{-9} T^2 + 5.888 \times 10^{-7} T - 4.5 \times 10^{-5}\ , \quad (26)$$

where α is the CTE, T is the temperature of the composite, and the subscripts m and f refere to matrix and fiber properties, respectively. With these properties known, the effective medium theory can be invoked, where

$$\alpha_c = \frac{V_f E_f \propto_f + V_m E_m \propto_m}{V_f E_f + V_m E_m} \int_0^x (\cos^2\varphi - \upsilon_c \sin^2\varphi) f(\varphi) d\varphi + [(1+\upsilon_m)\alpha_m V_m + (1+\upsilon_f)\alpha_f V_f] \int_0^x f(\varphi) d\varphi \quad (27)$$

where E is t he Young's modulus, v is the Poisson's ratio, the subscript c denotes a property of the composite, φ is the angle of fiber orientation, and $f(\varphi)$ is the fiber distributions function for the class of the fiber orientation. For randomly oriented fibers, the distribution function

$$f(\varphi) = \frac{1}{n}, \quad (28)$$

where n is the number of possible fiber orientations, which is independent of dimension. When the fibers are randomly oriented in three dimensions, the expression for α_c becomes

$$\alpha_c = \frac{1}{2}\left(\frac{V_f E_f \propto_f + V_m E_m \propto_m}{V_f E_f + V_m E_m}(1-\upsilon_c) + (1+\upsilon_m)\alpha_m V_m + (1+\upsilon_f)\alpha_f V_f\right). \quad (29)$$

It can be seen that the Poisson's ratio of the composite, v_c, is needed. Through micromechanics and experimental verification[71], it has been shown that the rule of mixtures can accurately predict the Poisson's ratio of randomly oriented short fiber composites. Thus, v_c is approximated using

$$\upsilon_c = V_f \nu_f + V_m \nu_m. \quad (30)$$

The computed CTE for different weight fractions of CNT over the temperature range of 30°C – 120°C is given below in Figure 63. In their comparison with experimentally measured CTE of MWCNT nanocomposites, Alamusi et al. found that the

micromechanics based model presented above was an accurate prediction of CTE, with less than 15% error across a temperature range of 30-120°C and MWCNT loading range of 1-5% weight.

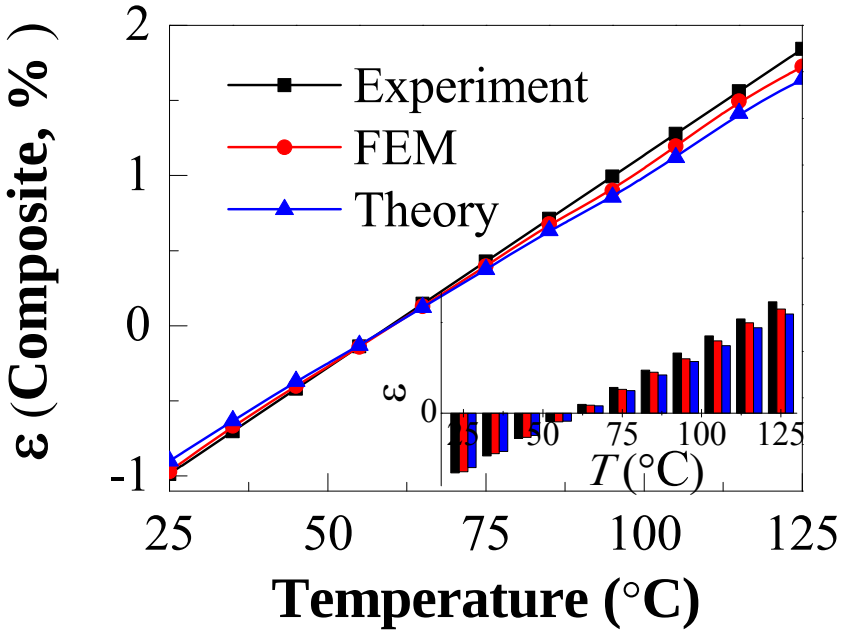

Figure 63: Calculated CTE of CNT-epoxy composite for various CNT loadings[69]

Thus, the proposed Monte Carlo material model is enhanced to include the temperature dependent strain discussed above as a parameter for fiber reorientation. The temperature dependent expansion described in the analytical model presented above is an isotropic volumetric expansion; thus, following the notations given in the strain dependent reorientation section, the fiber positions are updated by the transformation

$$\begin{aligned} x' &= x(1 + \Delta\varepsilon(T)), \\ y' &= y(1 - \Delta\varepsilon(T)), \\ z' &= z(1 - \Delta\varepsilon(T)). \end{aligned} \tag{31}$$

Since volumetric expansion preserves angles within the expanded volume, the orientations of the CNT fibers remains the same while the spacing between the fibers increases. A schematic of this transformation is given in Figure 64. The lengths of the individual CNT fibers are also updated using the thermal expansion information given in Table 1.

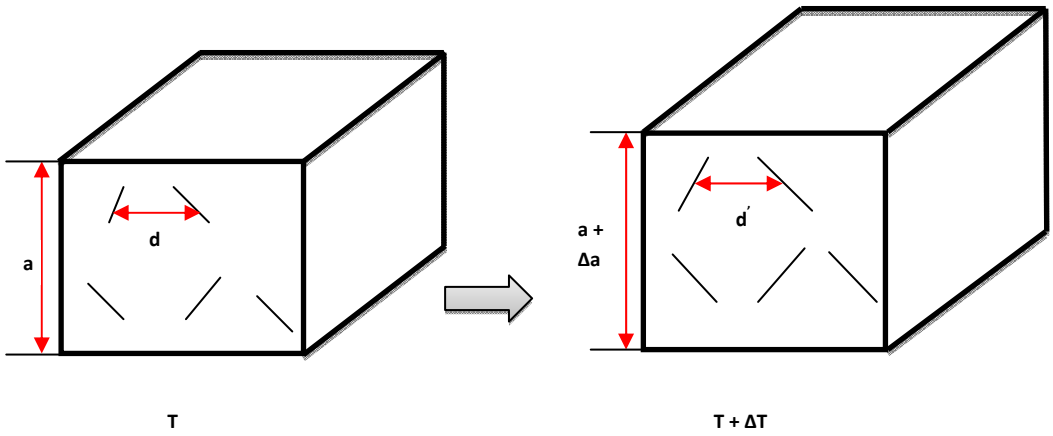

Figure 64: Dimension and CNT spacing changes in RVE due to temperature

5.3.6 Simulation Results Of Temperature Effects On Resistivity

After modification of the model to include thermal strain, numerical simulations were run for CNT weight fractions of 1%, 2%, 3%, 4%, and 5% over the temperature range of 20°C-100°C by 10C intervals. Each simulation was run 10 times and the averaged results are presented in Figure 65 and Figure 66, resistivity and normalized change in resistance, respectively. From the simulation results, if only thermal expansion is considered in the change in resistance network, a distinct change in behavior is expected around 60°C, or the threshold between thermal expansion and contraction as predicted by the analytical model presented above. Below the 60°C, the rate of change of

resistance with temperature is low due to the hard-core CNT conditions set in the model. During thermal contraction, the CNTs are brought closer to each other, reducing the tunneling resistance, but since they cannot penetrate each other their separation distance is limited by the minimum film thickness. Above 60°C, there is no such restriction as the separation distance between CNTs grows. Thus, above the thermal contraction-expansion threshold, the resistance changes quickly. Also, it should be noted that in general, as the CNT loading increases, the sensitivity of CNT-epoxy composite to temperature increases as indicated by the slope above the 60°C threshold. This is believed to be due to larger number of junctions contributing to the network at higher loadings.

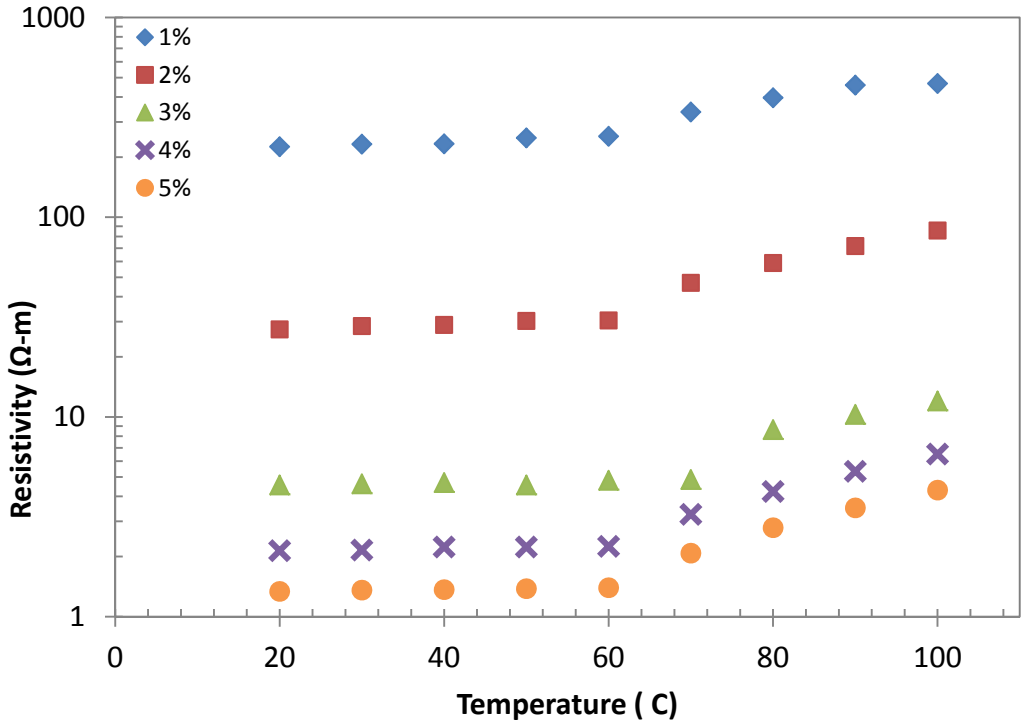

Figure 65: Simulation results of resistivity vs. temperature

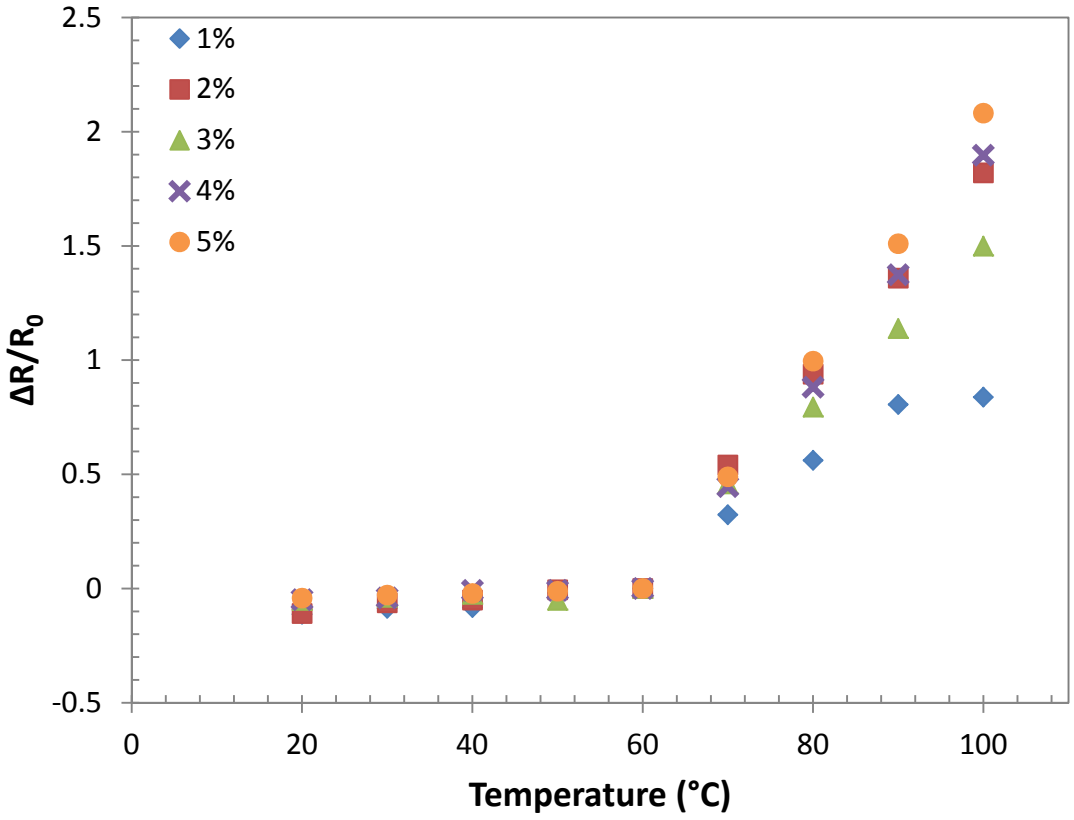

Figure 66: Simulation results of change in resistance vs. temperature

5.4 EXPERIMENTAL VERIFICATION IN CNT-EPOXY NANOCOMPOSITE

To verify the results of the numerical simulation, CNT-epoxy nanocomposite films were fabricated and tested for their bulk resistivity over a range of temperatures. To match the simulation and experimental verification, the simulation parameters were selected to match the physical properties of the selected material system.

5.4.1 Fabrication Of Nanocomposite Specimens

The experimental specimens were fabricated according to the methods described by Hu et al. [42][40] at Chiba University, Japan. Multi-walled CNT (MWCNT) (NT-7, Hodogaya Chemical Co., Ltd) with a nominal outer diameter of 65nm and aspect ratio of

100 was added to epoxy (jER806, Japan Epoxy Resins Co, Ltd.) with amine hardener (Tomaido #245-LP, Fuji Kasei Kogyo Co., Ltd). The properties of the MWCNT are given in Figure 50. First, the epoxy and hardener, with mass ratio 5:3, respectively, were mixed in a planetary mixer (AR-100, THINKY Co., Ltd) at 2000rpm for 10-minutes. Specimens with MWCNT content ranging from 1%-5% weight (%wt), respectively, of the epoxy mixture were fabricated. The MWCNT was added to the mixed epoxy and mixed in the planetary mixture for 10-minutes, with a defoaming interval of 1-minute. The MWCNT-epoxy was then poured into a silicon mold, pressed, and cured in an oven at 80°C for 2-hours. The resulting MWCNT-epoxy films were removed from the mold and cut into 1-cm × 2-cm strips for testing of their electrical resistivity. For the electrical resistivity tests, electrodes were attached to the MWCNT-epoxy films using silver epoxy, as shown in Figure 67.

Table 8: MWCNT Physical Properties

Property	***Value***
Outer Diameter	65nm
Aspect Ratio	> 100
Density (g/cm3)	2.1
Specific Surface Area (m2/g)	28
Carbon Purity (%)	> 99.5

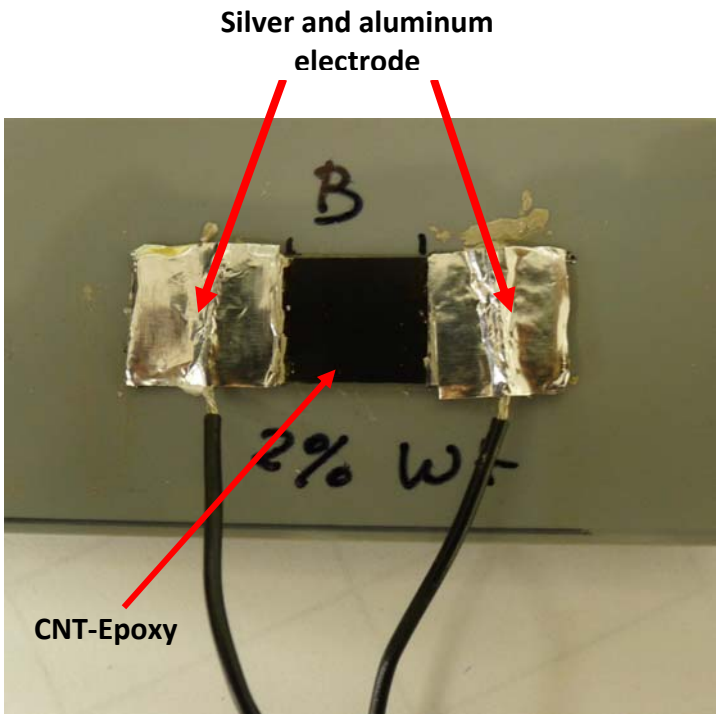

Figure 67: Photo of MWCNT-epoxy Film for Electrical Resistivity Testing

5.4.2 Electrical Resistivity Testing Of MWCNT-Epoxy Films

The MWCNT-epoxy films were tested for their electrical resistivity over the temperature range of 30°C-100°C. After the silver electrodes were formed on the films, the films were placed in a temperature and humidity controlled environmental chamber (ESPEC SH-240) and tested for electrical resistance, *R*, using an LCR meter as the temperature was increased in 10°C steps. A photograph of the experimental set-up is given in Figure 68.

Due to differences in fabrication and curing conditions, the absolute resistivity of a given composition has great variability. Also, though the specimen is known to expand and contract due to thermal expansion, the change in dimensions is negligible compared

to the change in resistance and is ignored here for the purpose of volume resistivity calculation.

Figure 68: Photograph of resistance test set-up for CNT-epoxy film (a) environmental chamber and LCR meter and (b) samples in interior of environmental chamber

5.4.3 Results

The average absolute calculated resistivity values for the tested epoxy composite films vs. temperature for CNT compositions of 1-5% composite weight are presented below in Figure 69. As described in the above section, the absolute resistivity of the samples was calculated by normalizing the measured sample resistance by the sample dimensions. The results presented are the average calculated resistivities for each sample composition.

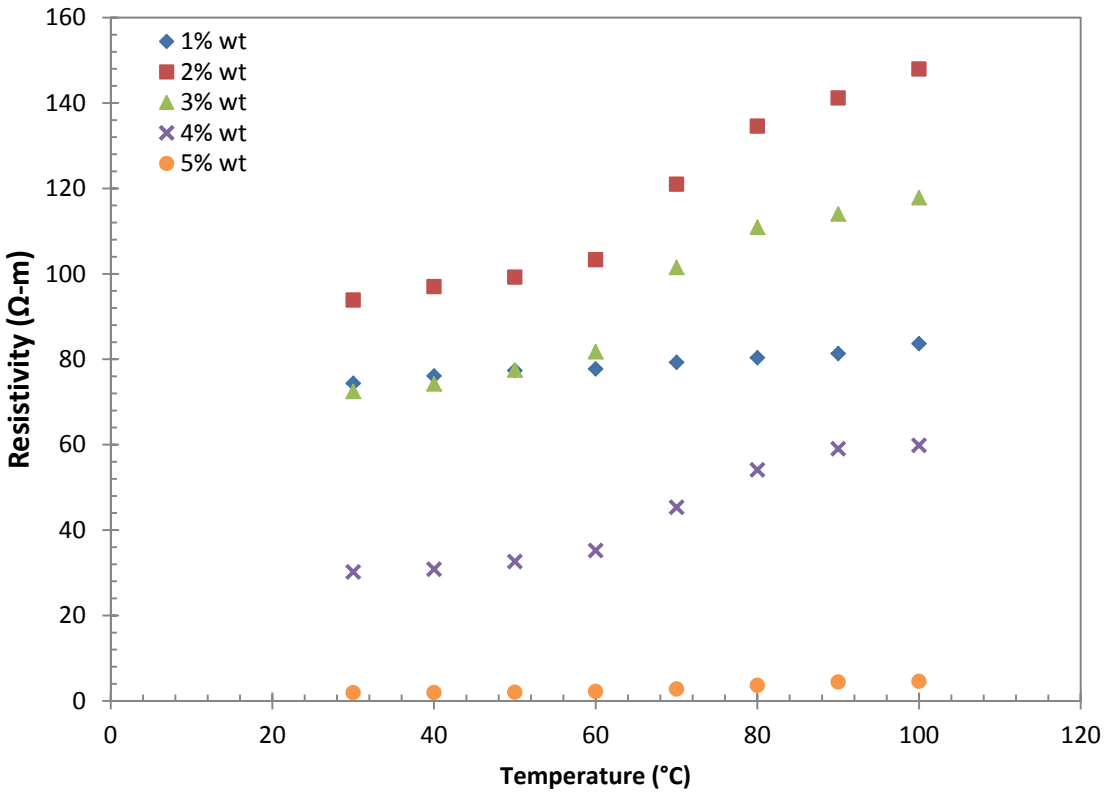

Figure 69: Average absolute resistivity of epoxy-CNT films vs. temperature

Though all composition show the same general trend with increase of temperature, it is difficult to perform a direct comparison of the composite resistivity's sensitivity to temperature using the absolute calculated resistivity. To better analyze the sensitivity, the normalized percent change of resistivity was calculated as

$$\Delta R_{\%} = \frac{R - R_{60^\circ}}{R_{60^\circ}}, \tag{32}$$

where R_{60} denotes the resistivity of the sample at 60°C. The reasoning for normalization by the measured resistivity at 60°C is discussed in the following section. The normalized resistivity change results for the CNT-epoxy films of composition 1-5% weight CNT are presented below in Figure 70.

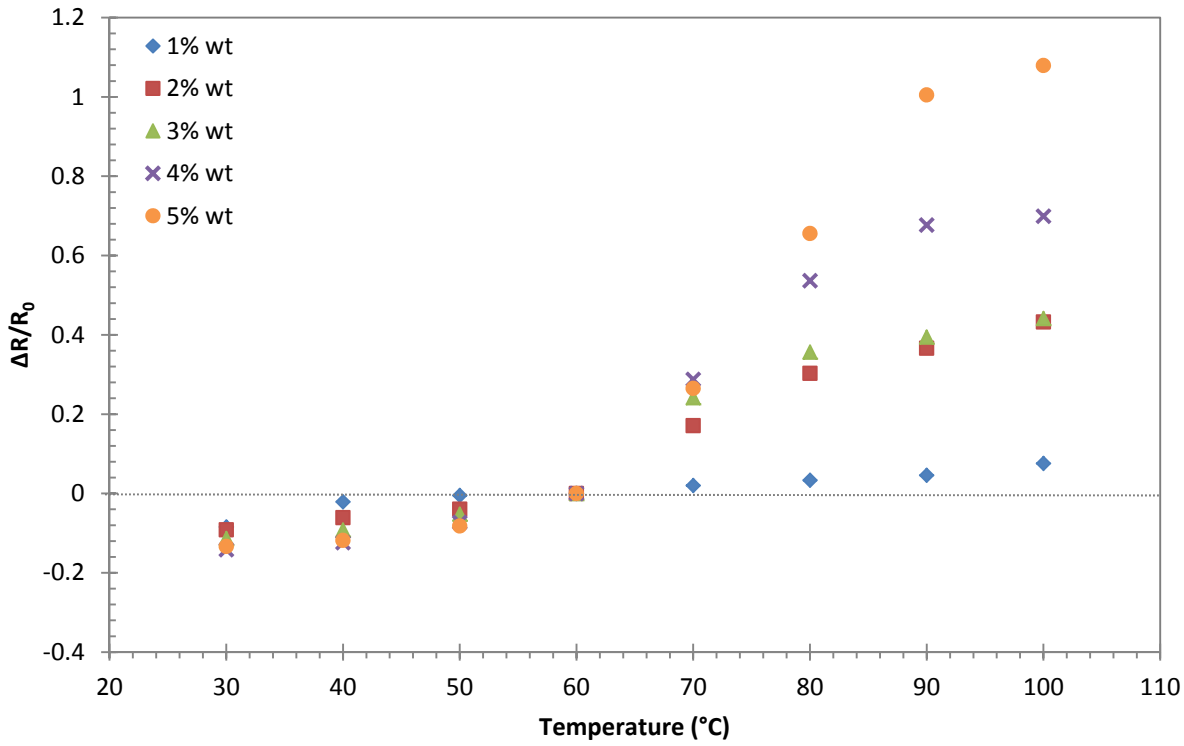

Figure 70: Normalized change of resistivity of CNT-epoxy films vs. temperature

5.5 Discussion

From the experimental results presented above, it can be seen that CNT-epoxy short fiber composites are indeed highly sensitive to temperature. First, the experimental results in Figure 69 verify the longstanding observation that increased CNT reinforcement content generally results in lower composite resistivity. Though the samples with the lowest CNT composition, that is 1% by composite weight, had a mid-level resistivity, it can be understood by the difficulties in maintaining a truly random fiber orientation. During the fabrication process, the viscosity of the uncured matrix is strong affected by the addition of the high aspect ratio CNT powder. At low CNT loadings, the uncured epoxy has low viscosity and good flowability, resulting is an easily

spreadable matrix during the film formation process. However, this same flowability can result in increased fiber alignment during the pressing process used to form the composite film. It has been previously shown by experiment and simulation that fiber alignment (which can often be introduced through pressing, injection, or extrusion processes) results in a lowered electrical composite resistivity.

However, of greater interest is the piece-wise behavior of resistivity vs. temperature for samples of all compositions. Though there is an overall increase in resistivity as the temperature increases, the behavior of the composite can be broken into two linear regions – a region of relatively low rate of resistivity change with temperature at low temperatures (i.e., – below 60°C) and a region of increased rate of resistivity change with temperature at high temperatures (i.e., – above 60°C). These two regions are observed graphically as a change in slope in the resistivity vs. temperature plots. The significance of the 60°C threshold lies in the thermal expansion analysis of this exact CNT-epoxy material system performed by Alamusi et al. [69], in which thermal expansion of the composite was examined through changes in temperature through experiment, FEM, and micro-mechanical analysis. In their investigation, Alamusi et al. concluded that the CNT-epoxy system studied incurred an important change in thermal expansion behavior at approximately the 62°C threshold – below the temperature threshold, the composite possessed a negative thermal expansion rate (i.e., – a net contraction of dimensions with small increases in temperature); above the temperature threshold, the composite posses a positive thermal expansion rate (i.e., – a net expansion of dimensions with small increases in temperature). Thus, in the results presented here, the observation of two regions of resistivity behavior changing at the 60°C threshold

lends support to the hypothesis that thermal expansion plays a dominate role in the conductive network breakdown which results in changes in the composite's electrical resistance behavior.

Extending Alamusi et al.'s conclusions, it can be projected that at high temperatures above the transition threshold the composite undergoes a net volumetric expansion, pulling the conductive CNT fibers apart and reducing the number of parallel conductive pathways through which current can flow. At temperatures below the transition threshold, the composite contracts, pushing the CNT fibers closer together and reducing the tunneling resistance (the resistance incurred as electrons must "tunnel" through the insulating matrix to move between conductive fibers), which is a function of the conducting fibers' separation distance. The result is a conductive network break down as the fibers are gradually pulled apart and, eventually, separated to the point where electrons can no longer tunnel from fiber to fiber. However, it should be remembered that the CNT fibers cannot be pushed into each other and that the thin layer of insulating matrix cannot be completely eliminated. Thus, at low temperatures, the rate of change of resistivity is reduced since physical restrictions limit the extent to which the inter-fiber tunneling resistance can be reduced.

Additionally, normalization of the resistivity calculations by the 60°C threshold resistivity allows us to directly compare the composite sensitivity to temperature. After the normalization shown in Figure 70, we can see that as the composite CNT loading is increased at temperatures above the transition threshold, the sensitivity of the composite resistivity to temperature is increased; that is, as more CNT is added to the composite, the slope of the normalized resistivity vs. temperature graph increases. Though the

normalized resistivity vs. temperature graph appears linear at first, at high temperatures (above 100°C), the rate of change with temperature slows down, likely due to changes in mechanical properties as we approach the glass transition temperature of epoxy (approximately 120°C). Also, below the transition threshold temperature, there is a lack of distinct differences in temperature sensitivity between CNT compositions. This further supports the role of thermal expansion, as described above, in the change in electrical transport properties. As discussed above, since the physical restraints of the fiber-matrix arrangement limit how closely the fibers can be driven toward each other, a lack of temperature sensitivity (due to limited thermal contraction capacity) is to be expected and is verified in the results presented. There is no distinguishable difference in temperature sensitivity between composite compositions below the transition threshold.

Chapter 6 Conclusions and Directions for Future Work

This dissertation presented the work conducted on two projects relating to multi-functional carbon reinforced polymer composites. First, the work done on the development of a CF based self-heating fiberglass laminate structural system for wind turbine blade de-icing and the supporting control strategy was presented. Both laboratory and field testing showed that the proposed material system and control methods are effective in providing de-icing and anti-icing functionality to fiberglass-epoxy structures. Second, numerical simulation and experimental work on a temperature sensitive, piezoresistive CNF-epoxy composite film was presented. The work shows that use of a thermal expansion model combined with a Monte Carlo based simulation using junction resistance between fibers to generate resistor network circuits is effective in predicting the effect of temperature on electrical resistivity of the composite.

The results of the two projects demonstrate the enormous potential of carbon based polymer composites to serve as highly functional structural materials. In the case of the heated laminate system, the proposed application can potentially reduce the cost of wind energy by increasing production time in cold, humid climates, such as the North Sea and mountainous areas of central China, where demand for wind energy is high. Furthermore, beyond the proposed wind turbine application, the self-heating laminate system can be used for a number of other applications, including heated structural paneling and flooring. Though a fiberglass-epoxy base was used for the laminate in this dissertation, the material system can easily be tailored to the needs of the application and the supporting control structure would remain the same.

In the case of piezoresistive CNF-epoxy film, there is an increasing demand for high performance sensors which can be miniaturized or completely integrated into the structure. The CNF-epoxy system provides the advantages of conformability to any shape, small footprint, and high sensitivity to strain and temperature. As a short fiber reinforced composite, the film itself is a structural material which can be molded to form any number of self-sensing components. With the developed Monte Carlo model, material properties and manufacturing details, such as fiber orientation, can be easily combined to develop manufacturing processes tailored to the needs of the application.

6.1 CARBON FIBER BASED WIND TURBINE BLADE DEICING SYSTEM

Extensive laboratory testing of the proposed CF based fiberglass-epoxy laminate system strongly affirm its potential as a self-heating structural material. The results indicate that the CF based laminate is effective in providing a highly spatially targeted, fast responding heating capacity sufficient for surface de-icing applications. Investigation of the controller performance indicates that compared to traditional on-off control, upon which most commercial heating controllers are based, a proposed wind speed based power regulating fuzzy logic controller can be more effective at ice removal as well as be significantly more power efficient for the maintenance of the same laminate surface temperature. Field testing of a mock-up wind turbine with three blades installed with the self-heating laminate system and power regulation instrumentation support the laboratory results and provide a proof of concept for application in real world conditions.

Though modern wind turbine systems often have their own weather stations, these measurements are localized and cannot give information about larger weather systems

that may be moving toward the field site. As introduced in Section 3.6, weather forecast data can be easily incorporated into the proposed fuzzy logic controller to provide additional markers for the potential of icing events. Though this weather forecast functionality was developed in the controller system used in the UAA site test, due to the relatively dry climate of the Anchorage area, the dew point based icing prediction was not triggered during the testing time. Further work should be conducted to further develop the advanced use of weather forecasting data to provide anti-icing functionalities to the proposed CF based laminate structural system.

Results from the tensile material properties tests of samples with varying degrees of thermal cycling indicate that over 100 thermal cycles, there is only limited degradation of mechanical properties. Though there was a slight decrease seen in the fracture strain of the laminates, the fracture stress and elastic modulus saw no significant change as thermal cycling increased. Furthermore, taking into account the frequency of icing events and blade replacement in actual operation, the range of thermal cycling explored in this dissertation represents the typical lifetime of a wind turbine blade, over which the slight degradation would be spread. It is believed that with proper care in designing the wind turbine blade with regards to the fracture strain that no significant changes in operation life would be seen with the incorporation of the proposed self-heating composite.

6.2 TEMPERATURE DEPENDENT MONTE CARLO NANOCOMPOSITE RESISTIVITY MODEL

Using both analytical models at the microstructure scale and experimental measurement, the thermal expansion based temperature dependence of electrical resistivity of CNT-epoxy film composites was demonstrated. However, it should be kept in mind that the level temperature sensitivity depends on the application in mind. For example, if the intended application is in-situ temperature measurement, then a high sensitivity is desired so that a greater resolution of temperature to voltage can be achieved. However, in many structural applications, the desired sensing parameter is strain, which has now shown to be coupled with temperature effects. Thus, in the case of desired strain measurement applications, a low temperature sensitivity is desired so that the temperature based ER change can be decoupled.

Rather than depend on experimental data to produce needed calibration information and relative sensitivity comparisons, the developed numerical model can simplify material design by allowing manipulation of many parameters, including aspect ratio and fiber alignment, to be explored to shorten the time consuming and expensive experimental verification. Thus, a second major contribution of this work is the development of an extendable design tool for the electrical resistance property design of high aspect ratio fiber filled composites.

6.3 FUTURE WORK

In the case of mechanical property change with increasing thermal cycling, more work needs to be done to more completely understand the full extent of the change that

the self-heating process may have on the mechanical properties of the material. In this work, the uniaxial tensile properties were examined, but the shear behavior should be examined due to the properties of laminate composites. Interlayer bonding between the fiber reinforcement layers is matrix dominated and much weaker than the tensile strength, where loads are mainly supported by strong, stiff fibers. Also, due to the orientation of fibers in laminate lay-up, laminate properties are highly anisotropic. Due to both these characteristics of laminates, further study of the laminate mechanical properties is needed through bending tests and multiaxial loading tests to understand the interlaminar shear and orthotropic properties. Additionally, repeated testing with higher levels of thermal cycling is needed to extend the findings to longer operation life of the wind turbine blade.

Though the Monte Carlo simulation of the resistance change of CNT-epoxy composite due to temperature was highly successful in capturing the real behavior seen in the lab experiment conducted in this dissertation, it should be noted that vastly different resistance-temperature relationships have been seen in other CNT fiber reinforced systems. Other research has seen resistivity DECREASE exponentially with increasing composite temperature in carbon nano-filler reinforced composites with matrix systems such as cement [28][5] and polyester. This behavior cannot be described by the thermal expansion model given here and experimental measurements seem to indicate and activation energy-like behavior. Thus, more work is needed to investigate the possible effects of matrix activation energy or band gap properties to determine the threshold between the thermal expansion dominated behavior seen in this dissertation (resulting in a positive thermal coefficient for resistance) and the exponential behavior seen in other material systems (resulting in an exponential, negative thermal coefficient).

References

[1] M. Durstewitz, H. Dobesch, G. Kury, T. Laakso, G. Ronsten, and K. Santti., "European experience with wind turbines in icing conditions," in *European Wind Energy Conference and Exhibition*, London, 2004, pp. 1-6.

[2] O. Parent and A Ilinca, "Anti-icing and de-icing techniques for wind turbines: Critical review," *Cold Regions Science and Technology*, vol. 65, pp. 88-96, 2011.

[3] Deborah D.L. Chung, *Composite Materials: Science and Applications*, Brian Derby, Ed. London: Springer, 2003.

[4] X. Luo, A. Morrin, A. Killard, and M. Smyth, "Application of nanoparticles in electrochemical sensors and biosensors," *Electroanalysis*, pp. 319-326, 2006.

[5] D.D.L. Chung, "Electrical conduction behavior of cement-matrix composites," *Journal of Materials Engineering and Performance*, vol. II, no. 11, pp. 194-205, April 2002.

[6] M. Taya, W.J. Kim, and K. Ono, "Piezoresistivity of a short fiber/elastomer matrix composite," *Mechanics of Materials*, vol. 28, pp. 53-59, 1998.

[7] Sihai Wen and D.D.L. Chung, "Carbon fiber-reinforced cement as a thermistor," *Cement and Concrete Research*, no. 29, pp. 961-965, 1999.

[8] T.M. Chrisp, G. Starrs, W.J. McCarter, E. Rouchotas, and J. Blewett, "Temperature-conductivity relationships for concrete: An activation energy approach," *Journal of Materials Science Letters*, no. 20, pp. 1085-1087, 2001.

[9] M.R. Kessler, N.R. Sottos, and S.R. White, "Self-healing structural composite materials," *Composites Part A: Applied Science and Manufacturing*, vol. 34, no. 3, pp. 743-753, August 2003.

[10] S.R. White, N.R. Sottos, P.H. Geubelle, J.S. Moore, M.R. Kessler, S.R. Sriram, E.N. Brown, and S. Viswanathan, "Autonomic healing of polymer composites," *Nature*, vol. 409, pp. 794-797, February 2001.

[11] J. Gou, S. O'Braint, H. Gu, and G. Song, "Damping augmentation of nanocomposites using carbon nanofiber paper," *Journal of Nanomaterials*, vol. 2006, pp. 1-7, 2006.

[12] R.H. Baughman, C. Cui, A.A. Zakhidov, Z. Iqbal, J.N. Barisci, G.M. Spinks, G.G. Wallace, A. Mazzoldi, D. De Rossi, A.G. Rinzler, O. Jaschinksi, S. Roth, and M. Kertesz, "Carbon nanotube actuators," *Science*, pp. 1340-1346, 1999.

[13] S. Yehia, C. Tuan, D. Ferndon, and B. Chen, "Conductive concrete overlay for bridge de-icing: Mixture proportioning, optimization, and properties," *American Concrete Institute Materials Journal*, vol. 97, no. 2, pp. 172-181, 2000.

[14] J.O. Berghaus, J.G. Legoux, C. Moreau, F. Tarasi, and T. Chraska, "Mechanical and thermal transport properties of suspension thermal-sprayed alumina-zirconia composite coatings," *Journal of Thermal Spray Technology*, vol. 17, no. 1, pp. 91-104, March 2008.

[15] A.G. Every, Y. Tzou, D.P.H. Hasselman, and R. Raj, "The effect of particle size on the thermal conductivity of ZnS/diamond composites," *Acta Metallurgica Materia*, vol. 40, no. 1, pp. 123-129, 1992.

[16] Kin-Tak Lau and David Hui, "The revolutionary creation of new advanced materials - carbon nanotube composites," *Composites: Part B*, vol. 33, pp. 263-2777, 2002.

[17] M.S. Kim, H.K. Kim, S.W. Byun, S.H. Jeong, Y.K. Hong, J.S. Joo, K.T. Song, J.K Kim, C.J. Lee, and J.Y. Lee."PET fabric/polypryrrole composite with high electrical conductivity for EMI shielding," *Synthetic Metals*, vol. 126, no. 2-3, pp. 233-239, February 2002.

[18] B.C.K. Tee, Chao, Allen, Ranulfo Wang, and Zhenan Bao, "An electrically and mechanically self-healing composite with pressure- and flexion sensitive properties for electronic skin applications," *Nature Nanotechnology*, vol. 7, pp. 825-832, November 2012.

[19] V.C. Li, Y.M. Lim, and Y.W. Chan, "Feasibility study of a pasive smart self-healing cementitious composite," *Composites Part B: Engineering*, vol. 29, no. 6, pp. 819-827, November 1998.

[20] S. Yehia and C. Tuan, "Conductive concrete overlay for bridge deck de-icing," *American Concrete Institute Materials Journal*, vol. 96, no. 3, pp. 382-390, 1999.

[21] H.A. Sodano, G. Park, and D. Inman, "An investigation into the performance of macro-fiber composites for sensing and structural vibration applications," *Mechanical Systems and Signal Processing*, vol. 18, no. 3, pp. 683-697, May 2004.

[22] G. Song, B. Kelly, and B.N. Agrawal, "Active position control of a shape memory alloy wire actuated composite beam," *Smart Materials and Structures*, vol. 9, no. 5, pp. 711-716, 2000.

[23] J.G. Boyd and D.C. Lagoudas, "Thermomechanical response of shape memory composites," *Journal of Intelligent Material Systems and Structures*, vol. 5, no. 3, pp. 333-346, May 1994.

[24] X. Wang, Y. Wang, and Z. Jin, "Electrical conductivity characterization and variation of carbon fiber reinforced cement composite," *Journal of Materials Science*, vol. 37, pp. 223-227, 2002.

[25] S. Wang, X. Shui, X. Fu, and D.D.L. Chung, "Early fatigue damage in carbon-fiber composites observed by electrical resistance measurement," *Journal of Materials Science*, vol. 33, pp. 3875-3884, 1998.

[26] P.E. Irving and C. Thiagarajan, "Fatigue damage characterization in carbon fiber composite materials using an electrical potential technique," *Smart Materials and Structurs*, vol. 7, pp. 456-466, 1998.

[27] Ingo Weber and Peter Schwarz, "Monitoring bending fatigue in carbon-fiber/epoxy composite strands: a comparison between mechanical and resistance techniques," *Composites Science and Technology*, vol. 61, pp. 849-853, 2001.

[28] D.D.L. Chung, "Cement reinforced with short carbon fibers: a multifunctional material," *Composites: Part B*, no. 31, pp. 511-526, 2000.

[29] H. Li, H. Xiao, and J. Ou, "Effect of compressive strain on electrical resistivity of carbon black-filled cement-based composites," *Cement & Concrete Composites*, vol. 28, pp. 824-828, 2006.

[30] M. Sun, X. My, Z. Wang, Z. Hou, and Z. Li, "Experimental studies on the indoor electrical floor heating system with carbon black mortar slabs," *Energy and Buildings*, vol. 40, pp. 1094-1100, 2008.

[31] I. Kang, M.J. Schulz, J.H. Kim, V. Shanov, and D. Shi, "A carbon nanotube strain sensor for structural health monitoring," *Smart Materials and Structures*, pp. 737-748, 2006.

[32] Morinobu Endo, Takuaya Hayashi, Yoong Ahm Kim, Mauricio Terrones, and Mildred S. Dresselhau, "Applications of carbon nanotubes in the twenty-first century," *Philosophical Transaction of the Royal Society of London*, vol. 362, pp. 2223-2238, 2004.

[33] Inpil Kang, Yun Yeo Heung, Yun Yeo, Jay H. Kim, Jong Won, Lee, Ramanand Gollapudi, Srivinivas Subramaniam, Suhasini Narasimhadevara, Douglas Hurd, Goutham R. Kirikera, Vesselin Shanov, Mark J. Schulz, Donglu Shi, Jim Boerio, and Shankar Mall, "Introduction to carbon nanotube and nanofiber smart materials," *Composites: Part B*, vol. 37, pp. 382-394, 2006.

[34] T Durkop, S.A. Getty, Enrique Cobas, and M.S. Fuhrer, "Extraordinary mobility in semiconducting carbon nanotubes," *Nano Letters*, vol. 4, no. 1, pp. 35-39, 2004.

[35] H. Deng, T. Skipa, E. Bilotti, R. Zhang, D. Lellinger, L. Mezzo, Q. Fu,I. Alig, and T. Peijs, Ton, "Preparation of high-performance conductive polymer fibers through morphological control of networks formed by nanofillers," *Advanced Functional Materials*, vol. 20, pp. 1424-1432, 2010.

[36] M. Grujicic, G. Cao, and W.N. Roy, "A computational analysis of the percolation threshold and the electrical conductivity of carbon nanotube filled polymeric materials," *Journal of Materials Science*, vol. 39, pp. 4441-4449, 2004.

[37] Wolfgang Bauhofer and Josef Z. Kovacs, "A review and analysis of electrical percolation in carbon nanotube polymer composites," *Composites Science and Technology*, vol. 69, pp. 1486-1498, 2009.

[38] T. Kuilla, S. Bhadra, D. Yao, N.H. Kim, and S. Lee, J.H. Bose, "Recent advances in graphene baesd polymer composites," *Progress in Polymer Science*, vol. 35, no. 11, pp. 1350-1375, November 2010.

[39] N. Hu, Y. Karube, M. Arai, T. Watanabe, C. Yan, Y. Li, Y. Liu, and H. Fukunaga, H."Investigation on sensitivity of a polymer/carbon nanotube composite strain sensor," *Carbon*, vol. 48, no. 3, pp. 680-687, March 2010.

[40] N. Hu, Y. Karube, C. Yan, Z. Masuda, and H Fukunaga, "Tunneling effect in a polymer/carbon nanotube nanocomposite strain sensor," *Acta Materialia*, vol. 56, no. 13, pp. 2929-2936, August 2008.

[41] Ying, Qiu, XinMing Li, Fan Yang, Xi-Shu Wang, and Yajun Yin, "Ultra-high sensitivity of super carbon-nanotube based mass and strain sensors," *Nanotechnology*, vol. 19, pp. 1-8, 2008.

[42] N. Hu, Z. Masuda, G. Yamamoto, H. Fukunaga, T. Hashida, J. Qiu, "Effect of fabrication process on electrical properties of polymer/multi-wall carbon nanotube nanocomposites," *Composites: Part A*, vol. 39, no. 5, pp. 893-903, May 2008.

[43] D. Gao, M. Sturm, and Y. L. Mo, "Electrical resistance of carbon-nanofiber concrete," *Smart Materials and Structures*, vol. 18, no. 9, 2009.

[44] S. Bae, H. Kim, Y. Lee, X. Xu, J.S. Park, Y. Zhen, J. Balakrishnan, T. Lei, H. Kim, Y. Song, Y.J. Kim, K.S. Kim, B. Ozyilmaz, J.H. An, B.H. Hong, and S. Iijima, "Roll-to-roll production of 30-inch graphene films for transparent electrodes," *Nature Nanotechnology*, vol. 5, pp. 574-578, August 2010.

[45] Chen Wei, Ajit Roy, and Tia Tolle, "Multifunctional chemical vapor sensors of aligned carbon nanotubes and polymer composites," *Journal of the American Chemical Society*, vol. 128, pp. 1412-1413, 2006.

[46] N. Sinha, J. Ma, and J. Yeow, "Carbon nanotube based sensors," *Journal of Nanoscience and Nanotechnology*, vol. 6, pp. 573-590, 2006.

[47] A. Ilinca, "Analysis and mitigation of icing effects on wind turbines," in *Wind Turbines*, I.

Al-Bahadly, Ed.: Intech-Open, 2011, ch. 8, pp. 177-214.

[48] C. Hochart, G. Fortin, and J. Perron, "Wind turbine performance under icing conditions," *Wind Energy*, vol. 2, pp. 319-333, 2008.

[49] H. Holttinen, G. Ronsten, L. Tallhaug, P. Lundsager, R. Horbaty, I. Baring-Gould, A. Lacroix, E. Peltola, and T. Laakso, "The state-of-the-art of wind turbines in icing and cold climates," in *Global Windpower Conference and Exhibition*, Paris, France, 2002, pp. 1-5.

[50] L. Battisti, R. Fedrizzi, A. Brighenti, and T. Laakso, "Sea ice and icing risk for offshore wind turbines," in *OWEMES*, Citavecchia, Italy, 2006, pp. 1-10.

[51] T. Laakso, H. Holttinen, G. Ronsten, L. Tallhaug, R. Horbaty, I. Baring-Gould, A. Lacroix, E. Peltola, and B. Tammelin, B."State-of-the-art of wind energy in cold climates," International Energy Agency, Research Review 2003.

[52] H. Seifert, A. Westerhellweg, and J. Kroning, "Risk analysis of ice throw from wind turbine blades," in *BOREAS VI*, Pyha, Finland, 2003, pp. 1-18.

[53] H. Seifert, "Technical requirements for rotor blades operating in cold climate," in *BOREAS VI*, Finland, 2003.

[54] E. Peltola, M. Marjeniemi, H. Stiesdal, and J. Jarvela, "An ice prevention system for the wind turbine blades," in *European Wind Energy Conference*, Nice, France, 1999, pp. 1034-1037.

[55] L Battisti, P. Baggio, and R. Fedrizzi, "Warm-air intermittent de-icing system for wind turbines," *Wind Engineering*, vol. 30, no. 5, pp. 361-374, 2006.

[56] C. Mayer, A. Ilinca, G. Fortin, and J. Perron, "Wind tunnel study of of electro-thermal de-cing of wind turbine blades," *International Journal of Offshore and Polar Engineering*, pp. 1-7, 2007.

[57] Kelly Aerospace. (2012, November) Kelly Aerospace Thermal Systems. [Online]. http://www.kellyaerospace.com/wind_turbine_deice.html

[58] G.A. Owens and S.E. Schofield, "Thermal cycling and mechanical properties of carbon fibre fabric reinforced PMR-15 polyimide laminates," *Composites Science and Technology*, vol. 33, pp. 177-190, 1988.

[59] B.C. Ray, "Study of the influence of thermal shock on the interfacial damage in thermosetting matrix aramid fiber composites," *Journal of Material Science Letters*, vol. 22, pp. 201-202, 2003.

[60] B.C. Ray, "Thermal shock and thermal fatigue on delamination of glass fiber reinforced

polymeric composites," *Journal of Reinforced Plastics and Composites*, vol. 24, no. 1, pp. 1-14, 2005.

[61] N.L. Hancox, "Thermal effects on polymer matrix composites: Part 1. Thermal cycling," *Materials and Design*, vol. 19, pp. 58-91, 1998.

[62] "Standard test method for tensile properties of polymer matrix composite materials," ASTM, Standards 2008.

[63] Caithness Wind Farm Information Forum. (2007, September) 2005 Wind Turbine Accident Data to December 31st 2005. [Online]. http://www.caithnesswindfarms.co.uk

[64] M.M. Khan, M.T. Iqbal, and F. Khan, "Reliability analysis of a horizontal axis wind turbine," in *IEEE 14tg NECEC Conference*, Newfoundland, Canada, 2004.

[65] Y. Yu, G. Song, and L. Sun, "Determinant Role of Tunneling Resistance in Electrical Conductivity of Polymer Composites Reinforced by Well Dispersed Carbon Nanotubes," *Journal of Applied Physics*, pp. 108-113, 2010.

[66] J.G. Simmons, "Generalized Formula for the Electric Tunnel Effect between Similar Electrodes Separated by a Thin Insulating Film," *Journal of Applied Physics*, pp. 1793-1803, 1963.

[67] N. Hu, M. Zen, C. Yan, G. Yamamoto, H. Fukunaga, and T. Hashida, "The electrical properties of polymer nanocomposites with carbon nanotube fillers," *Nanotechnology*, vol. 19, no. 5, pp. 893-903, May 2008.

[68] M. Taya, *Electronic Composites*. New York, USA: Cambridge University Press, 2005.

[69] Alamusi, "Prediction of CTE," *Nanoscale Research*, 2013.

[70] M. Schmidt and H. Lipson, "Distilling free-form natural laws from experimental data," *Science*, vol. 324, no. 5923, pp. 81-85, 2009.

[71] J.C. Halpin and J.L. Kardos, "The Halpin-Tsai equations: a review," *Polymer Engineering and Science*, vol. 16, no. 5, pp. 344-352, May 1976.

[72] D. Williams, N. Williams, and Y. Cao, "Road salt contamination of ground water in major metropolitan area and development of a biological index to monitor its impact," *Water Research*, vol. 34, no. 1, pp. 127-138, 2000.

[73] D.D.L Chung, "Self-heating structural materials," *Smart Materials and Structures*, vol. 13, pp. 562-565, 2004.

[74] C. Tuan, "Electrical resistance heating of conductive concrete containing steel fibers and

shavings," *American Concrete Institute Materials Journal*, vol. 101, no. 1, pp. 65-70, 2004.

[75] S. Yehia and C. Tuan, "Current Events," *Roads and Bridges*, vol. 46, no. 10, pp. 32-35, October 2008.

[76] S. Yehia, "No-stick surface," *Roads and Bridges*, vol. 42, no. 4, pp. 26-28, April 2004.

[77] W. J. McCarter, G. Starrs, T. M. Chrisp, and P.F. G. Banfill, "Activation energy and conduction in carbon fiber reinforced cement matrices," *Journal of Material Science*, vol. 42, pp. 2200-2203, 2007.

[78] G. Yin, N. Karube, Y. Liu, Y. Li, and H. Fukunaga, "A carbon nanotube/polymer strain sensor with linear and anti-symmetric piezoresistivity," *Journal of Composite Materials*, vol. 45, no. 12, pp. 1315-1323, 2011.

[79] W.S. Bao, S.A. Meguid, Z.H. Zhu, and M.J. Meguid, "Modeling Electrical Conductivies of Nanocomposites with Aligned Carbon Nanotubes," *Nanotechnology*, pp. 5704-5712, 2011.

[80] L. Battisti and R. Fedrizzi, "2D numerical simulation of a wind turbine de-icing system, using cycled heating," *Wind Engineering*, vol. 31, no. 1, pp. 33-42, 2007.

[81] S. Butterfield, S. Sheng, and F. Oyague, "Wind energy's new role in supplying the world's energy: What role will structural health monitoring play?," in *7th International Workshop on Structural Health Monitoring*, Stanford, California, 2009.

[82] Rodrigo Capaz, Catalin Spataru, Paul Tangney, Marvin Cohen, and Steven Louie, "Temperature dependence of the band gap of semiconducting carbon nanotubes," *Physical Review Letters*, vol. 94, 2005.

[83] C. Chang, M. Ho, G. Song, Y.L. Mo, and H. Li, "A feasibility study of self-heating concrete utilizing carbon nanofiber heating elements," *Journal of Smart Materials and Structures*, vol. 18, 2009.

[84] B. Chen, K. Wu, and W. Yao, "Conductivity of carbon fiber reinforced cement-based composites," *Cement & Concrete Composites*, vol. 26, pp. 291-297, 2004.

[85] Klaus Friedrich, Stoyko Fakirov, and Zhong Zhang, *Polymer Composites: from nano-to-macro-scale*. New York: Springer Science, 2005.

[86] H.Z. Geng, D.S. Lee, K.K. Kim, G.H. Han, H.K. Park, and Y.H. Lee, Y.H."Absoprtion spectroscopy of surfactant-dispersed carbon nanotube film: Modulation of electronic structures," *Chemical Physical Letters*, vol. 455, no. 4-6, pp. 275-278, 2008.

[87] C.L. Kane, E.J. Mele, R.S. Lee, J.E. Fischer, P. Petit, H. Dai, A. Thess, R.E. Smalley, A.R.M. Verschueren, S.J. Tans, and C. Dekker"Temperature-dependent resistivity of single-

wall carbon nanotubes," *Europhysics Letters*, vol. 41, no. 6, pp. 683-688, 1998.

[88] M. Sen, "A review of the principles and applications of thermal control," *Journal of the Mexican Society of Mechanical Engineers*, pp. 115-131, 2004.

[89] Mithun Singla, "Advanced Sliding Mode Controller and Its Innovative Applications Using Smart Materials," Houston, TX, PhD Dissertation 2012.

[90] American Chemical Society, *Polymer Nanocomposites: Synthesis, Characterization and Modeling*, R Krishnamoorti and R.A Vaia, Eds. Washington D.C.: American Chemical Society, 2002.

[91] N. Ueda and M. Taya, "Prediction of the electrical conductivity of two-dimensionally misoriented short fiber composites by a percolation model," *Journal of Applied Physics*, pp. 459-461, 1986.

[92] Ting Yang, Mithun Singla, Gangbing Song, and Joey Yang, "Experimental Study on Carbon Fiber Tape-Based Deicing Technology," *Journal of Cold Regions Engineering*, pp. 55-63, 2012.

[93] Chongwu Zhou, Jing Kong, and Hongjie Dai, "Electrical measurements of individual semiconducting single-walled carbon nanotubes of various diameters," *Applied Physics Letters*, vol. 76, no. 12, pp. 1597-1600, March 2000.

[94] G.C. Papanicolaou, A.G. Xepapadaki, and G.D. Tagaris, "Effect of thermal shock cycling on the creep behavior of glass-epoxy composites," *Composite Structures*, vol. 88, pp. 436-442, 209.